International Journal of Modern Physics A
Vol. 36, No. 16 (2021) 2130009 (70 pages)
© World Scientific Publishing Company
DOI: 10.1142/S0217751X2130009X

Vector-Boson scattering at the LHC: Unraveling the electroweak sector

Roberto Covarelli*
Physics Department of University of Torino and INFN,
Via Pietro Giuria 1, Torino, I-10125, Italy
roberto.covarelli@unito.it

Mathieu Pellen
Albert-Ludwigs-Universität Freiburg, Physikalisches Institut,
Hermann-Herder-Straße 3, D-79104 Freiburg, Germany
mathieu.pellen@physik.uni-freiburg.de

Marco Zaro
TIF lab, Dipartimento di Fisica, Università degli Studi di Milano
and INFN, Sezione di Milano, Via Celoria 16, 20133 Milano, Italy
marco.zaro@mi.infn.it

Received 22 February 2021
Revised 2 April 2021
Accepted 6 April 2021
Published 31 May 2021

Vector-boson scattering (VBS) processes probe the innermost structure of electroweak (EW) interactions in the Standard Model (SM), and provide a unique sensitivity for new physics phenomena affecting the gauge sector. In this review, we report on the salient aspects of this class of processes, both from the theory and experimental point of view. We start by discussing recent achievements relevant for their theoretical description, some of which have set important milestones in improving the precision and accuracy of the corresponding simulations. We continue by covering the development of experimental techniques aimed at detecting these rare processes and improving the signal sensitivity over large backgrounds. We then summarize the details of the most relevant VBS signatures and review the related measurements available to date, along with their comparison with SM predictions. We conclude by discussing the perspective at the upcoming Large Hadron Collider runs and at future hadron facilities.

Keywords: Vector-boson scattering; large hadron colliders; electroweak interactions.

---

*Corresponding author.

Contents

1. Introduction 3
2. General Aspects of VBS at the LHC 4
    2.1. Definition of VBS 5
    2.2. Polarized VBS 8
        2.2.1. Definition of polarized cross section 8
        2.2.2. Phenomenological results 11
    2.3. Theoretical predictions 13
        2.3.1. Effects of QCD origin 13
        2.3.2. Effects of EW origin 18
    2.4. Experimental techniques 20
        2.4.1. The ATLAS and CMS detectors 21
        2.4.2. Tagging-jet reconstruction 23
        2.4.3. Vector-boson reconstruction 25
        2.4.4. Monte Carlo simulation 27
    2.5. Impact on Beyond-the-Standard-Model theories 28
3. VBS Processes at the LHC 32
    3.1. The $\mathrm{W}^{\pm}\mathrm{W}^{\pm}\mathrm{jj} \to \ell^{\pm}\nu\ell'^{\pm}\nu\mathrm{jj}$ final state 32
        3.1.1. Theoretical calculations 32
        3.1.2. Experimental approaches 33
    3.2. The $\mathrm{W}^{\pm}\mathrm{Zjj} \to \ell^{+}\ell^{-}\ell'^{\pm}\nu\mathrm{jj}$ final state 38
        3.2.1. Theoretical calculations 38
        3.2.2. Experimental approaches 40
    3.3. The $\mathrm{ZZjj} \to \ell^{+}\ell^{-}\ell'^{+}\ell'^{-}\mathrm{jj}$ and $\to \ell^{+}\ell^{-}\nu\bar{\nu}\mathrm{jj}$ final states 42
        3.3.1. Theoretical calculations 42
        3.3.2. Experimental approaches 44
    3.4. The $\mathrm{W}^{+}\mathrm{W}^{-}\mathrm{jj} \to \ell^{\pm}\nu\ell'^{\mp}\nu\mathrm{jj}$ final state 47
        3.4.1. Theoretical calculations 47
        3.4.2. Experimental approaches 47
    3.5. The semileptonic final states 48
        3.5.1. Theoretical calculations 48
        3.5.2. Experimental approaches 48
    3.6. The $\mathrm{W}^{\pm}\gamma\mathrm{jj}$ and $\mathrm{Z}\gamma\mathrm{jj}$ final states 52
        3.6.1. Theoretical calculations 52
        3.6.2. Experimental approaches 52
    3.7. The exclusive $\gamma\gamma \to \mathrm{W}^{+}\mathrm{W}^{-}$ final state 55
        3.7.1. Theoretical calculations 56
        3.7.2. Experimental approaches 56
4. Prospects for High-Luminosity and High-Energy LHC Scenarios 57
5. Conclusion 59

Acknowledgments 60

References 60

1. Introduction

The Standard Model (SM) of fundamental interactions is a theory which explains natural phenomena at the smallest distances that can be probed by human-built scientific facilities. Despite the very simple assumptions it is based upon, Lorentz invariance, locality, and gauge symmetries, it is able to explain an astonishing wide range of phenomena, from atomic spectroscopy to particle collisions at the highest possible energy. In a Lagrangian formulation, forces are represented by gauge fields, with a symmetry group $\mathcal{G} = \mathrm{SU}(2)_L \otimes \mathrm{U}(1)_Y \otimes \mathrm{SU}(3)_C$,[1–3] where the three groups respectively gauge the weak isospin, hypercharge, and color charge quantum numbers. Matter is represented by spin-$\frac{1}{2}$ fields, which fall under different representations of the gauge groups: the quarks, which are triplets for $\mathrm{SU}(3)_C$, and the leptons which are singlets. Quark and lepton fields come in three families, i.e. three copies with identical gauge quantum numbers, but with different masses. Each family is organized in doublets. Particles within each doublet differ by their electric charge, so there are up- and down-type quarks (u, d), as well as neutrinos and charged leptons (ν, ℓ). Remarkably, the interactions with the $\mathrm{SU}(2)_L \otimes \mathrm{U}(1)_Y$ fields are dictated by the fermion helicity: indeed, only left-handed doublets are charged under $\mathrm{SU}(2)_L$, which makes gauge interactions in the SM *chiral*.

This seemingly neat and simple structure, however, is not sufficient to explain the origin of mass of gauge bosons, as well as fermions, since an inclusion of mass terms in the Lagrangian would unavoidably lead to breaking gauge symmetries. This problem was solved in the 1960's by Higgs, Brout, Englert, Guralnik, Hagen, and Kibble.[4–9] By adding a new scalar field to the theory, it is possible to trigger the so-called spontaneous Electroweak Symmetry Breaking (EWSB), giving mass to the gauge fields and preserving gauge symmetries at the same time. After spontaneous symmetry breaking, the hypercharge and isospin fields mix and give rise to the mediators of the electromagnetic and weak interactions: the massless photon, γ, and the massive weak bosons, $\mathrm{W}^{\pm}$ and Z. Similarly, the Yukawa-type interactions between the scalar field and the fermions give rise to the fermionic masses.[2] The remainder of the scalar field is the so-called Higgs boson, a new particle whose existence is a prediction of the SM. The quest for this new particle culminated in 2012, almost 50 years after its existence was postulated, with the discovery announced by the ATLAS and CMS experiments at CERN.[10,11]

After the discovery of the Higgs boson, while the SM is a complete and consistent theory, some phenomena remain unexplained: the dominance of matter over anti-matter in the universe, the nonnatural pattern of fermionic masses, and the evidence for neutrino oscillations are some of these. This is why extensions of the SM have been hypothesized, which either predict new particles, or deviations of parameters from the SM predictions, or both. Experimental searches and measurements, such as those carried out by the ATLAS and CMS experiment at the CERN Large Hadron Collider (LHC), scrutinize many different scattering processes in order to find any sign of physics beyond the SM (BSM). Among the various processes which trigger the attention of theory and experimental experts, vector-boson scattering (VBS) is certainly one prominent example. Indeed, it probes two key aspects of the SM together: gauge interactions on the one hand, being one of the few processes with tree-level sensitivity to the quadrilinear (or quartic) gauge couplings; the couplings between the Higgs and gauge bosons on the other hand, which are probed at energy scales which can sensibly differ from the Higgs mass. Indeed, a typical undergraduate textbook exercise is to show that, in the SM, the three classes of Feynman diagrams consisting of (i) diagrams featuring only trilinear gauge couplings, (ii) diagrams featuring the quartic gauge coupling, and (iii) diagrams featuring the Higgs boson violate unitarity, if considered on their own. However, when considering all the three classes together, unitarity is restored.

At the time when this review is written, between the LHC Run-2 and Run-3, experimental collaborations have collected the first evidences for rare VBS processes, while on the theory side several key advances in their description have been achieved. The scope of the review is therefore to present such advancements both on the theoretical and experimental side, and to outline the possible improvements that could be attained with the LHC Run-3 data. In particular, this work focuses on SM results, while BSM physics in VBS is only briefly reviewed. The reader interested in BSM can find a more extensive discussion in Ref. 12. In addition, complementary literature on the topic of VBS exists and can be found in Refs. 13–16 and references therein.

This review is structured as follows. The first part is devoted to general aspects of VBS at the LHC and begins with a definition of what is actually meant by VBS in this context. It then turns to the theoretical aspects and experimental techniques use to predict and measure VBS at the LHC. The second part reviews all the possible VBS signatures at the LHC from both an experimental and a theoretical perspective. After this part, which is the core of the review, a short section is dedicated to the future of VBS measurements, especially concerning the High-Luminosity phase of the LHC as well as higher-energy regimes. Finally, the review ends with a summary and concluding remarks in the last section.

2. General Aspects of VBS at the LHC

In this section, general aspects of VBS at the LHC are addressed. First, a clear definition of VBS at the LHC is given. In particular, emphasis is put on potential differences between theory and experiment in that respect. The concept of *polarized* VBS cross-section is then introduced and results related to that topic are reviewed.

After these introductory sections, the theoretical and experimental status of VBS at the LHC is discussed. For the theory part, all aspects related to Quantum Chromo-Dynamics (QCD) and electroweak (EW) calculations are presented. The experimental part starts with the description of the ATLAS and CMS detectors, before moving to the main aspects of VBS analyses: the reconstructions of tagging jets and of the VBS final states.

This section ends with a short review of current limits on anomalous quartic couplings, obtained by the ATLAS and CMS collaborations during the first two runs of the LHC. In particular, no bounds on concrete models are discussed as these can be found in other reviews such as Ref. 12.

2.1. *Definition of VBS*

From an experimental perspective, a scattering process at the LHC is defined through its measured final state. It includes particle jets, leptons, photons or missing energy from neutrinos, which define the signature of the process. From a theoretical point of view, a scattering process is defined through its external particles as well as its strong and EW couplings in perturbative theory. While these two definitions partially overlap, they also induce some ambiguities when comparing measurements with theory predictions.

The measurement of VBS at the LHC is exemplary in this respect. The typical picture of VBS consists of two gauge bosons radiated off two separate quarks lines to scatter. Typical Feynman diagrams are shown in the top row of Fig. 1. In case of heavy vector bosons (all except γ), the VBS process is thus defined at Born level at the order $\mathcal{O}(\alpha^6)$, upon including the decay products of the heavy gauge bosons. It has quarks in the initial state and at least two quarks and up to four leptons in the final state. This implies that three possible VBS signatures at the LHC are: two jets and four leptons (*fully leptonic*), four jets and two leptons (*semi-leptonic*/*semi-hadronic*), or six jets (*fully hadronic*). This definition has the advantage to be clearly gauge invariant and to describe all nonresonant, off-shell, and interference effects. In particular, it means that many other diagrams beyond the VBS ones such as tri-boson contributions are included (some of them are shown in the bottom row of Fig. 1). In order to select VBS diagrams only, approximations to the full process like the effective vector-boson[17–21] or the VBS[22, 23] ones have to be used.

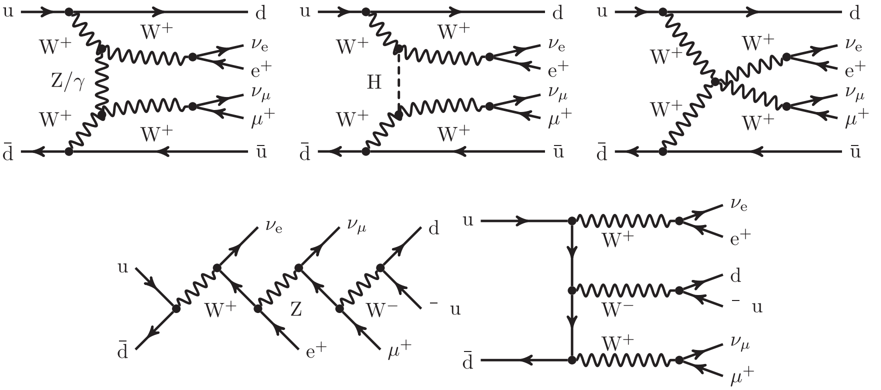

Fig. 1. Typical Feynman diagrams for VBS contributions (top) as well as non-VBS contributions (bottom) contributing to the process pp → $\mu^+\nu_\mu e^+\nu_e jj$. These figures are taken from Ref. 24.

Measuring experimentally a VBS signature necessarily implies also measuring non-VBS contributions. On an event-by-event basis, the quantum-mechanical nature of the process does not allow to distinguish a VBS event from a tri-boson event for example. Therefore, experimental analyses targeting VBS measurements sometimes include specific cuts in order to suppress undesired contributions in the definition of fiducial regions for the measurements. In the case of tri-boson contributions, a typical cut would be an invariant-mass cut on the decay products of a W/Z boson around their mass. Alternatively, such contributions can also be subtracted from the measurements using Monte Carlo simulations.

In addition to the purely EW contributions at order $\mathcal{O}(\alpha^6)$, VBS signatures also feature irreducible contributions of orders $\mathcal{O}(\alpha_s\alpha^5)$ and $\mathcal{O}(\alpha_s^2\alpha^4)$. These three contributions are usually referred to as *EW (or VBS) signal*, *interference*, and *QCD background*, respectively. Again, on an event-by-event basis, an event cannot be unambiguously attributed to any of these contributions. Nonetheless, experimental collaborations have measured VBS in signal-enriched phase-space regions upon applying specific kinematic cuts.

The justification of such a procedure is that the EW and the QCD contributions behave rather differently. In particular, given their rather different QCD structures, they tend to be maximal in different phase-space regions. The EW component does not feature QCD exchanges between the two quark lines while the QCD component does.[15] It implies that the differential cross-section as a function of the invariant mass or the rapidity difference of the two scattered quarks (that form what will be called the *tagging jets*) is very different for the two components:[23] typically, the EW component is characterized by tagging jets with large invariant masses (m_{jj}) and rapidity differences (Δy_{jj}), leaving the central part of the scattering free from QCD activity, at least in the fully leptonic signature, while it is the opposite for the QCD component. This is particularly well illustrated by Fig. 2 which shows two-dimensional differential distributions of the three contributions as a function of the invariant mass and rapidity difference of the two tagging jets. Therefore, in the same way as for non-VBS contributions, cuts can thus be applied in order to suppress the interference and/or QCD background: the invariant mass of the tagging jets and their rapidity separation are the basic discriminating cuts for VBS measurements at the LHC.

Alternatively, the QCD and interference contributions can again be subtracted using Monte Carlo predictions, the aim still being to isolate VBS contributions from its irreducible background. While this procedure is already questionable at LO, it is not meaningful at NLO and beyond. At LO, it is an arbitrary choice to include interference contribution to either the EW signal or to the QCD background as by definition the interference possesses both amplitudes. At NLO, the number of contributions goes up to 4 as shown in Fig. 3. In particular, some of these corrections are of mixed type which means that two different Born processes (with the two different amplitudes) received corrections. Because the two types of corrections are linked by infrared singularities, they cannot be separated in contributions that

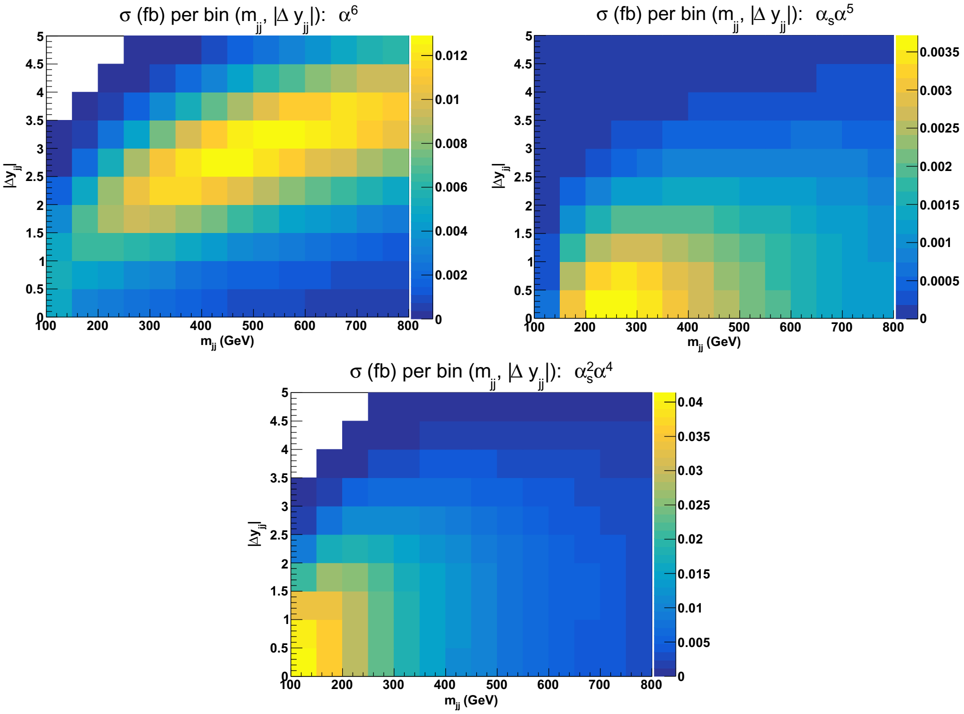

Fig. 2. Double-differential distributions in the variables $m_{\rm jj}$ and $|\Delta y_{\rm jj}|$ for the three LO contributions of orders $\mathcal{O}(\alpha^6)$ (top left), $\mathcal{O}(\alpha_{\rm s}\alpha^5)$ (top right), and $\mathcal{O}(\alpha_{\rm s}^2\alpha^4)$ (bottom). Typical event selection is applied apart from cuts on $m_{\rm jj}$ and $|\Delta y_{\rm jj}|$. These figures are taken from Ref. 23.

$$\begin{tikzcd}
\textbf{LO} & & \mathcal{O}(\alpha^6) \arrow[dl, "\mathrm{EW}"'] \arrow[dr, "\mathrm{QCD}"] & & \mathcal{O}(\alpha_{\rm s}\alpha^5) \arrow[dl, "\mathrm{EW}"'] \arrow[dr, "\mathrm{QCD}"] & & \mathcal{O}(\alpha_{\rm s}^2\alpha^4) \arrow[dl, "\mathrm{EW}"'] \arrow[dr, "\mathrm{QCD}"] & \\
\textbf{NLO} & \mathcal{O}(\alpha^7) & & \mathcal{O}(\alpha_{\rm s}\alpha^6) & & \mathcal{O}(\alpha_{\rm s}^2\alpha^5) & & \mathcal{O}(\alpha_{\rm s}^3\alpha^4)
\end{tikzcd}$$

Fig. 3. All contributing orders at both LO and NLO for the VBS processes at the LHC. This figure is taken from Ref. 24.

have only one type of amplitude (EW or QCD).[24] Hence, it is not possible to define an NLO signal or background without making assumptions. As a result, a measurement of the VBS signal necessarily relies on such theoretical inputs and their approximations.

In order to rely as less as possible on theoretical inputs, as well as to enable the soundest comparison between theory and data, fiducial measurements should be presented without subtracting any process contributing to the VBS signatures (neither irreducible QCD or interference background nor tri-boson contributions). From this physical measurement, various subtractions can subsequently be applied in order to single out the salient features of VBS. Such results are naturally subject to approximations and can then be studied as such. We believe that this is the best way to get most of the VBS physics in a transparent way and hence foster fruitful exchange between the theory and the experimental community. It is worth emphasizing that first steps in this direction have been already taken for example in Refs. 25 and 26 by presenting fiducial cross-sections of the EW and QCD component separately as well as their sum.

Along these lines, the presentation of several fiducial regions in experimental analyses is also welcome as it enables the study of various physical effects. Looser selections are typically dominated by the QCD background or tri-boson contributions, while tighter VBS cuts will highlight mostly the characteristics of the VBS at high-energy. These physical effects are the multiple sides of the same physical process and such measurements have therefore the power to explore all of them.

2.2. *Polarized VBS*

Among the various features of the SM which are especially relevant for VBS, the possibility to access the different polarization states of the vector bosons is certainly one of the most intriguing ones. After EWSB, massive vector bosons feature three physical polarization states: two transverse (left and right handed), $\epsilon_\mu^{\mathrm{L/R}}$, and one longitudinal, ϵ_μ^0. In the SM, the vector-boson masses and their longitudinal polarization are generated by the Higgs mechanism, and the presence of the Higgs boson unitarizes the scattering amplitude for longitudinal polarizations. Hence the ability to study different polarization states is a precious asset in order to validate the SM, or to spot possible deviations from its predictions. BSM physics may disrupt the unitarization of longitudinally-polarized vector bosons,[27–30] or alter the relative impact of different polarization states.

The possibility to explore different polarization states is a feature of all processes involving vector bosons (see e.g. Ref. 31). For example, single vector-boson production, possibly in association with jets, is dominated by left-handed polarization states,[32] while the W boson from the top decay is dominantly longitudinal.[33]

The definition of the production of a specific polarization state is therefore possible. In the following, we will show that this is true only in an idealized situation, as a realistic environment poses significant difficulties. We will discuss how these difficulties can be overcome and the necessary conditions for polarized cross-sections to be well defined. We will conclude the section by presenting some results for polarized VBS at hadron colliders in the SM and in some of its extensions.

2.2.1. *Definition of polarized cross section*

Several aspects need to be considered when one tries to define the production cross-section for a specific polarization state of a vector boson. In this discussion, we will follow the discussion of Ref. 34, which also documents the implementation of the polarized cross-section for $\mathrm{W}^+\mathrm{W}^-\mathrm{jj}$ in the PHANTOM code.[35] Extension to the cases of WZ and ZZ production is documented in Ref. 36. The first and most immediate aspect is that vector bosons are unstable particles which undergo a decay. Hence any information on their polarization must be kept through the decay processes. If we consider the case of a single vector boson (the generalization to the case of multiple vector bosons is trivial) which is produced from an initial state I and decays into a final state F:

$$I \to V \to F, \tag{1}$$

the corresponding matrix element can be written as:

$$\mathcal{M}_{I\to V\to F} = \mathcal{M}^{\mu}_{I\to V}\frac{-g_{\mu\nu}+\frac{p_\mu p_\nu}{M_V^2}}{(p^2-M_V^2)^2+M_V^2\Gamma_V^2}\mathcal{M}^{\nu}_{V\to F}. \tag{2}$$

Here, p is the momentum of the intermediate vector boson. The projector $-g_{\mu\nu}+\frac{p_\mu p_\nu}{M_V^2}$ can be expressed as the sum over the polarizations of the intermediate vector bosons:

$$-g_{\mu\nu}+\frac{p_\mu p_\nu}{M_V^2} = \sum_\lambda \epsilon^\lambda_\mu \epsilon^{\lambda^*}_\nu. \tag{3}$$

Now, when the amplitude in Eq. (2) is squared, one obtains

$$\begin{aligned}
|\mathcal{M}_{I\to V\to F}|^2 &= \mathcal{M}^{\mu}_{I\to V}\frac{\sum_\lambda \epsilon^\lambda_\mu \epsilon^{\lambda^*}_\nu}{\left(p^2-M_V^2\right)^2+M_V^2\Gamma_V^2}\mathcal{M}^{\nu}_{V\to F} \\
&\quad\times\left(\mathcal{M}^{\mu}_{I\to V}\frac{\sum_{\lambda'} \epsilon^{\lambda'}_\mu \epsilon^{\lambda'^*}_\nu}{\left(p^2-M_V^2\right)^2+M_V^2\Gamma_V^2}\mathcal{M}^{\nu}_{V\to F}\right)^* \\
&\neq \sum_\lambda\left[\mathcal{M}^{\mu}_{I\to V}\frac{\epsilon^\lambda_\mu \epsilon^{\lambda^*}_\nu}{\left(p^2-M_V^2\right)^2+M_V^2\Gamma_V^2}\mathcal{M}^{\nu}_{V\to F}\right. \\
&\quad\left.\times\left(\mathcal{M}^{\mu}_{I\to V}\frac{\epsilon^\lambda_\mu \epsilon^{\lambda^*}_\nu}{\left(p^2-M_V^2\right)^2+M_V^2\Gamma_V^2}\mathcal{M}^{\nu}_{V\to F}\right)^*\right].
\end{aligned} \tag{4}$$

The meaning of Eq. (4) is that, since the vector bosons are not external particles, their polarization states interfere with each other. This, in principle, jeopardizes the definition of a polarized cross-section. However, interference terms integrate to zero over the whole range of the decay azimuth angle, and this makes it possible, at least in principle, to have a well-defined polarized cross-section. It has to be stressed that, whenever cuts are imposed (as it is the case in any realistic setup) or when one is interested in observables sensitive to the decay degrees of freedom, particularly to the azimuth angle, the cancellation of interferences is not bound to happen. This can be observed in Fig. 4 for $\mathrm{W^+W^-}$jj VBS, where singly-polarized cross-sections (the positively-charged W remains unpolarized) and their incoherent sum are compared with the full cross-sections: the upper left plot shows the dijet invariant mass, which has no dependence on the lepton azimuth angle. The upper right plot shows the

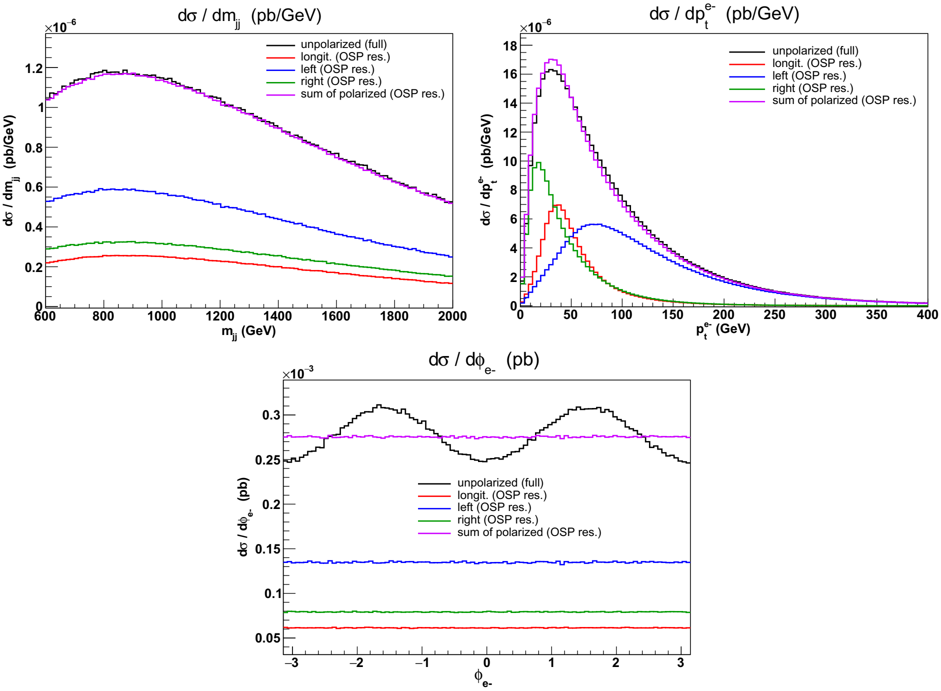

Fig. 4. (Color online) Differential singly-polarized cross-sections for opposite-sign W scattering at the LHC. Polarizations are defined in the laboratory frame. The unpolarized prediction (black) is compared with the incoherent sum (purple) of the polarized ones (blue, green and red; these use on-shell projection and take into account only the resonant diagrams). No cut is imposed on leptonic variables. These figures are taken from Ref. 34.

lepton transverse momentum, which has an indirect dependence on the azimuth angle. Finally, the bottom plot shows the lepton azimuth angle. It can be observed that, while for the dijet invariant mass the incoherent sum of the polarization and the full cross-section are indistinguishable, small but visible differences appear for the electron transverse momentum, and obvious effects appear for the azimuth angle. Observables which display good agreement between the incoherent sum of the different polarization states and the full result can be employed to extract the polarization fractions for the different states. While, as mentioned above, cuts on the leptons can in principle spoil such an agreement, in practice their effect is generally mild on most observables.

There are other aspects which need to be considered in the definition of polarized cross-section. First, vector bosons may be produced off-shell, i.e. far from the resonance peak. This issue is typically addressed by using the so-called on-shell projection (OSP), where some momentum transformation is used changing the momenta such that the intermediate vector boson is on its mass shell. This is similar to the so-called pole scheme approximation, usually employed in the computation of higher-order corrections (for example in Refs. 37–43 and references therein). Second, nonresonant diagrams may exists, i.e. diagrams for the process $I \to F$ that do not feature an intermediate vector boson in the s-channel (e.g. the left diagram in the second row of Fig. 1), but those are usually assumed not to contribute significantly to the cross-section. The last relevant aspect to be considered is that polarization vectors are not Lorentz-covariant, hence a given reference frame must be chosen. Typical choices are the partonic center-of-mass frame, the laboratory frame or the diboson center-of-mass frame. In particular the latter has been used in the analysis of Ref. 44. The choice of a given frame is mostly dictated by practical reasons, like the experimental capability to reconstruct the frame.[a] Studies available to date, see e.g. Ref. 45, show that no frame choice has particular advantage over the others.

To summarize, the definition of a polarized cross-section relies on the following assumptions: interferences cancel in Eq. (4) (strictly true only for integrated quantities); nonresonant diagrams are neglected; and an OSP is introduced to reshuffle the external momenta onto the vector-boson mass shell. In this context, the polarization fractions $f_{L/R}$ and f_0 can be introduced (with polarization vectors in a frame of choice) for a specific kinematic variable X. If one considers the case of a $\mathrm{W}^{\pm}$ boson decaying into lepton and neutrino, where θ is the polar angle in the W rest frame (and the azimuth angle ϕ is integrated over), one obtains

$$\begin{aligned}\frac{1}{\frac{d\sigma(X)}{dX}}\frac{d\sigma(\theta,X)}{d\cos\theta dX} &= \frac{3}{8}(1\mp\cos\theta)^2 f_{\mathrm{L}}(X)\\ &\quad+\frac{3}{8}(1\pm\cos\theta)^2 f_{\mathrm{R}}(X)+\frac{3}{4}\sin^2\theta f_0(X). \end{aligned} \tag{5}$$

Using this equation, one could extract the polarization fractions from data by fitting the angular distributions. Experimental analysis is in practice more complicated, since selections alter the shape as a function of $\cos\theta$ and angular-dependent acceptance/efficiency factors must be taken into account.

The method discussed above is general, in the sense that it can be applied to any process featuring intermediate vector bosons. While the discussion has been carried assuming there is a single polarized vector boson, it can be easily extended to the case where more vector bosons appear, such as VBS. Besides the case mentioned above (single vector boson, and top production), the method of Ref. 34 has been also applied to vector-boson pair production in Refs. 43, 46, 47, and in Ref. 48 it has been automatized using MadGraph5_aMC@NLO[49] (henceforth denoted as MG5_aMC) and MadSpin,[50] paving the path to the possibility of including NLO QCD corrections in VBS analysis.

2.2.2. *Phenomenological results*

Having introduced the polarization fractions and their prerequisites to be well defined, we will show some phenomenological results which highlight how these fractions can be employed to probe beyond the SM effects.

---

[a] For a recent study on different reconstruction techniques, see e.g. Ref. 51.

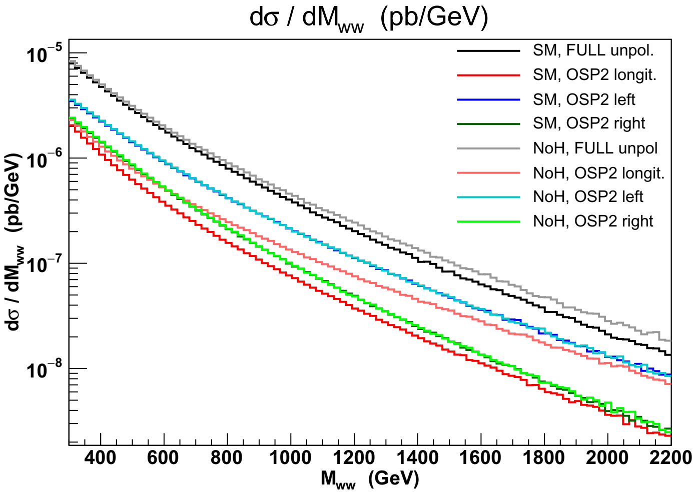

Fig. 5. Polarization fractions in the SM and in the Higgs-less SM, in opposite-sign W scattering at the LHC, for the invariant mass of the W pair. Polarizations are defined in the laboratory frame. The (negatively-charged) lepton from the polarized W boson is required to satisfy the cuts $p_T(\ell) > 20\,\text{GeV}$, $|\eta(\ell)| < 2.5$. This figure is taken from Ref. 34.

The first case we consider is discussed in Ref. 34, and it is the case of a Higgs-less SM, i.e. corresponds to pushing the Higgs boson mass to infinity.

In Fig. 5, the WW invariant-mass distribution is shown, for the unpolarized process as well as for the different polarization states of one of the negatively-charged vector boson. The SM and the Higgs-less SM (dubbed *NoH* in the figure) are shown. Since the Higgs boson unitarizes the scattering of longitudinal vector bosons, one expects the longitudinally-polarized component in the Higgs-less SM to display a harder behavior with respect to the SM case, as can be seen in the plot of Fig. 5. While the left and right polarizations display an identical behavior in the two models, the behavior of the longitudinal polarization is radically different at high energies. Indeed, in the SM, 21% of events feature a longitudinally-polarized vector boson when a minimum cut, $M_{\text{WW}} > 300\,\text{GeV}$ is required on their invariant mass. The fraction decreases to 15% when the invariant-mass cut is raised to 1 TeV. In the Higgs-less case, the two fractions become respectively 27% and 35%, with more than a factor-2 effect when the hardest cut is imposed.

The second example, from Ref. 48, compares the SM case with a composite-Higgs model.[52–59] In this class of models, or at least in their most recent versions, the interaction of the Higgs boson and the weak gauge bosons is rescaled with a common factor a, and can be described by the following effective Lagrangian[60,61]

$$L \supset \left(\frac{m_{\text{Z}}^2}{2}\text{Z}^\mu\text{Z}_\mu + M_W^2\text{W}^\mu\text{W}_\mu\right)\left(1 + 2a\frac{h}{v} + \cdots\right). \tag{6}$$

The SM case is recovered when the scattering of longitudinal vector bosons is unitarized, which corresponds to $a = 1$. Other values different from unity will display a

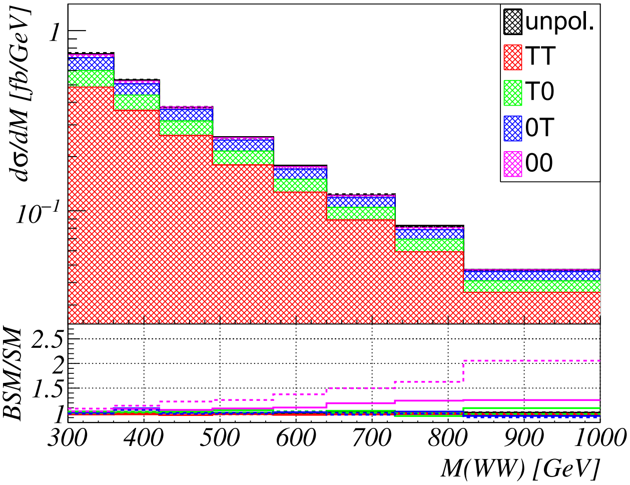

Fig. 6. Polarization fractions in the SM in opposite-sign W scattering at the LHC, for the invariant mass of the W pair. Polarizations are defined in the partonic center-of-mass frame. The namings 0 and T identify the longitudinal and transverse polarization, respectively. The inset displays the ratios $\mathcal{R}(M_{WW})$ defined in Eq. (7) for $a = 0.8$ (dashed) and $a = 0.9$ (solid). This figure is taken from Ref. 48.

unitary-violating behavior. As in the previous case, the process at hand is $\mathrm{W^+W^-jj}$ production and the WW invariant mass distribution shown in Fig. 6 is examined, where the polarization fractions of both vector bosons are given. The upper plot in the figure shows the polarization fractions in the SM ($a = 1$), while the lower inset shows how they are affected when one sets $a = 0.8$ (dashed) or $a = 0.9$ (solid), by plotting the ratio:

$$\mathcal{R}(M_{\mathrm{WW}}) \equiv \frac{d\sigma(a)}{dM_{\mathrm{WW}}} \Big/ \frac{d\sigma(a=1)}{dM_{\mathrm{WW}}} \,. \tag{7}$$

The most striking behavior can be observed in the ratio for the longitudinal-longitudinal scattering fraction. It shows effects of the order of 30% in the largest-mass bin considered for $a = 0.9$ and grows up to 100% when $a = 0.8$.

2.3. *Theoretical predictions*

In this section, we will review the state-of-the-art of the theoretical predictions for VBS, and we will discuss the main sources of theoretical uncertainty.

2.3.1. *Effects of QCD origin*

NLO QCD corrections The anatomy of QCD corrections in VBS processes is quite peculiar, and it is dictated by the underlying structure of the process. A typical t-channel VBS diagram at tree level, such as those in the top row of Fig. 1, features two quark lines that exchange EW bosons. Since no color charge is exchanged between the two quarks, QCD corrections tend to factorize, in the sense that they affect one quark line at a time. While nonfactorizable corrections exist, for example in the case of the scattering of identical quarks, they are suppressed by color considerations and by kinematics. If one neglects non-VBS diagrams, the situation is completely analogous to Higgs production in vector-boson fusion (VBF), where NLO QCD corrections were first computed in the factorized approximation using the so-called structure-function approach.[62] Indeed, also for VBS, the first results including NLO QCD corrections were obtained discarding nonfactorizable corrections.[63–66] Within this approximation, NLO QCD corrections to VBS are rather mild, and their exact impact depends on the cuts employed to define the VBS signal, on the choice of renormalization and factorization scales and, of course, on the specific process.

Going beyond this approximation, i.e. including nonfactorizable corrections, entails a major step in computational complexity. On the one hand, loops with many (six or more) external legs and high-rank numerators, due to the presence of vector bosons, have to be evaluated. On the other hand, nonfactorizable corrections are in general not Infra-Red (IR)-finite, and hence possibly dependent on the specific IR regulator. This could be avoided only by considering all contributions of $\mathcal{O}(\alpha_s\alpha^6)$, including those which classify as EW corrections to the LO QCD-EW interference of VVjj production, as depicted in Fig. 3 (in that figure, the NLO QCD corrections to VBS signal correspond to the $\mathcal{O}(\alpha_s\alpha^6)$ contribution). Only recently, with advanced techniques having paved the way to the automation of EW and mixed QCD-EW corrections, nonfactorizable contributions have been included in the NLO QCD corrections to VBS.[24,67,68] When they are compared to the approximation that assumes factorization, the impact of nonfactorizable QCD corrections is found to be small in typical VBS phase-spaces,[23] exceeding 5% only in more inclusive phase-spaces. This can be seen in Fig. 7 which shows two differential distributions in the invariant mass of the two tagging jets. The left-hand side shows a comparison of NLO predictions in an inclusive phase-space, while the right-hand one is in a more exclusive phase-space, typical of experimental analyses. The full predictions which include nonfactorizable corrections are denoted by either *full* or MoCaNLO + Recola. The differences among other predictions are due either to the inclusion or not of non-VBS contributions, or to the details of the definition of nonfactorizable corrections, or both.

Once NLO QCD corrections are included, theoretical uncertainties estimated through the variation of renormalization and factorization scale are of the order of few percent on NLO-accurate observables. In the case of $\mathrm{W}^{\pm}\mathrm{W}^{\pm}\mathrm{jj}$ production, this can be observed in Fig. 7 for the m_{jj} observable, where the theory uncertainty is shown as a blue band around the MoCaNLO + Recola prediction. The scale uncertainty is obtained through 7-fold scale variation (see Sec. 2.4.4). The inclusion of nonfactorizable corrections does not significantly impact the size of the scale uncertainty.

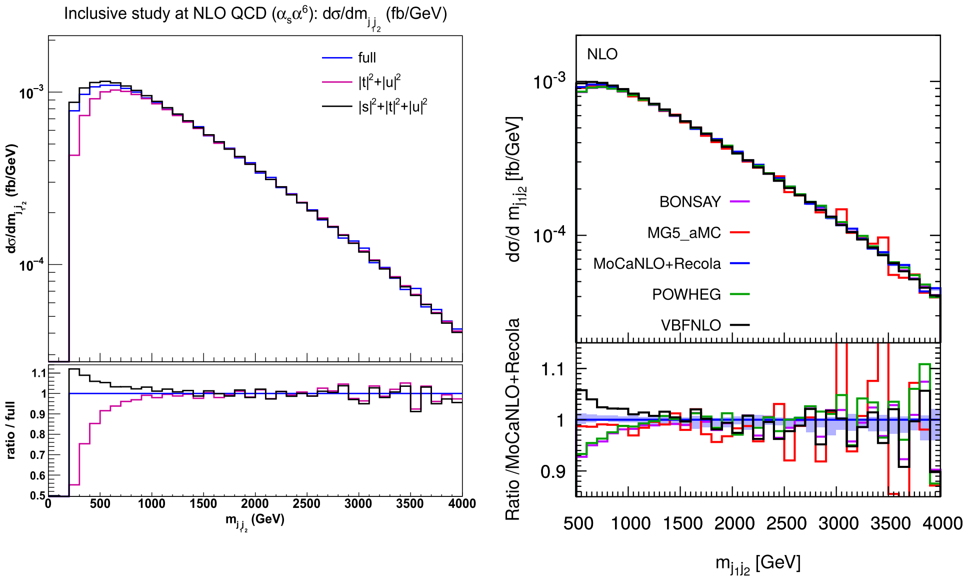

Fig. 7. Differential distributions in the invariant mass of the two tagging jets at the NLO (fixed order). Various theoretical predictions with different approximations are here compared in an inclusive set-up and a more exclusive one (as in the experimental analysis). The best prediction is denoted by either *full* or MoCaNLO+Recola. These figures are taken from Ref. 23.

Beyond NLO-QCD: NNLO and parton-shower effects For what concerns QCD effects beyond NLO, it is a fair statement that NNLO QCD corrections, even in the factorized approximation, are extremely challenging to compute, and will likely not be available on a short-term timescale. Indeed, at variance with the case of single- or even double-Higgs production in VBF, where corrections up to NNNLO in QCD have been computed within a factorized approach,[69–75] VBS processes present more complex topologies, since the outgoing vector bosons can couple to the quark lines.[b]

However, for almost all processes, NLO QCD corrections have been matched to parton-showers (PS) within different matching schemes,[23,79–82] and now this kind of processes are within the reach of automatic frameworks. In general, when compared with NLO predictions at fixed order, NLO+PS results show quite small (10%–15%) effects on the shape and normalization of distributions. The spread of predictions obtained with different matching schemes and/or different PS programs is also found to be at the 10% level, and it has been investigated in detail for $W^{\pm}W^{\pm}jj$ production in Ref. 23.

A relevant exception, worth to be discussed, is related to the modeling of the third-jet kinematics. It has been observed that, for predictions matched with

---

[b] Some recent achievements toward the computation of nonfactorizable corrections to Higgs production in VBF are worth to be cited,[76,77] which may be relevant also for VBS.

Pythia8,[83,84] the global-recoil scheme leads to a large unphysical enhancement of the third-jet activity in the mid-rapidity region, related to a wrong assignment of the phase-space boundaries for processes with initial-final color connections. Such an enhancement, absent in predictions obtained with other parton showers such as Herwig7,[85–87] is observed both with the Powheg[88,89] and the MC@NLO[90] matching schemes, although it is larger with the latter, owing to the fact that Powheg generates the first emission with an internal Sudakov factor (and thus shower effects only enter from the second emission on). This effect is discussed in detail for same-sign WW production in Ref. 23, but it is in fact a general issue affecting processes with VBF/VBS-type topologies. Indeed, a similar enhancement has been observed also in the measurement of EW single-Z production,[91] and for Higgs production in VBF.[78]

While the unphysical enhancement disappears when a new recoil scheme, developed for Deep-Inelastic-Scattering processes (dipole recoil[92]), is employed, the way Monte Carlo counterterms are currently implemented e.g. in MG5_aMC prevents the user to employ a recoil scheme different from the global recoil.[c] This does not apply to a Powheg-type matching, where the user can instead change the shower parameters more freely.

In Ref. 78, it has been shown that, even within the global-recoil scheme, this effect disappears when an NLO-accurate description of the third jet at the matrix-element level is employed, as can be observed in Fig. 8. This is a further demonstration that the central-rapidity enhancement observed for predictions matched with Pythia8 is unphysical and, as such, it should not be considered as an uncertainty source for the third-jet description. Given the similarities between VBS and VBF from the QCD point of view, these conclusions can be extended from the latter to the former. They could also be verified explicitly using an NLO prediction for VBS with three jets, which is available at the moment, but should not be beyond the reach of modern event generators and matrix-element providers.

PDF uncertainties Accounting for all sources of uncertainty stemming from QCD requires also the inclusion of those coming from parton distribution functions (PDFs). At LO, only quarks appear in the initial state of VBS processes, regardless of the specific final state. Within typical VBS cuts, they mostly feature intermediate values of the Bjorken x's and scales $Q = \mathcal{O}(100)$ GeV.

From Fig. 9, one can appreciate that the bulk of the $\mathrm{W}^{\pm}\mathrm{W}^{\pm}\mathrm{jj}$ cross-section comes from $x \simeq 0.2$, a region where quark densities, especially valence ones, are quite well constrained nowadays, with uncertainties below 5%.[94] As gluons only enter at NLO, they give a subleading contribution to the cross-section, considering the small size of NLO corrections discussed above. The produced final state, in particular the charges of the gauge bosons, affects the combination of flavors which

---

[c] A new implementation of the Monte Carlo counterterms has been recently presented in Ref. 93, and future developments on allowing a more flexible choice of shower parameters are in progress.

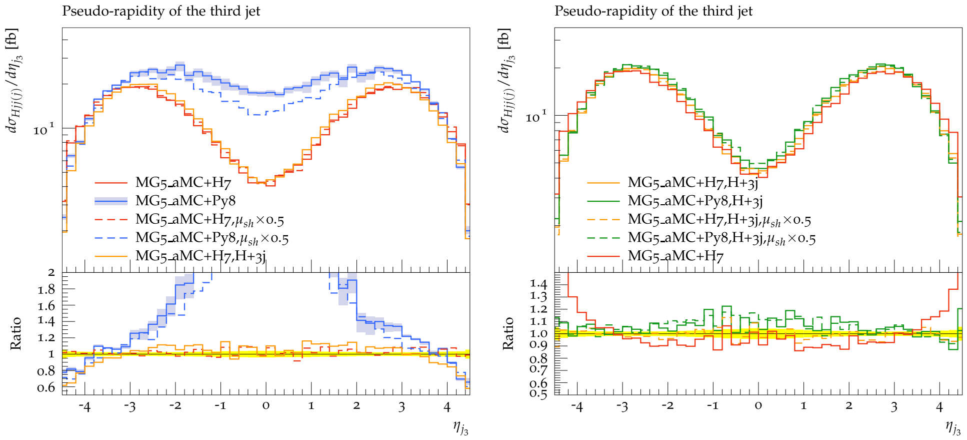

Fig. 8. (Color online) The rapidity of the third jet in Higgs production via VBF, obtained using MG5_aMC + Pythia8 or Herwig7. The left panel shows predictions for the production of a Higgs boson plus two jets at NLO+PS matched with Pythia8 (blue) or Herwig7 (red), including renormalization and factorization scale uncertainties (blue band) as well as variations of the shower starting scale (dashed lines), Together with the prediction for Higgs plus three jets at NLO+PS matched with Herwig7 (orange). The right panel shows predictions for the Higgs boson plus three jets at NLO, matched with Herwig7 (orange) or Pythia8 (green). together with the prediction for Higgs plus two jets at NLO + PS matched with Herwig7 (red solid). These figures are taken from Ref. 78.

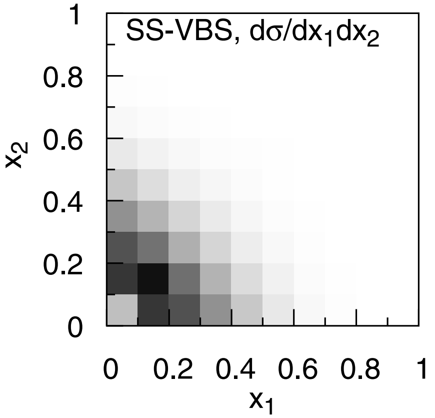

Fig. 9. The Bjorken x regions contributing to same-sign WW production via VBS, at the 13 TeV LHC. The color coding is a follow: maximal is for black, minimal is for white. The set-up used for this plot is the same as in Ref. 23.

can initiate the process: positively charged final states, such as W^+W^+jj production, are mostly sensitive to valence quarks, while for neutral or negatively charged ones the contribution of sea quarks becomes more important. Hence, PDF uncertainties are expected to be quite process-specific.

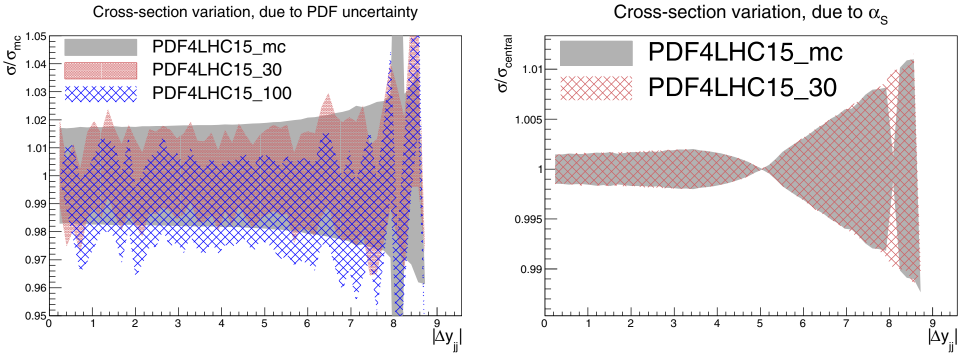

Fig. 10. PDF (left) and α_s (right) uncertainty for the rapidity separation of the two tagging jets, evaluated with the PDF4LHC15 set. These figures are taken from Ref. 95.

If we consider again, as an example, the case of same-sign W boson production, and specifically the rapidity separation of the two jets, one can appreciate from Fig. 10 that the PDF uncertainties, evaluated with the PDF4LHC15 set,[94] are at the level of $\pm 2\%$ for a large part of the range, up to 4% only for extreme separations. For the same observable, uncertainties due to α_s are (as expected) totally negligible, below 1% across almost the whole considered range.

As mentioned above, these numbers are expected to be rather process specific and are calculated in experimental analyses targeting the corresponding final states. In order to have an idea of how the charge of the final state can affect their size, one can consider the case of charged-Higgs production via VBF, for which these studies are available.[96–98] In this case, the Higgs mass plays the role of the invariant mass of the vector-boson pair. Estimations in Ref. 97 show that PDF uncertainties never exceed a few percent, being smaller for lighter final states and when valence-quark contributions are mostly probed (Fig. 10).

2.3.2. *Effects of EW origin*

Given the magnitude of the strong and EW couplings, for typical LHC processes NLO EW corrections are generally of the order of NNLO QCD corrections, that is a few percent. This power-counting argument is usually valid at the level of the total cross-sections, but the situation is rather different when considering differential distributions, as EW and QCD corrections exhibit a rather different behavior and are relevant in different phase-space regions. In general, they become negative and large (typically several 10%) in the high-energy limit because of Sudakov logarithms.[99]

In the case of VBS, the global picture is quite different, namely the NLO EW corrections are large relative to QCD corrections of the same order. As shown in Ref. 100, large EW corrections are an intrinsic feature of VBS at the LHC. At the level of the total cross-section, they can be of the order of -20% and reach up to -40% in tails of differential distributions. Their origin can be attributed to

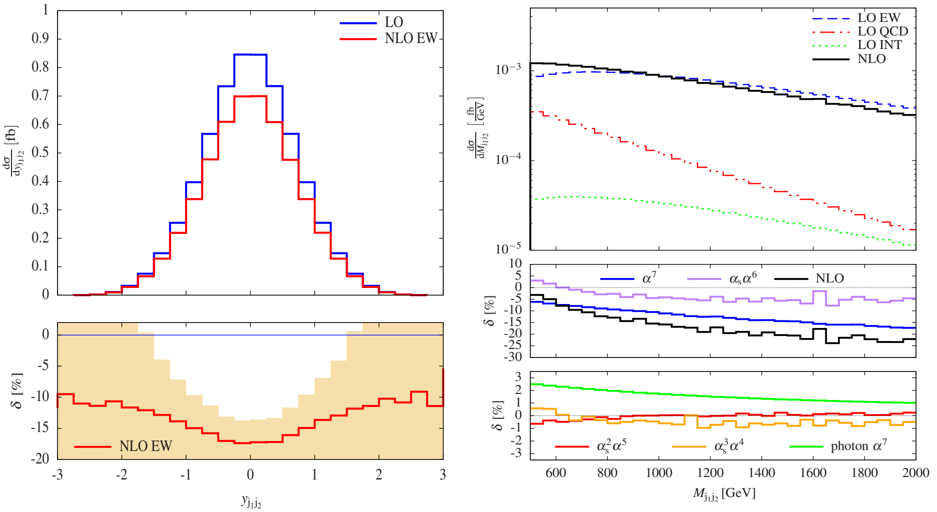

Fig. 11. (Color online) NLO EW corrections to same-sign WW scattering for the rapidity distribution of the two tagging jets (left). The yellow band in the lower plot represents the expected statistical experimental uncertainty at 3000 fb^{-1}. Full NLO corrections to same-sign WW scattering for the invariant mass of the two tagging jets (right). The left figure is taken from Ref. 100 while the right one is taken from Ref. 24.

the massive t-channel which enhance the typical scale of the process,[101] as well as the fact that the EW Casimir operators are larger for bosons than fermions.[102] For same-sign WW scattering, where all NLO corrections are known, the EW corrections to the VBS process of order $\mathcal{O}(\alpha^7)$ are the largest corrections.[24] Such a pattern has been confirmed for the WZ[67] and ZZ[68] signature. It is also worth mentioning that such EW corrections are largely independent of the charge of the final state as shown in Ref. 103 for $\mathrm{W}^\pm\mathrm{W}^\pm\mathrm{jj}$. Even more, the Leading-Log approximations derived in Refs. 67, 68, 100 are rather universal due to the identical $\mathrm{SU}(2)_\mathrm{w}$ couplings occurring in all scatterings. In Fig. 11, the differential distribution in the rapidity of the two tagging jets is displayed. In the lower plot, the yellow band represents the expected statistical experimental uncertainty in each bin for the High-Luminosity LHC collecting 3000 fb^{-1}. Given their magnitude, one can thus expect that high-luminosity measurements will be sensitive to such EW corrections.

Another source of EW effects is the inclusion of photon PDF. The determination of the photon PDF has witnessed a complete change of paradigm in 2016, when the LUXqed methodology was introduced,[104, 105] which employs a more robust determination from first principles of the photonic density. Thanks to these works, the photon density can now be constrained at a level comparable to that of the strong-interacting partons. This was made possible by relating photon-induced processes with their nonphoton induced counterpart, and using this relation to extract the photon density. Before 2016, the only available approaches were either relying on some *a priori* parametrization of the photon density,[106, 107] or on leaving it completely free to be fit.[108] This led in the first case to an impossible, or very difficult quantification of theoretical uncertainties, and in the second to huge uncertainties, often of the order of 100%, relative to the impact of the photon density. The LUXqed methodology is now employed by all major PDF providers, such as NNPDF[109] and MMHT[110] as well as the PDF4LHC working group.[94]

For example, in same-sign WW scattering,[24] the photon-induced contributions are of the order of 2.7% with NNPDF-3.0 QED[108] while they go down to 1.5% when using the LUXqed_plus_PDF4LHC15_nnlo_100 set. Due to charge conservation, LO photon-induced contributions are present for the WZ, ZZ, and W^+W^- channels as well. They involve one or two initial-state photons and contribute to the orders (α^6) and $(\alpha_s\alpha^5)$. They amount to about 0.4% with respect of the LO of order (α^6) for WZ.[67]

When referring to NLO EW corrections, it was so far implied that only real photon radiations are included. The radiation of heavy gauge bosons occurs at the same perturbative order, and in principle can also be accounted for. To date, this effect is relatively unexplored in the context of VBS, while studies exist for other processes.[111–113] In Ref. 114, the related correction has been estimated to be of the order of few percent for the High-Luminosity LHC at the level of the total cross-section.

Finally, for signatures other than same-sign WW scattering, there also exist a photon-to-jet conversion function which is necessary to cancel IR divergences associated to photons splitting into a quark–antiquark pair.[115] While it ensures a proper treatment of this nonperturbative contribution, its numerical impact is rather small and has been evaluated to be the order of 0.01% for WZ.[67]

2.4. *Experimental techniques*

Taking into account the decay of heavy gauge bosons, VBS cross-sections are typically of the order of femtobarns in proton–proton (pp) collisions at a center-of-mass energy of 13 TeV. For this reason, the LHC experiments that have sensitivity to these processes are the ones which benefit from the full amount of integrated luminosity delivered by the accelerator, ATLAS[116] and CMS.[117,d]

Both ATLAS and CMS have analyzed fully or partially the 13 TeV LHC dataset delivered between 2016 and 2018, referred to as *Run*-2 of the accelerator, which corresponds to about 135–140 fb^{-1} per experiment, depending on the percentage of high-quality data which can be used to reconstruct a specific final state. In these runs, the mean number of pp collisions per LHC bunch crossing (*pileup*) varied between 23–27 in 2016 and 35 and more in 2017 and 2018. Using such a large dataset, the experimental knowledge of VBS has dramatically increased in the recent years. Starting from the pre-Run-2 results at 7 and 8 TeV where just upper limits on VBS

---

[d] Apart from an exploratory theoretical study for the LHCb experiment,[118] no results are available from other experiments than ATLAS and CMS.

SM cross-sections were reported, both experiments have now claimed evidence or observation for all the main VBS processes.

2.4.1. *The ATLAS and CMS detectors*

ATLAS and CMS are general-purpose detectors with a cylindrical geometry and a nearly hermetic coverage in θ and ϕ.[e] Figure 12 shows longitudinal views of a quadrant of the ATLAS and CMS detectors.

In both ATLAS and CMS the interaction point is surrounded by tracking detectors. For both the innermost system consists of a silicon pixel detector, providing precise estimation of track impact parameters and vertices, and is complemented by outer layers of silicon microstrip detector. In ATLAS tracking information is also provided by a transition radiation tracker. In both experiments, these inner detectors provide precise measurements of charged-particle tracks in the pseudorapidity range $|\eta| < 2.5$.

Electromagnetic and hadronic calorimeters cover the region $|\eta| < 3.2$ in ATLAS and $|\eta| < 3.0$ in CMS. In ATLAS the electromagnetic calorimeter is based on high-granularity, lead/liquid-argon (LAr) sampling technology, while in CMS it consists of high-resolution lead tungstate crystals. The ATLAS hadronic calorimeter is comprised of a steel/scintillator-tile sampling detector in the central region and a copper/LAr detector in the region $1.5 < |\eta| < 3.2$, while CMS uses a brass/scintillator detector.

For VBS signatures, it is of paramount importance to collect electromagnetic and hadronic energies at larger values of pseudorapidity. To achieve this goal, both ATLAS and CMS are equipped with forward calorimeters, that have lower granularities but must satisfy stringent radiation hardness requirements. In ATLAS the region of the detector $3.1 < |\eta| < 4.9$ features a forward calorimeter (FCal), measuring electromagnetic and hadronic energies in copper/LAr and tungsten/LAr modules. In CMS the forward calorimeter (HF) covers the region up to $|\eta| \lesssim 5.0$ and consists of a steel absorber equipped with quartz fibers of two different lengths which distinguish the electromagnetic and hadronic components.

The magnet arrangement is different in the two experiments. CMS features a large superconducting solenoid with a 6-m inner diameter providing an axial magnetic field of 3.8 T. In ATLAS, a smaller solenoid providing a magnetic field of 2 T surrounds the inner tracker, while three large superconducting toroidal magnets are placed with an eightfold coil symmetry outside the calorimeters.

In both ATLAS and CMS the muon spectrometer comprises trigger and high-precision tracking chambers to measure the trajectory of muons. Detector

---

[e] Both ATLAS and CMS use right-handed coordinate systems with their origin placed at the nominal interaction point and the z-axis running along the beam direction. The x- and y-axes point to the center of the LHC ring and upward, respectively. Cylindrical coordinates (r, θ, ϕ) are used in this coordinate system. The subscript T refers to quantities measured in the (x, y), or transverse plane, while the pseudorapidity is defined as $\eta = -\log[\tan(\theta/2)]$.

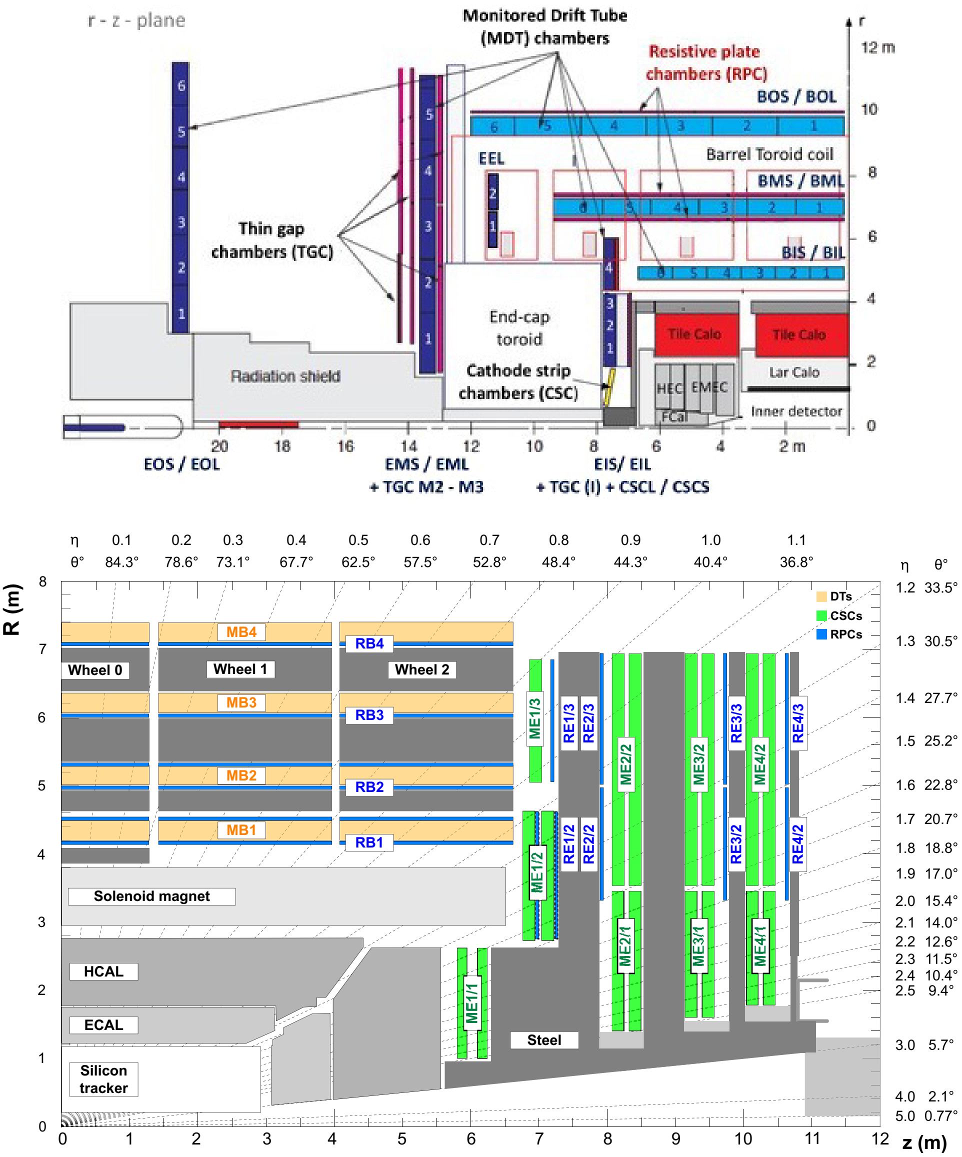
r - z - plane
Monitored Drift Tube (MDT) chambers
Resistive plate chambers (RPC)
BOS / BOL
Barrel Toroid coil
BMS / BML
BIS / BIL
EEL
Thin gap chambers (TGC)
End-cap toroid
Cathode strip chambers (CSC)
Radiation shield
Tile Calo
Tile Calo
Lar Calo
HEC
EMEC
FCal
Inner detector
r
12 m
10
8
6
4
2
0
20
18
16
14
12
10
8
6
4
2 m
EOS / EOL
EMS / EML
+ TGC M2 - M3
EIS/ EIL
+ TGC (I) + CSCL / CSCS
η 0.1 0.2 0.3 0.4 0.5 0.6 0.7 0.8 0.9 1.0 1.1
θ° 84.3° 78.6° 73.1° 67.7° 62.5° 57.5° 52.8° 48.4° 44.3° 40.4° 36.8°
η θ°
1.2 33.5°
1.3 30.5°
1.4 27.7°
1.5 25.2°
1.6 22.8°
1.7 20.7°
1.8 18.8°
1.9 17.0°
2.0 15.4°
2.1 14.0°
2.2 12.6°
2.3 11.5°
2.4 10.4°
2.5 9.4°
3.0 5.7°
4.0 2.1°
5.0 0.77°
DTs
CSCs
RPCs
R (m)
z (m)
Wheel 0
Wheel 1
Wheel 2
MB4
MB3
MB2
MB1
RB4
RB3
RB2
RB1
ME1/3
ME1/2
ME1/1
RE1/3
RE2/3
RE1/2
RE2/2
ME2/2
ME2/1
ME3/2
ME3/1
RE3/3
RE3/2
ME4/2
ME4/1
RE4/3
RE4/2
Solenoid magnet
HCAL
ECAL
Silicon tracker
Steel
0 1 2 3 4 5 6 7 8 9 10 11 12
0 1 2 3 4 5 6 7 8

Fig. 12. Longitudinal views of a quadrant of the ATLAS (top) and CMS (bottom) detectors. Sub-apparati used for the detection of different particles and their positioning are shown.

technologies include drift tubes, cathode strip chambers in the forward regions, resistive-plate chambers, and thin-gap chambers. The CMS muon coverage is $|\eta| < 2.4$ while in ATLAS it is $|\eta| < 2.7$ for tracking and $|\eta| < 2.4$ for trigger chambers.

Events of interest are selected in real time using two-tiered trigger systems in both experiments.[119,120] The first level is composed of specialized hardware processors and uses information from the calorimeters and muon detectors. The second level (high-level) consists of farms of processors running a fast, optimized version of the event reconstruction software that reduce the event rate before data storage. Data are stored in different streams according to which high-level trigger path(s) find compatibility between an event and a specific particle hypothesis (single electron, double muon, etc.).

2.4.2. *Tagging-jet reconstruction*

All VBS processes have in common a pair of jets in the final state, originating from the hard scattering process. These have been precisely defined in Sec. 2.1 and we refer to those jets here as *VBS-tagging jets*.

In ATLAS, jet constituents are topologically-grouped clusters ("topo-clusters") of electromagnetic and hadronic calorimeter cells.[121] In CMS events are reconstructed using a more detailed particle-flow algorithm[122] that identifies each individual particle with an optimized combination of all subdetector information. However, at the very high pseudorapidity values covered by the HF only, a hadron or electromagnetic particle-flow candidate is just defined by its energy release in a η-ϕ HF cell, since information from no other subdetector is available.

In both experiments jets are reconstructed from either particle-flow candidates or topo-clusters using the anti-k_{T} clustering algorithm,[123] as implemented in the FastJet package,[124] with typically a distance parameter of 0.4. This value ensures a good particle containment while reducing the instrumental background, as well as the contamination from pileup. In both ATLAS and CMS identification criteria for jets are very loose and retain almost all physically meaningful jets. Since these jets include leptons with the surrounding QED activity (sometimes referred to as *dressed* leptons), analyses with leptonic final states always require a minimum tagging-jet/lepton ΔR separation in defining their fiducial regions, usually taken equal to the jet distance parameter.

Pileup effects, which are particularly relevant in the forward regions, affect jet measurement in two ways: by adding entire jets that do not originate from the hardest-scattering event (thus requiring *pileup rejection* techniques) and by adding particles in the jet that do not belong to signal jets but overlap in space (requiring *pileup subtraction* techniques). In evaluating both effects, there is an important difference between charged and neutral particles. For charged particles, the hypothesis of being originated in the hardest-scattering *primary vertex* can be evaluated track by track and is based on impact-parameter compatibility.[f] For neutral particles, this association is not possible and subtraction or rejection must be done on a statistical basis. It has to be noted that outside the tracker coverage ($|\eta| < 2.5$ for both ATLAS and CMS) all particles must be treated as neutral.

---

[f] In both ATLAS and CMS, the hardest-scattering vertex is defined as the primary vertex in the event for which the scalar sum of the p_{T}^2 of the associated tracks is maximum.

ATLAS and CMS apply pileup subtraction as part of the jet energy corrections.[125, 126] The subtraction has the analytical form suggested in Ref. 127

$$p_{\mathrm{T}}^{\mathrm{corr}} = p_{\mathrm{T}} - \rho \times A_{\mathrm{jet}}, \tag{8}$$

where ρ is the estimated average pileup p_{T} density in specific regions of the detector and A_{jet} is the jet area. Depending on the experiment and specific analysis, this subtraction can be performed on the original jet, or in combination with charged-hadron subtraction based on vertex compatibility. ATLAS[128, 129] and CMS[130] have dedicated pileup rejection methods. Within the tracking volume, a jet-vertex combined compatibility is computed from the charged tracks found inside a jet, while in the forward regions different jet shapes are employed to build discriminating variables that isolate signal jets from pileup jets. Not all VBS analyses apply selections based on these very recent methods.

Techniques enriching the selected sample with quark-initiated jets over the more abundant gluon-initiated background were studied both in ATLAS[131] and CMS[132] and could be useful in VBS searches. Their limitations, however, reside in the limited resolution and granularity of the subdetectors covering the very forward regions. In ATLAS, performances outside the tracking volume are not even reported, while in CMS they were found to be poor in the forward region.

Requirements on the transverse momentum (p_{T}) of tagging jets, applied after jet energy corrections, vary among the different analyses and can be symmetric or not between the two. Pseudorapidity requirements need to be as loose as possible because of the particular spatial distribution of tagging jets: typically all jets with $|\eta| < 4.5$ (4.7) are selected in ATLAS (CMS). Variables describing kinematics of the jet pair are the most discriminating between VBS and various sources of background. As mentioned previously, typical selections include a minimum rapidity or pseudorapidity difference (Δy_{jj} or $\Delta\eta_{\mathrm{jj}}$, usually taken as unsigned quantities), a minimum invariant mass of the jet pair (m_{jj}) and, in some cases, selection on more complex quantities, like the Zeppenfeld variables that we shall define in the following.

A common choice in case of more than two reconstructed jets in an event is to retain the event if fulfilling the selection, and choose the two jets with the largest p_{T} or energy as the VBS-tagging jets. Both choices have nontrivial implications on the analyses. First of all, a third-jet veto is in principle a powerful handle for background rejection, since the VBS topology implies a rapidity gap between the tagging jets with very little hadronic activity. However, besides possible pileup contributions occurring in the gap, a long-standing theory problem was the observation of large differences in the third-jet kinematics when comparing predictions obtained with some commonly-used parton-shower programs.[23] The origin of these differences has recently been understood (see Sec. 2.3), thus in principle making it possible to include veto techniques in future analyses without being hampered by large theoretical systematic uncertainties. Second, the definition of the tagging jets can be particularly relevant for phase-space regions including heavy-gauge boson resonances decaying into quarks. Such an example is given in Sec. 3.3 when discussing the case of ZZ scattering. Finally, it has to be noted that, as detailed in the next section, in presence of jets originating from heavy gauge-boson decays in the selection, the choice of the tagging jets is not obvious and varies between different analyses.

2.4.3. *Vector-boson reconstruction*

The analysis techniques to reconstruct and select vector bosons in VBS processes depend strongly on the final state under investigation.

High-energy photons (γ) are reconstructed in electromagnetic calorimeters with very high efficiencies. On the other hand, when one or both vector bosons are heavy (W or Z) the reconstruction is based on their decay products and three classes of analyses can be distinguished:

(1) Fully leptonic channels: Heavy gauge bosons decay into the $\mathrm{W}^\pm \to \ell^\pm \nu_\ell$ and $\mathrm{Z} \to \ell^+\ell^-$ final states, where ℓ denotes either an electron or a muon. Even though the branching fractions are approximately only 20% and 6.7%, respectively, these final states are the cleanest and can satisfactorily cover the phase-spaces of all VBS processes. For this reason, all evidences or observations of SM VBS processes so far relies on fully leptonic (or lepton $+\,\gamma$) channels.

The decays of W and Z bosons into τ leptons are not considered in existing analyses because, while having identical branching fractions as electrons and muons, they are much more challenging to reconstruct due to the presence of the missing neutrinos in the τ secondary decays. Nevertheless, the events where the τ decay leptonically can enter the selected samples in the fully leptonic channels. This contamination is much smaller in size than the τ leptonic branching fraction, since secondary leptons from τ decays have smaller transverse momenta and/or fail invariant mass requirements. However, all analyses do (or should in principle) state if this small contribution is considered or not in their definition of fiducial analysis volumes.

In the $\mathrm{W}^\pm \to \ell^\pm \nu_\ell$ case, due to the presence of neutrinos, the process cannot be fully reconstructed. As opposed to the $\mathrm{Z} \to \ell^+\ell^-$ case, it implies that nonresonant contributions also enter the selected sample, and therefore must also be included in the simulation.

(2) Semi-leptonic channels: One heavy gauge bosons is reconstructed from the $\mathrm{W}^\pm \to \ell^\pm \nu_\ell$ or $\mathrm{Z} \to \ell^+\ell^-$ final state, and the other one from the $\mathrm{W}^\pm \to q\bar{q}'$ or $\mathrm{Z} \to q\bar{q}$ final state.

These final states exhibit larger cross-sections because of the higher branching ratios. However, performing a standard reconstruction of the jets from W or Z hadronic decays, as described in Sec. 2.4.2, results in samples overwhelmingly dominated by the production of single-bosons in association with jets, in which sensitivity to SM VBS is negligible compared to fully leptonic channels.

However, special reconstruction techniques apply in case of *boosted* vector bosons, i.e. when their Lorentz γ-factor is large.[133] In particular if the aperture angle of the quark–antiquark pair is $\Delta R \simeq 2/\gamma \simeq 2M(q\bar{q})/p_{\mathrm{T}}(q\bar{q}) < 0.8$, that is for $p_{\mathrm{T}}(q\bar{q}) \gtrsim 220$ GeV, the hadronic decay products of the gauge boson do not cluster into two separated $R = 0.4$ jets but are instead merged into a larger-area jet. In this case, hadronic W and Z decays are identified by anti-k_{T} jets with $R = 0.8$ which contain all the products of the decay. As opposed to standard jets, these *merged* jets have two important characteristics that help distinguishing them from regular-jet background: after removing soft QCD radiation, the invariant mass of all jet constituents peaks at the W or Z mass; and the inner structure of the jet is such that two *subjets* with smaller radii can be identified.

There are two main characteristics in analyses employing boosted vector bosons: first, they usually address mixed final states because jet-mass resolutions are such that W and Z cannot be easily separated. Therefore these final states are indicated by V (indicating generically a vector boson, either W or Z). Second, the requirement $p_{\mathrm{T}}(\mathrm{V}) \gtrsim 220$ GeV implies that only small parts of the SM VBS phase-space are accessible, which compensates for the higher branching fraction. On the other hand, BSM effects in EFT approaches produce cross-sections with larger components in the boosted phase-space as stated in Sec. 2.5. Hence, the most stringent limits on the Wilson coefficients of EFT operators are obtained from semi-leptonic channels.

(3) Fully hadronic channels: Because of the dominant multijet background, these analyses can only be performed for final states with two boosted gauge bosons, VV. While potentially they could have even better sensitivities than semi-leptonic channels on EFT operators, there are no public LHC analyses to date employing these final states.

Lepton and missing energy reconstruction. A brief review of charged-lepton reconstruction follows, which is common to many VBS analyses. Photon and merged-jet reconstruction and selection are specific to some analyses and will be discussed in Sec. 3.

In ATLAS and CMS, muons are reconstructed by combining information from the inner tracking system with the signals in the muon chambers and finding matches between reconstructed tracks in the two detectors. In most analyses, muons must satisfy identification criteria which are called *medium* in ATLAS[134] and *tight* in CMS[135] but in both cases correspond to efficiencies exceeding 90% after fiducial selections. A minimum number of hits in the related subdetectors is required, which rejects fake matchings, as well as kaon and pion decays in flight. Tight primary-vertex compatibility criteria select only *prompt* muons, rejecting those originating from long-lived particle decays. CMS utilizes the transverse and longitudinal track impact parameter d_{xy} and d_z as selection variables for primary-vertex track compatibility, while ATLAS uses the significance of the impact parameter in the transverse plane $|d_{xy}/\sigma_{d_{xy}}|$ and the vertex-track distance computed from the longitudinal impact parameter, $d_z \sin\theta$, with tighter requirements. Isolation requirements, further reducing the B- and D-meson decay background, are in general loose for both experiments.

Similarly, in both ATLAS and CMS, electron reconstruction combines information from inner-detector tracks and electromagnetic energy clusters. Primary vertex compatibility of the electron track is evaluated in a similar way as for muons, with equal or tighter requirements. However, identification criteria, again defined as *medium* in ATLAS[136,137] and *tight* in CMS,[138] are more complex in order to cope with potentially large backgrounds of misidentified photons and jets. These criteria involve many aspects of the reconstruction, including: angular and energy–momentum matching between track and cluster, electromagnetic shower shape variables, energy ratios between the central cluster cell and the surrounding ones, and maximum energy released in hadronic calorimeters in close-by regions of the detector. In ATLAS, these criteria are combined using a likelihood-ratio method, while in CMS selections are either applied sequentially or combined in a Boosted-Decision Tree (BDT).[g] Electron isolation considers separately the energy/momentum reconstructed around the electron direction in trackers, electromagnetic calorimeters, and hadronic calorimeters, taking into account possible *bremsstrahlung* effects in the traversed detectors: isolation requirements are part of the CMS identification criteria, while they are applied separately in ATLAS. Total efficiencies are lower than for muons, ranging in about 80%–85% for typical electrons from W or Z decays.

The only analyses significantly departing from the above choices are those having 4ℓ in the final state, because the simultaneous presence of four charged leptons removes many types of backgrounds and looser selections can be used to recover efficiency.

Another important ingredient in the case of final states involving one or more $\mathrm{W}^{\pm}$ boson(s) is the reconstruction of the missing transverse momentum $p_{\mathrm{T}}^{\mathrm{miss}}$, that can be identified as the (total) transverse momentum of the undetected high-energy neutrino(s). In both ATLAS and CMS this is defined as the opposite of the vector sum of all reconstructed particle momenta, so its precise determination depends on all energy/momentum corrections applied to visible particles and in particular to jets.[140,141]

2.4.4. *Monte Carlo simulation*

Monte Carlo (MC) simulation of VBS signals and backgrounds which cannot be estimated from data-driven techniques (e.g. QCD background, which has inherently the same signature) is an essential ingredient of experimental analyses.

---

[g] A decision tree is an algorithm which takes a set of input features and splits input data recursively based on those. Boosting is a machine-learning method which combines several decision trees to make a stronger signal-background classifier. BDT algorithms are coded in commonly used programs like TMVA[139] or Keras (`https://keras.io`).

Regarding simulations at NLO QCD, matched to parton shower or merged with higher parton multiplicities, the most used generator tools for physics events are MG5_aMC,[49] version 2.3 (v2.3) and above, POWHEG[88,89,142] v2, and Sherpa[143] v2.1 and above.

Generation parameters can vary in different processes and experimental analyses, but there are some common choices. In general, the central renormalization and factorization scales are set automatically by MG5_aMC to the central m_{T}^2 scale after k_{T}-clustering of the event, while in POWHEG and Sherpa the default choice is process-dependent (for diboson and VBS processes a common choice is to use the diboson invariant mass). Uncertainties from renormalization and factorization scales are mostly derived from the 7*-fold scale variation scheme*, where both are varied independently by a factor of two up and down, but avoiding the cases where the two vary in opposite directions (that is, differ by a factor four).

Quite peculiarly, in CMS, the standard sets of parton distribution functions (PDFs) used are different for the simulation of the 2016 detector conditions (NNPDF3.0 NLO) and for the 2017–2018 conditions (NNPDF3.1 NNLO). In ATLAS, the NNPDF3.0 NNLO PDF set is used in most cases. The estimation of PDF uncertainties follows prescriptions from the NNPDF collaboration.[144]

While Sherpa has an internal parton shower (PS) and underlying-event program, other Monte Carlo generators need an external tool providing PS, which are usually Pythia8[83] or HERWIG.[86] Underlying-event tuning is slightly different in the two experiments and tunes have also been updated in some cases during the course of Run-2.[145,146]

Detector simulation is obtained through the GEANT4 software[147,148] in both experiments.

2.5. *Impact on Beyond-the-Standard-Model theories*

VBS studies can constrain the existence of Beyond-the-Standard-Model (BSM) physics in several ways, which are reviewed in detail in Ref. 12. Therefore, in the present review we simply restrict ourselves to outline the main results obtained at the LHC. Searches for new physics in VBS channels can be divided into those based on an explicit (and possibly simplified) new physics model and general model-independent searches, usually parameterized as Effective Field Theories (EFTs).[149]

EFT constraints obtained in experimental analyses, in ATLAS and CMS, use the parameterization of Refs. 150 and 151, where dimension-8 operators are considered. Unlike at dimension-6, where quartic and trilinear gauge couplings are intrinsically related, at dimension-8 one can assume the presence of anomalous quartic gauge couplings (aQGC) and no anomalous triple gauge couplings (aTGC). There are 18 independent bosonic dimension-8 operators relevant for two-to-two scattering processes involving Higgs or gauge bosons at tree level, and conserving parity and charge conjugation. They can be classified as *scalar*, *mixed*, and *transverse* according to the number of gauge-boson strength fields contained in the operator (0, 2, and 4, respectively). Several CMS Run-2 analyses constrain physics from nonzero dimension-8 operators, while ATLAS Run-2 measurements mostly focus on SM VBS observations and do not provide explicit constraints on BSM physics: ATLAS results using the same model are however available in 7 TeV and 8 TeV analyses.

All these operators have the common feature that nonzero Wilson coefficients lead to modifications of the high-energy tail of differential distributions of the scattering process. Therefore, in the experimental analyses, events are first selected in VBS enhanced phase-space regions; second, in the selected sample, a distribution sensitive to this modification is used to set constraints on the couplings. At the LHC, such distributions include the invariant mass of the diboson system (or approximations based on reconstruction of the missing neutrino flight directions), or the transverse momentum of either scattered gauge boson.

Figures 13–15 show a compilation of the existing limits on dimension-8 operator couplings. The couplings are defined as the ratio of the Wilson coefficient and the power of the EFT new-physics scale appropriate for dimension-8 operators. They are therefore expressed in units of TeV^{-4}. As stated in Sec. 2.4, semi-leptonic signatures are an experimental challenge, but in most cases provides the strongest handle on dimension-8 EFT operators. For transverse operators, different final states can be more or less sensitive to specific sets of operators, as only those with the correct combination of gauge fields contribute to the related aQGC vertices. Exclusive

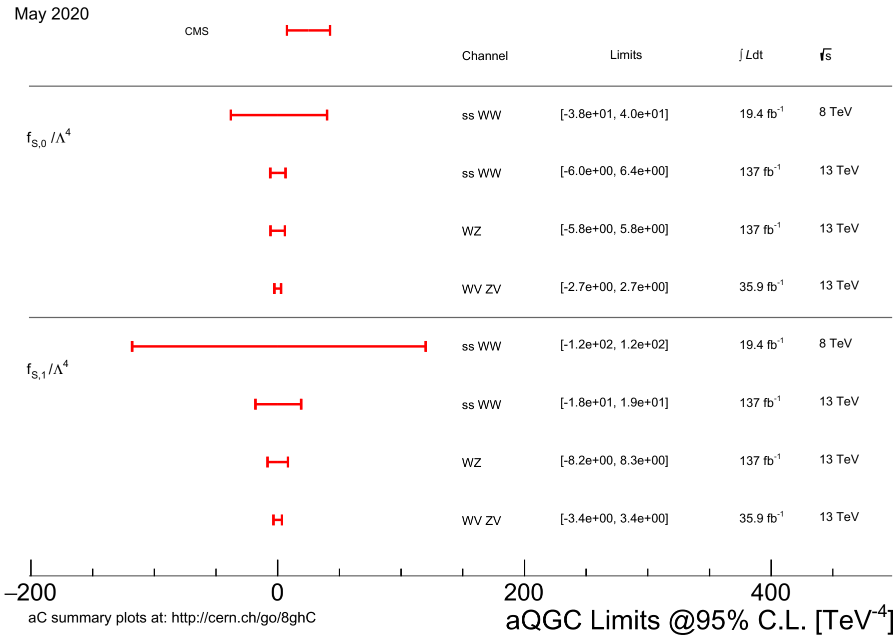

Fig. 13. (Color online) Current constraints on scalar dimension-8 operator couplings from various ATLAS (blue) and CMS (red) analyses at 7, 8, and 13 TeV, with corresponding integrated luminosities. The figure is taken from Ref. 153.

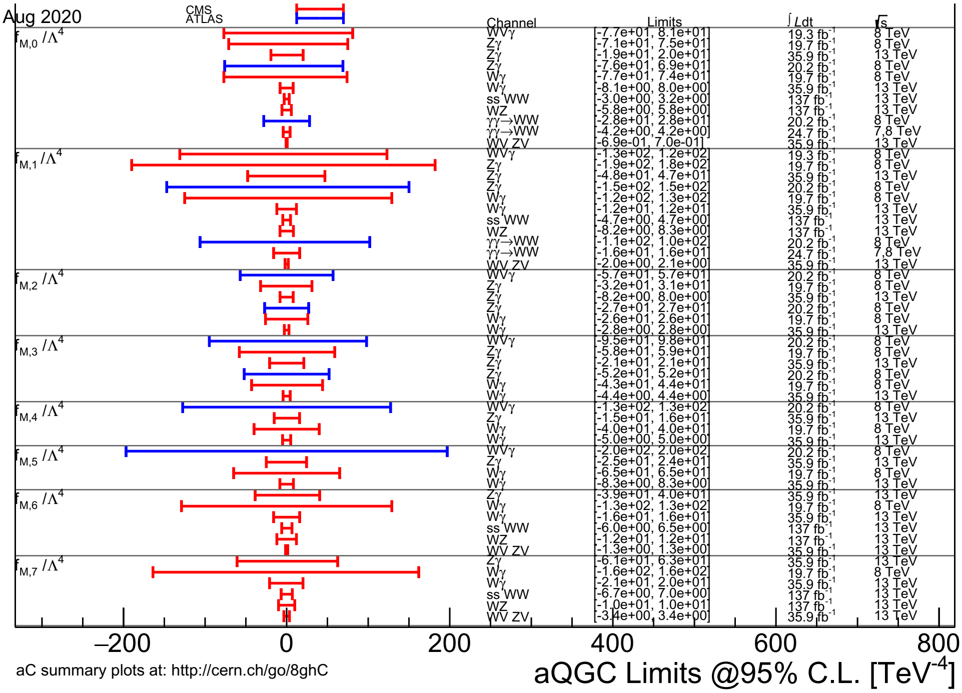

Fig. 14. (Color online) Current constraints on mixed dimension-8 operator couplings from various ATLAS (blue) and CMS (red) analyses at 7, 8, and 13 TeV, with corresponding integrated luminosities. The operator M,6 is reported but recently found to be redundant and hence not independent from other mixed operators.[154] The figure is taken from Ref. 153.

production, discussed in Sec. 3.7, gives the best results for operators sensitive to the $\gamma\gamma$WW interaction. It is important to notice that the presence of nonzero aQGCs would violate tree-level unitarity at sufficiently high-energy. Limits that take this effect into account can be set by cutting off the EFT integration at the unitarity limit and just considering the expected SM contribution for generated events with diboson invariant masses above the unitarity limit. The unitarity limits for each aQGC parameter, typically about 1.5–2.5 TeV, are usually calculated using the VBFNLO program[152] or taken from Ref. 151. These limits are typically less stringent than the naive ones, where the unitarity violation is not taken into account.

If existing, BSM physics is unlikely to be confined to VBS processes. The choice of selecting operators generating aQGC in the absence of aTGC is therefore not obvious, as it somehow breaks the EFT paradigm where operators with lower powers of Λ should be constrained first, while data are not excluding yet all possible aTGC. Moreover, in most VBS processes, aTGC effects enter directly, for example through specific s-channel diagrams. In a dimension-6 realization of the EFT, operators affecting VBS analyses are also relevant for non-VBS VV production, triple-gauge boson and Higgs boson production. They should eventually therefore be constrained

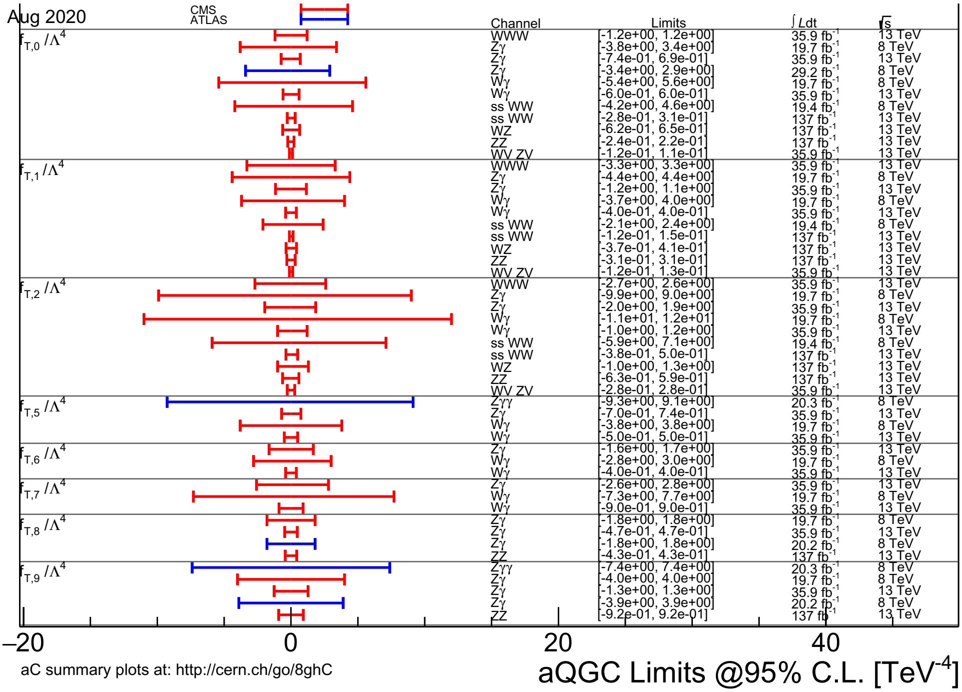

Fig. 15. (Color online) Current constraints on transverse dimension-8 operator couplings from various ATLAS (blue) and CMS (red) analyses at 7, 8, and 13 TeV, with corresponding integrated luminosities. The figure is taken from Ref. 153.

together in a larger-scope fit. Studies of dimension-6 effects on specific VBS final states can be found in Refs. 81, 155 and 156. Advancing in this direction, a very recent phenomenological work[157] attempts a parameterization of many existing VBS results and compares the limits on several Wilson coefficients considering just inclusive VV production versus inclusion of VBS, finding $15\% - 50\%$ weaker constraints when VBS is not included, depending on the specific operator.

In explicit BSM models, new resonances in the EW sector would also likely couple to the vector bosons and Higgs boson such that many other production mechanism would be impacted. Therefore, searches for new physics in diboson and Higgs events have strong implications for new physics searches in VBS channels. Of the many possible models predicting modifications to the EW sector, those involving additional Higgs bosons with narrow or broad natural widths are of particular interest. In the particular cases where couplings of the new resonances to fermions are suppressed or absent, in fact, the main production and decay modes would produce signals that are experimentally equivalent to VBS, but with resonant VV invariant masses. As these analyses are part of a more general search program in ATLAS and CMS, also involving other production mechanisms and final states, they will not be further reviewed here.

3. VBS Processes at the LHC

3.1. *The $W^{\pm}W^{\pm}jj \to \ell^{\pm}\nu\ell'^{\pm}\nu jj$ final state*

The $\mathrm{W}^{\pm}\mathrm{W}^{\pm}$jj process is considered to be the *golden channel* in the study of VBS. The cross-section ratio of the EW component containing the VBS production compared to the QCD one is very large (see Sec. 2.1 for a precise definition of the EW and QCD contributions), of order 4–6 in typical fiducial regions, while it is usually $\ll 1$ for other processes. This is due to charge conservation which prevents gluon-initiated processes in the QCD background as opposed to $\mathrm{W}^{\pm}$Zjj, ZZjj, or $\mathrm{W}^{+}\mathrm{W}^{-}$jj. In addition, the application of particular event selections allows to further enhance the EW component of the cross-section (also see Sec. 2.1). For this reason, the $\mathrm{W}^{\pm}\mathrm{W}^{\pm}$jj channel is the most sensitive to potential new-physics effects, including those affecting polarization and anomalous quartic gauge couplings.

3.1.1. *Theoretical calculations*

From a theoretical point of view, the $\mathrm{W}^{\pm}\mathrm{W}^{\pm}$jj channel is without a doubt the most accessible one, because of the reduced number of partonic channels and Feynman diagrams. Calculations started already 10 years ago with the computation of the QCD corrections to the EW process at order $\mathcal{O}(\alpha_{\mathrm{s}}\alpha^{6})$ in the VBS approximation.[66,158] Such corrections have been then matched to parton shower in programs such as POWHEG[79] or VBFNLO.[152,159,160] The QCD background is also known since some time at NLO[161,162] and has been matched to PS.[163] Only recently the NLO EW corrections of order $\mathcal{O}(\alpha^{7})$ have been computed[100] and found to be large. The full tower of NLO corrections has been computed a few months later in Ref. 24. Given the size of the EW corrections, these have been implemented in the computer program POWHEG[103] so that they can be combined with other matched predictions.

As $\mathrm{W}^{\pm}\mathrm{W}^{\pm}$jj is a representative channel for all VBS processes, in Ref. 23 several computer programs[35,49,88,89,142,152,159,160,164–166] have been used for a comparative study of fixed and matched predictions. One of the main findings of this study is that different NLO QCD predictions matched to parton shower can vastly differ for observables involving the third jet (i.e. a nontagging jet). This is particularly apparent on the right-hand side of Fig. 16. Nonetheless, we would like to emphasize that, upon using Pythia8 with the correct recoil scheme or Herwig, reliable predictions can be obtained even for the third-jet observables. This has been discussed in Sec. 2.3 and studied in detail in Ref. 78 for Higgs production via VBF. It implies that jet veto in central regions can be used in experimental analysis provided that good care is taken in using appropriate theoretical predictions. The second main finding of this study is that the VBS approximation is good up to few percent for typical VBS event selections. This implies that the VBS approximations at fixed order or used in combination with parton shower are reliable as long as selection cuts are able to suppress non-VBS contributions such as tri-boson contributions (see further discussion in Sec. 3.3).

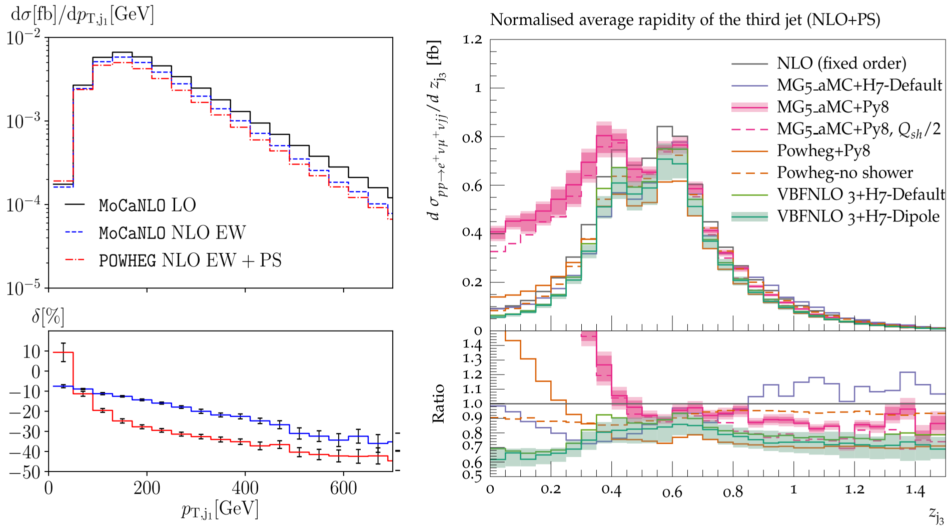

Fig. 16. Differential distributions for the $W^{\pm}W^{\pm}$jj channel. Left: transverse momentum of the hardest jet with LO, NLO EW, and NLO EW + PS accuracy. Right: normalized average rapidity of the third jet at NLO QCD + PS accuracy for different predictions. These figures are taken from Refs. 103 and 23, respectively.

After the publication of Ref. 23, other comparative studies have appeared.[167,168] It should be made clear that, while the former study was a tuned comparison among the different event generators, where all the parameters relevant for the partonic cross-sections were identical, this is not always the case for the latter studies. In the first case, discrepancies among predictions are unambiguously due to the different shower and hadronization models of the Monte Carlo programs. In the second case a certain degree of ambiguity remains in the origin of the discrepancies, which may jeopardize a proper understanding of these effects.

A summary of the available predictions is provided in Table 1. If it fair to say that the theoretical status is rather good, given the experimental accuracy available now and expected in the next 10 years. In particular, almost all NLO orders matched to parton shower are known. The only exception is the order $\mathcal{O}(\alpha_s^2\alpha^5)$, which has been shown in Ref. 24 to be suppressed. Also the order $\mathcal{O}(\alpha_s\alpha^6)$ matched to PS is only known in the VBS approximation. Nonetheless, provided that typical VBS phase-space regions are used this should be a very good one. Going beyond this approximation would require a method to match mixed-type corrections, which is currently not existing.

3.1.2. *Experimental approaches*

Both ATLAS and CMS have reported the observation of EW $W^{\pm}W^{\pm}$jj production using a partial 13 TeV dataset.[169,170] CMS has already published the same search on the full dataset, in combination with the $W^{\pm}$Zjj final state.[25]

Table 1. Summary of higher-order predictions currently available for the ss-WW channel: at fixed order and matched to parton shower. The symbols ✓, ✓*, and **X** means that the corresponding predictions are available, in the VBS approximation, or not available yet.

Order	$\mathcal{O}(\alpha^7)$	$\mathcal{O}(\alpha_s\alpha^6)$	$\mathcal{O}({\alpha_s}^2\alpha^5)$	$\mathcal{O}({\alpha_s}^3\alpha^4)$
NLO	✓	✓	✓	✓
NLO+PS	✓	✓*	**X**	✓

Monte Carlo simulation. ATLAS and CMS use Monte Carlo simulations to evaluate the signal and several background contributions to the selected data samples.

CMS uses the MG5_aMC generator,[49] version 2.4.2 to simulate the EW, strong, and interference components separately at LO. All samples have no extra partons beyond the two quarks in the simulated process and are hence inclusive in the number of extra jets. The interference is estimated to be about 4% of the signal and is included in the signal yield. Since the CMS analysis is more recent, it could benefit from the complete application of NLO QCD+EW corrections computed in Ref. 24 (see previous section), that decrease the cross-sections by 10%–15%, the correction being larger at higher values of m_{jj} and $m_{\ell\ell'}$. Similar settings are used to simulate the W$^{\pm}$Zjj component, that is analyzed together in a single study. Other minor backgrounds, including tribosons, processes with at least a top quark (t$\bar{\mathrm{t}}$, t$\bar{\mathrm{t}}$W, t$\bar{\mathrm{t}}$Z, tW, tZq, etc.) as well as other diboson processes, are simulated with either POWHEG[88,89,142] or MG5_aMC, mostly with inclusive NLO QCD accuracy.

ATLAS uses the Sherpa generator, version 2.2.2[143] to simulate the EW, strong and interference processes at LO. All samples are simulated with up to 1 extra parton beyond the two quarks and the 0- and 1-parton processes are merged using the MEPS matching scheme included in Sherpa. The interference is estimated to be about 6% of the signal. An alternative description of the VBS signal process is obtained using POWHEG at NLO in QCD.[66] A large difference between the two theoretical fiducial cross-sections is found.[h] We believe that these differences should be investigated beyond the work done in Ref. 167 (see remarks in the previous section, as well as in the corresponding part of Sec. 3.2 for W$^{\pm}$Zjj). Other backgrounds considered (in general the same as CMS, but with more emphasis on $V\gamma$ and EW $V\gamma$jj, which are found to be an important contribution to the background) are generated using different tools, perturbative accuracies, and extra-parton multiplicities.

Fiducial region definitions and reconstruction-level selections. Fiducial regions considered in the ATLAS and CMS analyses are compared in Table 2. In both analyses leptons from τ decays are not considered in the fiducial region and

---

[h] In Ref. 171, it has been documented that there was an issue in Sherpa regarding the color flow setup when using parton shower for VBS-like processes. To our knowledge this issue has been resolved, but the corresponding results have not yet appeared in any further publication.

Table 2. Comparison of $W^{\pm}W^{\pm}$jj fiducial region definitions and related EW (VBS) cross-section values in the ATLAS and CMS measurements.[25, 169] JRS stands for generic Jet-Rapidity Separation selections. ATLAS σ_{LO} has the issues reported in the text.

Variable	ATLAS	CMS
$p_{\mathrm{T}}(\ell)$	>27 GeV	>20 GeV
$\|\eta(\ell)\|$	<2.5	<2.5
$\Delta R(\ell\ell')$	>0.3	—
$m_{\ell\ell'}$	>20 GeV	>20 GeV
$p_{\mathrm{T,miss}}$	>30 GeV	—
$p_{\mathrm{T}}(\mathrm{j})$	>65/35 GeV	>50 GeV
$\|\eta(j)\|$	<4.5	<4.7
m_{jj}	>500 GeV	>500 GeV
JRS	$\Delta y_{\mathrm{jj}} > 2$	$\Delta\eta_{\mathrm{jj}} > 2.5$
σ_{LO}	$2.0^{+0.3}_{-0.2}$ fb	3.9 ± 0.6 fb
σ_{NLO}	$3.1^{+0.4}_{-0.5}$ fb (NLO QCD)	3.3 ± 0.5 fb (NLO QCD+EW)

lepton momenta are corrected by adding possible final-state photon radiations in a cone of $\Delta R < 0.1$ around the lepton direction.

Reconstruction-level selections follow closely the definition of the fiducial regions. In both analyses, events are selected at the trigger level by the presence of just one electron or muon, in order to increase efficiency. Both experiment veto events with jets likely originated from a bottom quark, in order to reject backgrounds featuring top-quark decays. CMS requires that the leading lepton has $p_{\mathrm{T}} > 25\,\mathrm{GeV}$, and that $p_{\mathrm{T,miss}} > 30$ GeV. In both ATLAS and CMS, background from wrong charge reconstruction in $\mathrm{e}^{\pm}\mathrm{e}^{\pm}jj$ events is reduced by requiring $|m_{\mathrm{ee}} - m_{\mathrm{Z}}| > 15$ GeV, and in ATLAS dielectron events with $|\eta(\mathrm{e})| > 1.4$ are also rejected. In CMS the maximum Zeppenfeld variable z^*_ℓ of the two leptons must be smaller than 0.75, where:[172]

$$z^*_\ell = \left| \frac{\eta(\ell) - [\eta(\mathrm{j}_1) + \eta(\mathrm{j}_2)]/2}{\Delta\eta_{\mathrm{jj}}} \right| . \tag{9}$$

Analysis strategy and background estimation. Both experiments fit the observed data after estimating backgrounds from either simulation or control regions. In ATLAS, the contribution from *nonprompt leptons* is estimated in different control regions, depending if they are originated from heavy-flavored meson decays or from $V\gamma$ events with photon conversions (only for final states with electrons). Such regions are enriched in $\mathrm{b\bar{b}}$ events and γ from final-state radiation in Z decays, respectively. CMS uses events which pass the final selection except for one rejected lepton, which is selected with looser requirements to enter the control region and further validates nonprompt leptons from heavy-flavor decays by inverting the b-jet veto. WZ events are fit together in the CMS analysis, while in ATLAS the normalization of a control region with 3ℓ selected events is floated in the fit. Both analyses use fully selected events with $200 < m_{\mathrm{jj}} < 500\,\mathrm{GeV}$ to constrain background-component normalizations.

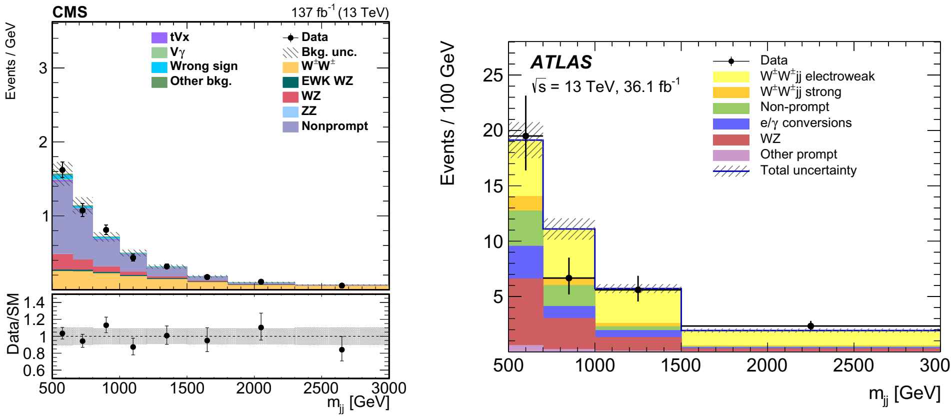

Fig. 17. Post-fit m_{jj} distributions in CMS (left) and ATLAS (right) in the $\mathrm{W^{\pm}W^{\pm}jj}$ analysis. *Nonprompt* in CMS includes the photon conversion background. In ATLAS, *e/γ conversions* includes events with wrong-sign electron reconstruction.

In the ATLAS analysis the signal-region data in four m_{jj} bins with different signal purities are fit together with the 3ℓ and the low-m_{jj} regions, in order to optimize significance. In CMS, which analyzes a larger dataset, a similar technique is used, but using two-dimensional distributions in bins of m_{jj} and $m_{\ell\ell'}$ in the signal region and three control regions, leaving free in the fit the normalization of two on them, in addition to the EW and strong cross-sections.

The ATLAS and CMS data with superimposed signal and background components are shown in Fig. 17. While the labeling of the process composition is different, its relative amount is similar between the two analyses, CMS exhibiting more nonprompt background because of the softer lepton selections.

Systematic uncertainties. Both ATLAS and CMS list systematic uncertainties according to their impact on the measured cross-sections. In CMS the dominant uncertainties come from the estimate of the nonprompt background, the limited size of simulated samples in the two-dimensional distributions, and theoretical errors on the various simulated components. In ATLAS, similar uncertainties are considered, but a larger impact from jet-energy corrections and the related $p_{\mathrm{T,miss}}$ measurement is present. No single contribution has an impact larger than 4% in either analysis.

Results. ATLAS reports a measured VBS fiducial cross-section of $\sigma_{\mathrm{EW}} = 2.89^{+0.59}_{-0.55}\,\mathrm{fb}$, where the total uncertainty is dominated by the statistical one, in agreement with the NLO QCD estimate of the SM cross-section. It corresponds to a background-only hypothesis rejection with a significance of 6.5σ.

CMS similarly reports $\sigma_{\mathrm{EW}} = 3.98 \pm 0.45\,\mathrm{fb}$, also statistically dominated and in agreement with the NLO QCD+EW estimation in the respective fiducial region. It corresponds to a background-only hypothesis rejection with a significance much larger than 5σ. The total $\mathrm{W^{\pm}W^{\pm}jj}$ cross-section including EW and strong components is also measured to be $\sigma_{\mathrm{tot}} = 4.42 \pm 0.47\,\mathrm{fb}$.

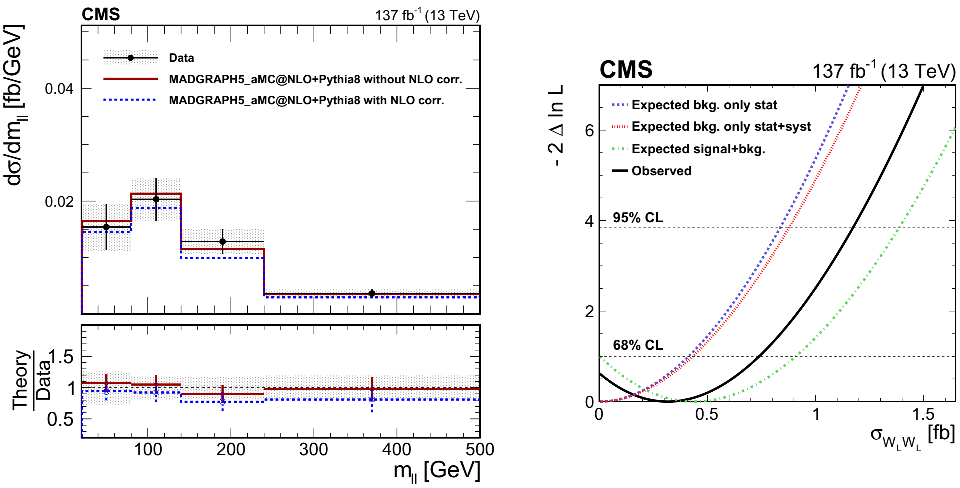

Fig. 18. CMS $W^{\pm}W^{\pm}jj$ analysis. Left: EW differential cross sections as a function of $m_{\ell\ell'}$ measured in data, in LO and NLO-corrected simulation. Right: likelihood scan as a function of the cross-section of $W^{\pm}_{L}W^{\pm}_{L}$ events.

Differential cross-sections in four bins of m_{jj}, $m_{\ell\ell'}$ and the leading lepton p_{T} are obtained by fitting simultaneously the corresponding regions of the phase-space, with negligible bin-migration effects, and when needed replacing the fitted observables with the ones under study. All the results are in agreement with SM expectations, although the experimental uncertainties are of the order of 20% because of limited statistics. Figure 18(left) shows the EW differential cross sections as a function of $m_{\ell\ell'}$.

Constraints on aQGC are set by fitting the diboson transverse mass distribution[i] in the signal region: no BSM excess is found and the limits set on $f_{T,0}$, $f_{T,1}$, $f_{T,2}$, $f_{M,0}$, $f_{M,1}$, $f_{M,7}$, and $f_{S,0}$ are the world second-best limits after the CMS semi-leptonic VBS analysis.

Polarization measurement. In a separate analysis, CMS[173] examines the same selected dataset in order to measure the polarization of W bosons in $W^{\pm}W^{\pm}jj$ events. The analysis is identical to the previously described CMS results, for what concerns the simulation and estimation of the backgrounds, event selection, systematic uncertainties, and fitting techniques.

Polarized signal for the three possible combinations $W^{\pm}_{\mathrm{L}}W^{\pm}_{\mathrm{L}}$, $W^{\pm}_{\mathrm{L}}W^{\pm}_{\mathrm{T}}$, and $W^{\pm}_{\mathrm{T}}W^{\pm}_{\mathrm{T}}$ are generated using a new version of MG5_AMC.[48] The two-dimensional fits use different variables than in the original analysis: both are output scores of BDT algorithms, an *inclusive* one optimized to select EW $\mathrm{W}^{\pm}\mathrm{W}^{\pm}\mathrm{jj}$ over backgrounds, and a *signal* BDT defined in two versions, alternatively optimized to select purely longitudinal or longitudinal-unpolarized ($\mathrm{W}^{\pm}_{\mathrm{L}}\mathrm{W}^{\pm}_{X}$) signals over other polarization combinations. Training variables, besides those already used in the event selection, include the transverse mass, p_{T}, angular or ΔR separations between leptons and jets, and the ratio of p_{T} products between leptons and jets.

---

[i] The diboson transverse mass is defined as $m_{\mathrm{T}}(\mathrm{WW}) = \sqrt{(\Sigma E_i)^2 - (\Sigma p_{z,i})^2}$, where E_i and $p_{z,i}$ are the energies and z components of the momenta of all particles from the decay of the W in the event. The four-momentum of the di-neutrino system is defined using the $p_{\mathrm{T,miss}}$ vector and assuming that the values of the longitudinal component of the momentum and the invariant mass are zero.

The resulting cross-sections of $\sigma_{\mathrm{fid}} = 1.2^{+0.6}_{-0.5}\,\mathrm{fb}$ for the $\mathrm{W}^{\pm}_{\mathrm{L}}\mathrm{W}^{\pm}_{X}$ process and $\sigma_{\mathrm{fid}} < 1.17\,\mathrm{fb}$ at the 95% Confidence Level (CL) for the $\mathrm{W}^{\pm}_{\mathrm{L}}\mathrm{W}^{\pm}_{\mathrm{L}}$ process are in agreement with the SM. There is not yet an evidence even for a single-boson polarization state, the significance of the $\mathrm{W}^{\pm}_{L}\mathrm{W}^{\pm}_{X}$ background-hypothesis rejection being only 2.3σ. Figure 18(right) shows the likelihood scan as a function of the cross-section of $\mathrm{W}^{\pm}_{\mathrm{L}}\mathrm{W}^{\pm}_{\mathrm{L}}$ events. Results are also extracted by considering polarization eigenstates not in the default helicity frame, but in the colliding-parton frame. Results in both frames have been found to be comparable.

3.2. *The $W^{\pm}Zjj \to \ell^{+}\ell^{-}\ell'^{\pm}\nu jj$ final state*

The $\mathrm{W}^{\pm}\mathrm{Zjj}$ VBS process has a larger cross-section than $\mathrm{W}^{\pm}\mathrm{W}^{\pm}\mathrm{jj}$, which becomes however comparable when considering the much less abundant leptonic Z decays. In addition, production with at least two strong vertices is a dominant background, because $\mathrm{W}^{\pm}\mathrm{Z}$ production at the LHC is possible from a quark–antiquark initial state at tree level, and NLO QCD corrections resulting in two-jet events are fairly large. Therefore searches for this VBS process are much more challenging, with typical signal-to-background ratios of 1/10, and require advanced analysis techniques.

3.2.1. *Theoretical calculations*

With respect to the $\mathrm{W}^{\pm}\mathrm{W}^{\pm}\mathrm{jj}$ channel, $\mathrm{W}^{\pm}\mathrm{Zjj}$ is more complicated as it has more partonic channels and more involved Feynman diagrams. Therefore, the state-of-the-art in the theoretical knowledge is not as advanced as for $\mathrm{W}^{\pm}\mathrm{W}^{\pm}\mathrm{jj}$. Nonetheless, QCD corrections have been known for some time in the VBS approximation[65] and have also been matched to parton shower.[82] The QCD background is also known at NLO QCD accuracy since some time[174] and NLO predictions matched to parton shower can nowadays be obtained from automatized tools.

Recently the full NLO computations for the orders $\mathcal{O}(\alpha^7)$ and $\mathcal{O}(\alpha_{\mathrm{s}}\alpha^6)$ have been obtained.[67] It is worth noticing that it confirmed that the EW corrections are in general large for VBS processes at the LHC. Such results can for example be seen in the left-hand side of Fig. 19.

Along the lines of Refs. 23 and 82 showed that the details of the parton shower can be particularly relevant for phenomenological studies. In addition, the authors showed that the effect of hadronization and multiple-parton interaction can be significant, especially for observables involving the third jet. This is exemplified in the right hand-side of Fig. 19.

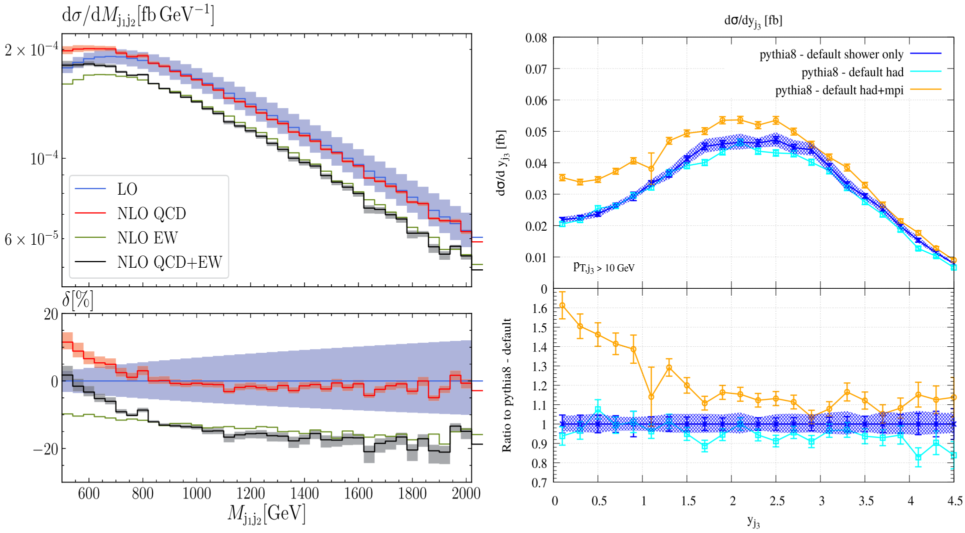

Fig. 19. Various differential distributions for the WZ channel. Left: invariant mass of the two tagging jets with NLO EW + QCD corrections. Right: Zeppenfeld variable for the third jet at NLO QCD + PS accuracy including hadronization or multiple-parton interaction. These figures are taken from Refs. 67 and 82, respectively.

Finally, in the proceedings of Les Houches 2017,[175] a tuned comparison of theoretical predictions up to LO+PS accuracy has been performed. It highlights the same features as the NLO comparative study of $W^{\pm}W^{\pm}jj$.[23] In particular, all differential distributions are in very good agreement at LO and LO+PS accuracy, the only exception being, as in Ref. 23, observables involving the third jet. It is worth emphasizing that the SHERPA predictions of Ref. 175 are LO or LO+PS predictions and are thus different from the SHERPA predictions usually adopted by the ATLAS collaboration, for example in Ref. 176, the latter being merged predictions with 2 and 3 jets matched to PS and largely differing from other predictions.

A summary of the available predictions is provided in Table 3. It is perfectly reasonable to expect that the accuracy obtained for the $W^{\pm}W^{\pm}jj$ channel can be also achieved in the next few years for the $W^{\pm}Zjj$ channel.

Table 3. Summary of higher-order predictions currently available for the WZ channel: at fixed order and matched to parton shower. The symbols ✓, ✓*, and **X** means that the corresponding predictions are available, in the VBS approximation, or not yet.

Order	$\mathcal{O}(\alpha^7)$	$\mathcal{O}(\alpha_s\alpha^6)$	$\mathcal{O}(\alpha_s{}^2\alpha^5)$	$\mathcal{O}(\alpha_s{}^3\alpha^4)$
NLO	✓	✓	**X**	✓
NLO + PS	**X**	✓*	**X**	✓

3.2.2. *Experimental approaches*

ATLAS has reported observation of EW $W^{\pm}Zjj$ production using a partial Run-2 dataset.[177] CMS performed the same search on the full dataset, in combination with the $W^{\pm}W^{\pm}jj$ final state,[25] also leading to an observation of this process.

Monte Carlo simulation. Since the CMS study combines the $W^{\pm}W^{\pm}jj$ and $W^{\pm}Zjj$ final states, the simulations use the same settings as in the previous section. The EW-QCD interference is positive and estimated to be 1% of the EW signal in the fiducial region. The QCD-induced $W^{\pm}Z + \text{jets}$ background is simulated at LO with up to three additional partons using MG5_aMC, merging the jet multiplicities according to the MLM scheme,[178] and normalizing the total cross-section to diboson NNLO QCD predictions.[179,j]

ATLAS uses Sherpa, version 2.2.2, to simulate the EW process at LO, inclusive in the number of jets, while the strong process is simulated at NLO QCD with up to one extra jet. The interference is estimated separately with MG5_aMC at LO to be about 10% of the EW signal, in noticeable disagreement with the CMS estimation. Nevertheless, its full amount is conservatively used as an uncertainty. Alternative descriptions of the EW and strong processes are obtained using MG5_aMC at LO or POWHEG at NLO in QCD.[180] Other backgrounds, such as ZZ, tribosons, $t\bar{t}W^{\pm}$, and $t\bar{t}Z$ are generated using different tools, QCD accuracies, and extra-parton multiplicities.

Fiducial region definitions and reconstruction-level selections. Fiducial regions considered in the ATLAS[k] and CMS analyses are compared in Table 4. The same assumptions as in $W^{\pm}W^{\pm}jj$ are used for τ decays and lepton "dressing".

Reconstruction-level selections follow the fiducial regions requirements. Both analyses use single-lepton triggers and use a b-jet veto. In ATLAS (CMS) the leading lepton is required to have $p_T > 27(25)\,\text{GeV}$, and both experiments require $p_{T,\text{miss}} > 30\,\text{GeV}$. In ATLAS 4ℓ events are explicitly vetoed, while CMS requires that $m_{\ell\ell\ell'} > 100\,\text{GeV}$. In CMS the maximum z^*_ℓ of the three leptons must be smaller than 1.

Analysis strategy and background estimation. Both ATLAS and CMS use BDT algorithms to isolate the EW signal over the large QCD background, combining 11 to 12 variables that are related to jet kinematics, vector-boson kinematics, or to both jets and leptons kinematics at the same time. It must be noticed that

---

[j] In the cases where QCD background is the dominant component, it is a common experimental practice to simulate all parton multiplicities starting from zero, even if only 2-jet events should in principle pass selections, provided the PS-matching scale is lower than the jet p_T thresholds. This ensures that events with nonsignal (fake or pileup) jets are correctly taken into account in the simulation.

[k] All ATLAS cross-sections are reported for a single lepton flavor and are therefore multiplied by four to compare to CMS.

Table 4. Comparison of $W^{\pm}Zjj$ fiducial region definitions and related EW (VBS) cross-section values in the ATLAS and CMS measurements.[25,177] JRS stands for generic Jet-Rapidity Separation selections.

Variable	ATLAS	CMS
$p_T(\ell)$	$> 20/15/15$ GeV	> 20 GeV
$\|\eta(\ell)\|$	< 2.5	< 2.5
$\Delta R(\ell\ell')$	$> 0.3/0.2$	-
$m_{\ell\ell}$	$[81, 101]$ GeV	$[76, 106]$ GeV
$m_T(W^{\pm})$	> 30 GeV	-
$p_T(j)$	> 40 GeV	> 50 GeV
$\|\eta(j)\|$	< 4.5	< 4.7
m_{jj}	> 500 GeV	> 500 GeV
JRS	$\eta(j_1) \cdot \eta(j_2) < 0$	$\Delta\eta_{jj} > 2.5$
σ LO	1.28 ± 0.12 fb	1.41 ± 0.21 fb
σ NLO QCD+EW	-	1.24 ± 0.18 fb

variables such as the $W^{\pm}$ rapidity or $m_T(WZ)$ are computed with much looser assumptions than in the $W^{\pm}W^{\pm}jj$ analysis, since just one neutrino is missing in this case and its longitudinal momentum can be inferred by a W-mass constraint on the ℓ-neutrino pair (ℓ being the lepton not associated to the Z decay).

Background contributions from other SM processes or from nonprompt leptons are sub-dominant and are estimated in a similar way as for the $W^{\pm}W^{\pm}jj$ analyses. The ATLAS and CMS data with superimposed signal and background components are shown in Fig. 20.

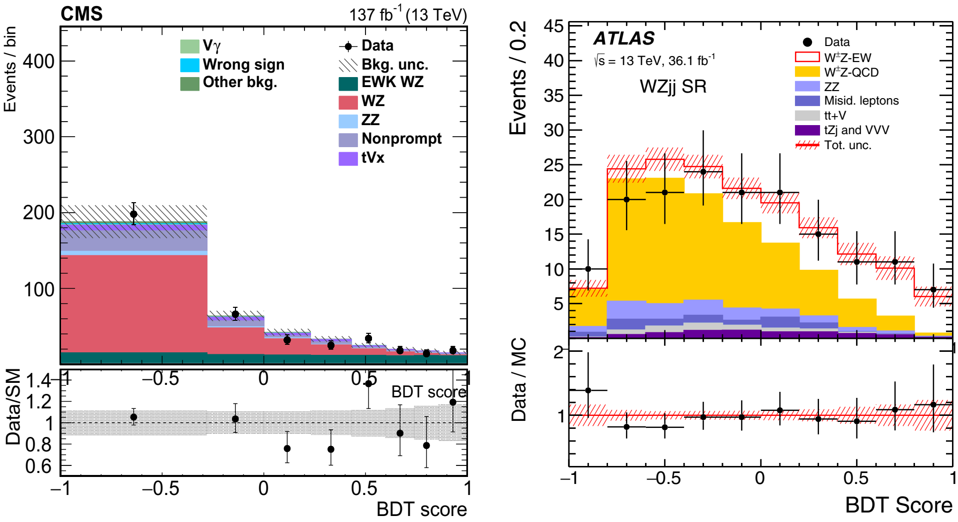

Fig. 20. Post-fit BDT-score distributions in CMS (left) and ATLAS (right) in the $W^{\pm}Zjj$ analysis. Process labeling is consistent, with the exception of events containing top quarks and vector bosons, which are merged in one category in the CMS plot.

Systematic uncertainties. In both ATLAS and CMS, two of the dominant uncertainties are the limited size of simulated samples and the theory errors on the $W^{\pm}Zjj$ production via 2 strong vertices. Among the experimental ones, lepton momentum and efficiency determinations bring the largest uncertainty in CMS, while in ATLAS jet energy scale and resolution uncertainties have a larger impact. No single contribution has an impact larger than 6% in either analysis, the EW search analysis being statistically dominated in both experiments.

Results. ATLAS reports a measured fiducial cross-section of $\sigma_{\mathrm{EW}} = 2.28^{+0.48}_{-0.42}\,\mathrm{fb}$, where the total uncertainty is dominated by the statistical one, finding a fairly large measured-to-SM ratio of 1.77. It corresponds to a background-only hypothesis rejection with a significance of 5.3σ, while only 3.2σ is expected. CMS similarly reports $\sigma_{\mathrm{EW}} = 1.81 \pm 0.41\,\mathrm{fb}$, also larger but more in agreement with the NLO QCD+EW estimations in the respective fiducial region. It corresponds to a background-only hypothesis rejection with a significance of 6.8σ.

The total $W^{\pm}Zjj$ cross-section including EW and strong components is also measured to be $\sigma_{\mathrm{tot}} = 6.7 \pm 1.0$ fb in ATLAS and $\sigma_{\mathrm{tot}} = 4.97 \pm 0.46$ fb in CMS. Differential cross-sections are reported only for the EW+strong case, as a function of m_{jj} in CMS and as a function of many variables in the ATLAS analysis. In CMS, agreement is found with the SM predictions. In ATLAS the same conclusion is reached, but only after scaling up these predictions by the quite large measured-to-SM cross-section ratio.

In the CMS study, limits on aQGC are set by fitting the diboson transverse mass distribution in the signal region and the results are statistically combined to those of the $W^{\pm}W^{\pm}jj$ analysis to obtain more stringent limits.

3.3. *The ZZjj $\to \ell^+\ell^-\ell'^+\ell'^-jj$ and $\to \ell^+\ell^-\nu\bar{\nu}jj$ final states*

The ZZjj VBS process has the smallest cross-section among the final states containing heavy vector bosons, and is one of the rarest SM processes observed to date. Since strong production is also a dominant background over the EW signal, the search for ZZjj is an experimental challenge. However, its experimental signature is very clean and, being the only final state where full reconstruction of the 6 final-state fermions is possible, it could become important for polarization measurements with larger datasets in the future.

3.3.1. *Theoretical calculations*

The theoretical status of the ZZjj channel is rather similar to the $W^{\pm}Zjj$ one. In particular, the QCD corrections to EW contributions are known since some time[64] and have been matched subsequently to PS.[81] NLO QCD corrections have also been computed for the QCD background in Ref. 181 and the matched results to parton-shower can be obtained from modern Monte Carlo generators.

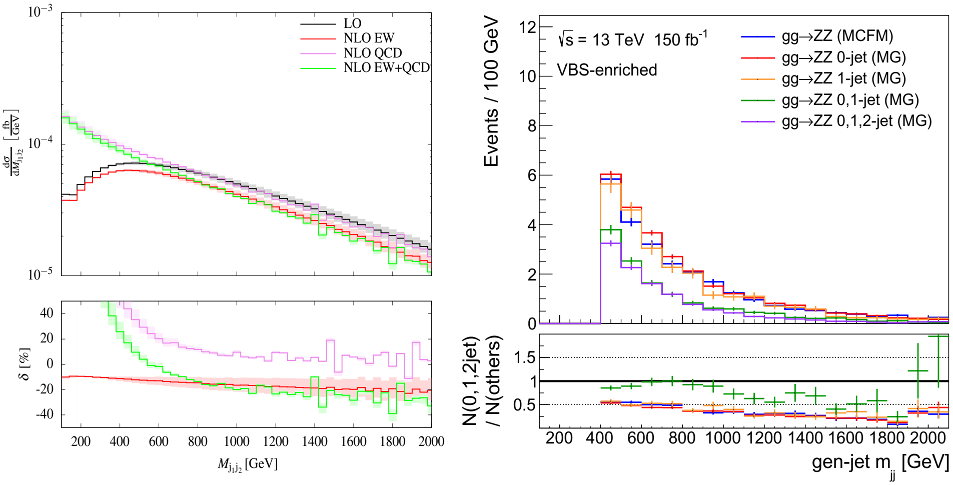

Fig. 21. Various differential distributions for the ZZ channel. Left: invariant mass of the two tagging jets with NLO EW + QCD corrections. Right: invariant mass of the two tagging jets with matching and merging of different jet multiplicities. These figures are taken from Refs. 68 and 182, respectively.

The full NLO contributions of orders $\mathcal{O}(\alpha^7)$ and $\mathcal{O}(\alpha_s\alpha^6)$ and all contributing leading orders along with the loop-induced contribution of order $\mathcal{O}(\alpha_s^4\alpha^4)$ have been computed in Ref. 68. Results show the same hierarchy as for $W^\pm W^\pm jj$ and $W^\pm Zjj$ and, furthermore, that loop-induced channels can contribute significantly in typical fiducial regions. This can be seen for example in Fig. 21 where, beyond a di-jet invariant mass of 500 GeV, QCD corrections are small while the EW ones are substantial. In Ref. 68, the loop-induced contribution simply amounts to include the $gg \to e^+e^-\mu^+\mu^-gg$ channel. Reference 182 went beyond, by studying loop-induced ZZ diboson production with up to 2 jets merged and matched to parton showers.[1] In particular, a proper description of loop-induced contributions can have a significant impact in relevant phase-space regions (see Fig. 21).

A summary of the available predictions is provided in Table 5. Note that the loop-induced contributions are not indicated there as they are only known at LO.

In Ref. 23, it has been pointed out that for ZZjj the VBS approximation is less accurate at LO than at NLO. The main reason is that performing the full computation implies including also tri-boson contributions where one of the gauge boson decays hadronically. This means that, when including real QCD radiation, the two tagging jets could be the gluon radiation and a jet from the aforementioned heavy gauge boson. The gauge boson can be resonant if the two quarks originating from its decay recombine in a single jet. While rather suppressed, such configurations can be significant when low di-jet invariant masses are used. This is particularly

---

[1] Very recently NLO QCD corrections matched to parton shower for the loop-induced process $gg \to e^+e^-\mu^+\mu^-$ were presented in Refs. 183 and 184

Table 5. Summary of higher-order predictions currently available for the ZZ channel: at fixed order and matched to parton shower. The symbols ✓, ✓*, and **X** means that the corresponding predictions are available, in the VBS approximation, or not yet.

Order	$\mathcal{O}(\alpha^7)$	$\mathcal{O}(\alpha_s\alpha^6)$	$\mathcal{O}({\alpha_s}^2\alpha^5)$	$\mathcal{O}({\alpha_s}^3\alpha^4)$
NLO	✓	✓	**X**	✓
NLO+PS	**X**	✓*	**X**	✓

explicit in the left-hand side of Fig. 21 where at low invariants, the QCD corrections are large while they become small for larger invariant masses.

While such corrections are perfectly legitimate as they describe a physical effect due to the interplay between the nature of the process and the event selection, in experimental analysis, the tri-boson contributions are often subtracted using LO Monte-Carlo simulations. First, as argued previously, this makes the measurement more dependent on theoretical input. Second, when using low di-jet invariant masses, the physical effect described above will then never been described by the theoretical predictions not including tri-boson contributions. This example illustrates perfectly the need to perform measurements as theory-independent as possible and have exchange between experiment and theory.

3.3.2. *Experimental approaches*

ATLAS has reported observation of EW ZZjj production using the full Run-2 dataset[185] and combining the two ZZ decay channels. CMS only analyzed events with four charged leptons and, after an earlier publication with limited sensitivity,[186] has recently reported a strong evidence for the EW production with the entire 13 TeV statistics.[26]

Monte Carlo simulation. CMS uses MG5_aMC at LO without additional partons to simulate the EW and interference components. The EW-QCD interference is positive and estimated to be 3%–9% of the EW signal in the various fiducial regions considered in the analysis. An alternative estimation at NLO QCD using POWHEG is also considered.[81] The QCD-induced ZZ+jets process (without loop-induced contributions) is simulated at NLO with up to one extra partons using MG5_aMC, merging the jet multiplicities according to the FxFx scheme,[93] and normalizing the total cross-section to NNLO QCD predictions for diboson production.[187] While the loop-induced contribution only appears at NNLO in QCD, this contribution is significant because of the gg initial state, which is dominant at the LHC. This contribution is included via a dedicated simulation at LO with up to two extra partons, using advanced MG5_aMC settings as described in Ref. 182. Parton Distribution Functions and scale choices follow those made in the $W^\pm W^\pm jj$ analysis.

ATLAS uses the same simulation as CMS for EW and interference, but with LO PDFs, and the full size of the interference component is conservatively used as an uncertainty. SHERPA 2.2.2 is used instead to simulate both the loop-induced and tree-level strong processes, at LO (NLO) and with up to one (three) extra partons, depending on the final state. In the $2\ell 2\nu$jj channel, a dedicated Monte Carlo generator, GG2VV, is used for the inclusive diboson loop-induced component.[188]

Other backgrounds, such as tribosons, $\mathrm{t\bar{t}W^{\pm}}$, and $\mathrm{t\bar{t}Z}$, are generated using different tools, QCD accuracies, and extra-parton multiplicities in the two experiments. These are in general a minor contribution to the selected data samples. The only exception is the most inclusive fiducial region of the CMS analysis, where the triboson contribution is significant at low m_{jj} values and is subtracted using simulation.

Fiducial region definitions and reconstruction-level selections. Fiducial regions considered in the ATLAS and CMS analyses are compared in Table 6. In ATLAS a single value for the combined $4\ell jj$ and $2\ell 2\nu jj$ phase-space is given. In CMS, results are given in three different fiducial region corresponding to increasing degrees of VBS enrichment.

Reconstruction-level selections follow the fiducial regions requirements very closely with minor additions (in CMS electron p_{T} thresholds are raised to 7 GeV, in ATLAS the Z-mass requirement is $[66, 116]$ GeV and the $p_{\mathrm{T,miss}}$ variable is replaced by its significance). Double or single-lepton triggers are used to select data, keeping in general a very high efficiency.

Analysis strategy and background estimation. Both ATLAS and CMS use multivariate analyses to isolate the EW signal over the large QCD background. In the 4ℓjj channel, ATLAS uses a BDT comprised of 12 variables: m_{jj}, Δy_{jj}, jet p_{T} and rapidities, Z candidate p_{T} and rapidities, and combinations of full-event variables.

Table 6. Comparison of ZZjj fiducial region definitions and related EW (VBS) cross-section values in the ATLAS and CMS measurements.[26,185] JRS stands for generic Jet-Rapidity Separation selections.

Variable	ATLAS 4ℓjj	ATLAS $2\ell 2\nu$jj	CMS (inclusive/loose/tight)
$p_{\mathrm{T}}(\ell)$	$> 20/20/10/7$ GeV	$> 30/20$ GeV	$> 20/10/5/5$ GeV
$\|\eta(\ell)\|$	$< 2.7/2.5$	< 2.5	< 2.5
$\Delta R(\ell\ell')$	> 0.2	—	—
$m_{\ell\ell}$	$[60, 120]$ GeV	$[80, 100]$ GeV	$[60, 120]$ GeV
$m_{4\ell}$	—	—	> 180 GeV
$p_{\mathrm{T,miss}}$	—	> 130 GeV	—
$p_{\mathrm{T}}(\mathrm{j})$	$> 40/30$ GeV	$> 60/40$ GeV	> 30 GeV
$\|\eta(\mathrm{j})\|$	< 4.5	< 4.5	< 4.7
m_{jj}	> 300 GeV	> 400 GeV	$> 100/400/1000$ GeV
JRS	$\Delta y_{\mathrm{jj}} > 2$	$\Delta y_{\mathrm{jj}} > 2$	$\Delta\eta_{\mathrm{jj}} > 0/2.4/2.4$
σ LO	0.61 ± 0.03 fb		$0.28 \pm 0.02\,/\,0.19 \pm 0.02\,/\,0.10 \pm 0.01$ fb
σ NLO QCD	-		$0.28 \pm 0.02\,/\,0.20 \pm 0.02\,/\,0.11 \pm 0.01$ fb

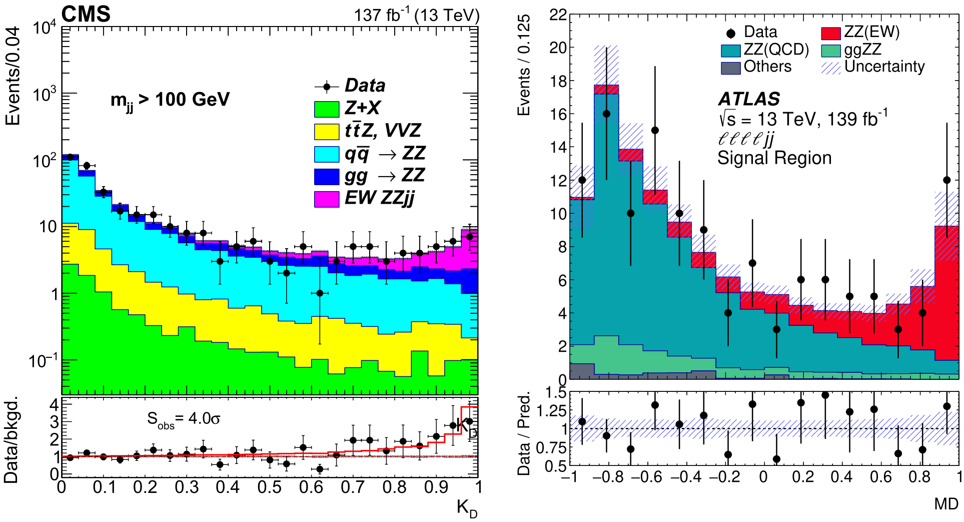

Fig. 22. Post-fit K_D distribution in CMS (left) and BDT score distribution in ATLAS (right) in the ZZjj analysis. The very different signal-to-background ratio is due to the different VBS-enrichment level in the two figures.

A similar choice is done for the $2\ell 2\nu$jj channel, replacing the quantities related to the undetected Z with $p_{\mathrm{T,miss}}$, its significance, and related variables. In CMS, the kinematic EW discriminant K_D is instead built from analytical matrix elements of the EW and strong processes at LO, obtained from the MCFM generator and using the MELA event-probability calculator.[189–191]

Both ATLAS and CMS use QCD-enriched control regions to validate background estimates in the 4ℓ channel, while the background from one Z boson and nonprompt leptons is sub-dominant. In the ATLAS $2\ell 2\nu$jj channel, the evaluation of the QCD contribution is instead simulation-based while control regions are used to estimate other important background processes such as $\mathrm{W}^{\pm}$Zjj, $\mathrm{W}^{+}\mathrm{W}^{-}$jj, and $\mathrm{t\bar{t}}$.

The ATLAS and CMS 4ℓjj data with superimposed signal and background components are shown in Fig. 22.

Systematic uncertainties. In both ATLAS and CMS uncertainties are given as fraction of predicted yields and not as impacts on the cross-section measurements, which makes comparisons more difficult. The ATLAS uncertainties appear to be dominated by a very large (30%) theory uncertainty on the strong ZZjj production simulated with Sherpa. In CMS this uncertainty, EW uncertainties, as well as uncertainties on lepton and jet measurements contribute in similar amounts.

Results. ATLAS reports a measured fiducial cross-section of $\sigma_{\mathrm{EW}} = 0.82 \pm 0.21\,\mathrm{fb}$, where the total uncertainty is dominated by the statistical one. It corresponds to a background-only hypothesis rejection with a significance of 5.5σ, while 4.3σ is expected, with the $4\ell jj$ channel exhibiting a much larger sensitivity. In the three fiducial regions CMS reports $\sigma_{\mathrm{EW,incl}} = 0.33^{+0.12}_{-0.11}\,\mathrm{fb}$, $\sigma_{\mathrm{EW,loose}} = 0.18^{+0.09}_{-0.08}\,\mathrm{fb}$, and $\sigma_{\mathrm{EW,tight}} = 0.09^{+0.05}_{-0.04}$ fb, all in agreement with SM expectations at both LO and NLO in QCD. The background-only hypothesis is rejected with a significance of 4.0σ.

In ATLAS, the total ZZjj cross-section including EW and strong components is also measured to be $\sigma_{\mathrm{tot}} = 1.27 \pm 0.14$ fb in the 4ℓjj channel and $\sigma_{\mathrm{tot}} = 1.2 \pm 0.3$ fb in the $2\ell2\nu$jj channel. In CMS the measured value is $\sigma_{\mathrm{tot}} = 5.3 \pm 0.6$ fb, in the most inclusive fiducial region.

In the CMS analysis, limits on aQGC are set by fitting the ZZ invariant mass distribution in the most inclusive region. These are particularly constraining for the T8 and T9 operators, which only involve neutral fields and to which this channel has therefore the greatest sensitivity.

3.4. *The $W^+W^-jj \to \ell^\pm\nu\ell'^\mp\nu jj$ final state*

3.4.1. *Theoretical calculations*

Finally the $\mathrm{W^+W^-}$jj channel raised a lot of theoretical interest in the past years. The QCD corrections to the EW signal are known in the VBS approximation[63] and have been matched to parton shower.[80] The QCD background is also known at the same accuracy, namely NLO QCD[192, 193] and matched to parton shower.[194] A summary of the available predictions is provided in Table 7. It is reasonable to think that the theoretical accuracy for this final state will be comparable to the one of the other channels in the next few years. In order not to include resonant top quarks contributions, care has to be taken. One should either use the 4-flavor scheme or use the 5-flavor scheme and carefully remove top-quark contributions (see for example Ref. 192).

3.4.2. *Experimental approaches*

There are so far no published results from ATLAS and CMS on the $\mathrm{W^+W^-}$jj channel. With respect to other channels, in this case the top-pair background with dileptonic $\mathrm{W^\pm}$ decays is dominant and requires a very efficient b-quark jet veto, bringing larger experimental uncertainties. The analysis method and preliminary results are available in Ref. 195.

Table 7. Summary of higher-order predictions currently available for the os-WW channel: At fixed order and matched to parton shower. The symbols ✓, ✓*, and ✗ means that the corresponding predictions are available, in the VBS approximation, or not yet.

Order	$\mathcal{O}(\alpha^7)$	$\mathcal{O}(\alpha_s\alpha^6)$	$\mathcal{O}(\alpha_s{}^2\alpha^5)$	$\mathcal{O}(\alpha_s{}^3\alpha^4)$
NLO	✗	✓*	✗	✓
NLO+PS	✗	✓*	✗	✓

3.5. *The semileptonic final states*

3.5.1. *Theoretical calculations*

As seen in the previous sections, theoretical predictions for VBS signatures with fully leptonic final states are numerous and rather complete. Unfortunately, to date, there are no public predictions beyond LO accuracy for any of the semileptonic signatures. Such processes include $\mathrm{pp} \to \ell^+\ell^-\mathrm{jjjj}$ and $\mathrm{pp} \to \ell\nu_\ell\mathrm{jjjj}$, meaning that they involve four jets and two leptons in the final state. This is currently at the edge of the state of the art, as only two such computations have been performed[196,197] and both describe processes with bottom quarks in the final state, meaning that in a VBS analysis they would probably be discarded because of b-jet vetoes.

While the necessary technology is already there, the two aforementioned semileptonic processes require the combination of two ($\mathrm{W}^\pm\mathrm{Zjj}$ and ZZjj) or three ($\mathrm{W}^\pm\mathrm{W}^\pm\mathrm{jj}$, $\mathrm{W}^\pm\mathrm{Zjj}$, and $\mathrm{W}^+\mathrm{W}^-\mathrm{jj}$) VBS processes, respectively, implying a significant computing burden for such signatures. Nonetheless, generating the on-shell gauge bosons at NLO QCD and then decaying them either leptonically or hadronically would be an option. This would lead to neglecting some nonresonant and interference contributions which are expected to be small, or even negligible, but it would considerably reduce the computing time. For example, for the $\ell\nu_\ell\mathrm{jjjj}$ final state, this would imply computation at NLO QCD of the on-shell processes $\mathrm{pp} \to \mathrm{W}^+\mathrm{W}^-\mathrm{jj}$, $\mathrm{pp} \to \mathrm{W}^\pm\mathrm{Zjj}$, and $\mathrm{pp} \to \mathrm{W}^\pm\mathrm{W}^\pm\mathrm{jj}$, before adding the corresponding decays of the heavy gauge bosons. This can be done for both the background and the signal, provided care is taken regarding the VBS approximations.

3.5.2. *Experimental approaches*

Both ATLAS and CMS have reported studies of semileptonic VBS final states in the 2016 subset of the 13 TeV LHC data, including $\mathrm{W}^\pm V$ and $\mathrm{Z}V$. However, the two analyses are rather different in their principles and scopes.

The ATLAS study[198] is targeting a SM VBS measurement, therefore combining a larger set of experimental signatures to cover the largest possible phase-space at the price of very high backgrounds. The study employs a complex multivariate analysis based on BDTs in a total of nine event categories. Events in categories differ in the number of charged leptons used to identify the leptonic vector-boson decay (0 leptons for $\mathrm{Z} \to \nu\bar{\nu}$, 1 lepton for $\mathrm{W}^\pm \to \ell^\pm\nu$, 2 leptons for $\mathrm{Z} \to \ell^+\ell^-$) and in the way the hadronic vector-boson decay (denoted as V) is identified: two categories are used for *merged* single-jet reconstruction, which differ in the purity of the selection working point, and one for the *resolved* two-jet reconstruction. The reconstruction of the merged jet employs the anti-k_T algorithm with a large distance parameter $R = 1.0$ and its identification is based on the *jet trimming* technique,[199] which looks for candidate subjets inside the larger-area jet and discards constituents not associated to those subjets. The invariant mass of the merged jet m_J is computed after trimming and the jet is re-calibrated.

The CMS study[200] is only devoted to BSM searches and therefore it is just a cut-based analysis, optimized for VV high-invariant-mass regions. Only two categories are considered, $\mathrm{W}^{\pm} \to \ell^{\pm}\nu$ and $\mathrm{Z} \to \ell^{+}\ell^{-}$ plus a merged jet. Sensitivity to SM VBS is not evaluated, while the absence of excesses at high mass are interpreted in terms of constraints on aQGC in EFT or on a complete BSM theory, the Georgi–Machacek model.[201] The merged jet reconstruction in CMS uses the anti-k_{T} algorithm with $R = 0.8$: jets are identified by the more recent modified mass-drop algorithm,[202] providing a cleaner estimate of the invariant mass. The "τ_N-subjettiness" variable, related to the compatibility of the large-area with being composed of N subjets, can be used to select jet candidates compatible with hadronic V decays.

Monte Carlo simulation. CMS uses MG5_aMC at LO without additional partons to simulate the EW, strong, and interference components for all the possible final states considered in the analysis, as well as for all BSM samples. An important feature of semileptonic searches is that there are important contributions from the single-W and Drell–Yan processes, where additional jets from QCD are misreconstructed as the hadronic V decay, as well as from processes with top quarks. The processes V+jets with up to four outgoing partons at Born level are simulated at QCD LO accuracy using MG5_aMC and merged using the MLM matching scheme. The $\mathrm{t\bar{t}}$, $\mathrm{t\bar{t}}V$, and single-top processes are generated at NLO accuracy using POWHEG. The simulated samples of background processes are normalized to the best predictions available for the total cross-sections. PDF and scale choices follow those made in other 13 TeV CMS analyses for 2016 simulations.

The ATLAS simulation choices are very similar. The W + jets and Drell–Yan processes are generated using Sherpa 2.2.1, and a NLO alternative description with up to two extra partons is also used. Strong VV production is also simulated with Sherpa and is more advanced than in CMS, up to one additional parton at NLO and up to three additional partons at LO. Matching and merging for Sherpa samples are performed in the MEPS scheme. Interference between EW and strong VV production is neglected and therefore used as a systematic uncertainty in the measurement, variable between 5% and 10% at different values of the BDT score (see below).

Fiducial region definitions and/or reconstruction-level selections. Fiducial regions considered in the ATLAS analysis are shown in Table 8. Since CMS only targets BSM constraints, there is no corresponding fiducial region, so offline event selection requirements are shown instead.

In both ATLAS and CMS the 2ℓ and 1ℓ channel events are selected with single-electron or single-muon triggers while events for the ATLAS 0ℓ channel were recorded with triggers requiring large $p_{\mathrm{T,miss}}$. Both experiment require strictly zero b-tagged jets in channels with reconstructed $\mathrm{W}^{\pm}$, to strongly suppress top-quark background.

Table 8. Fiducial region definitions and related EW (VBS) cross-section values in the ATLAS semileptonic VBS measurement,[198] and the reconstruction-level selections in the analogous CMS analysis.[200] The symbol J (capitalized) stands for a merged jet. The subscripts V and tag stand for jets from V decays or VBS-tagging jets, respectively.

Variable	ATLAS	CMS (reconstruction level)
$p_{\mathrm{T}}(\ell)$	> 27 GeV (1ℓ), $> 28/20$ GeV (2ℓ)	> 50 GeV (1ℓ), $> 50/30$ GeV (2ℓ)
$\|\eta(\ell)\|$	< 2.5	$< 2.4/2.5$
$m_{\ell\ell}$	$[83, 99]$ GeV (2ℓ)	$[76, 106]$ GeV (2ℓ)
$p_{\mathrm{T,miss}}$	> 200 GeV (0ℓ), > 80 GeV (1ℓ)	$> 50/80$ GeV ($1e/1\mu$)
$p_{\mathrm{T}}(\mathrm{J})$	> 200 GeV (merged)	> 200 GeV
$\|\eta(\mathrm{J})\|$	< 2.0 (merged)	< 2.4
$\tau_2/\tau_1(\mathrm{J})$	—	< 0.55
$\|\eta(\mathrm{j})\|$	< 4.5	< 5.0
$p_{\mathrm{T}}(\mathrm{j}_V)$	$> 40/20$ GeV (resolved)	—
$m_{\mathrm{jj},V}$ or m_{J}	$[64, 106]$ GeV	$[65, 105]$ GeV
$p_{\mathrm{T}}(\mathrm{jj}_{\mathrm{tag}})$	> 30 GeV	> 30 GeV
$m_{\mathrm{jj,tag}}$	> 400 GeV	> 800 GeV
JRS	$\eta_{\mathrm{j}_1,\mathrm{tag}} \cdot \eta_{\mathrm{j}_2,\mathrm{tag}} < 0$	$\Delta\eta_{\mathrm{jj,tag}} > 4.0$
σ LO	43.0 ± 2.4 fb	—

In ATLAS, reconstruction-level selections follow the fiducial regions requirements very closely with minor additions (tightened Z-mass requirement, jet–lepton and jet–jet angular separation, multijet suppression in the 0ℓ channel). Enhancement of the BSM EW components in the 1-ℓ channel is performed in CMS using Zeppenfeld variables previously defined and the boson *centrality*, defined as: $\Theta = \min[\min(\eta_{\mathrm{W}}, \eta_V) - \min(\eta_{\mathrm{j}_1,\mathrm{tag}}, \eta_{\mathrm{j}_2,\mathrm{tag}}), \max(\eta_{\mathrm{W}}, \eta_V) - \max(\eta_{\mathrm{j}_1,\mathrm{tag}}, \eta_{\mathrm{j}_2,\mathrm{tag}})]$.

Analysis strategy and background estimation. The ATLAS analyses uses different BDTs for the resolved- and merged-jet categories, comprising many variables (16 and 23, respectively, when considering all lepton channels) to isolate the SM VBS signal over the large backgrounds. Among the list of variables, not just kinematic and jet-identification ones are used, but also variables sensitive to the quark or gluon origin of small-area jets such as the jet width, the number of charged tracks inside the jet, and the number of "track jets" which are built as alternative to calorimeter-based jets with only charged tracks compatible with the hardest event vertex.

CMS uses the transverse mass $m_{\mathrm{T}}(\mathrm{W}V)$ or the invariant mass $m(\mathrm{Z}V)$ for the final fits. The background estimation is obtained by analytical fits with suitable empirical functions. Fit template shapes for the various background components are obtained using the m_{J} sidebands, and correcting with sideband-to-signal transfer factors obtained from simulation. In ATLAS, the estimation of the two main backgrounds W/Z+jets and $\mathrm{t\bar{t}}$ is performed in dedicated control regions, obtained by using the m_{J} sidebands or inverting the b-tag requirement, respectively. From these regions, simulation-to-data correction factors are obtained as a function of $m_{\mathrm{jj,tag}}$ and applied to simulated BDT shapes in the signal regions. The nine BDT

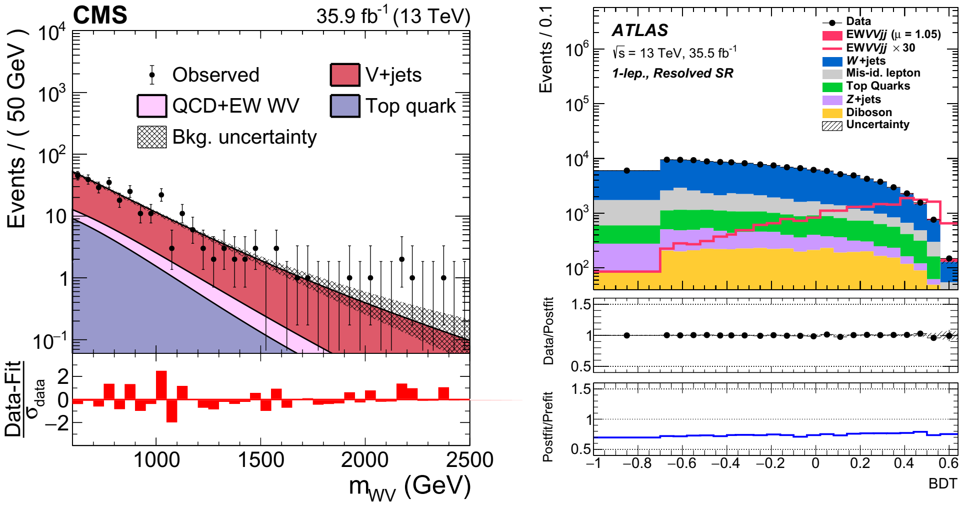

Fig. 23. Distribution of $m_{\mathrm{T}}(\mathrm{WZ})$ in the 1ℓ CMS signal region (left) and of the BDT score in the 1ℓ ATLAS signal region with resolved jets. The dominance of W + jets background is evident in both cases. In the CMS plot, the continuous line indicates the analytical fit.

output distributions, as well as the $m_{\mathrm{jj,tag}}$ shapes in the control regions, are used in the statistical analysis.

The ATLAS and CMS WV data with superimposed signal and background components are shown in Fig. 23.

Systematic uncertainties. In ATLAS, many systematic uncertainties contribute to a total uncertainty which is larger than the statistical one. Among the theoretical and modeling uncertainties, the main contributions are the limited size of the simulated samples and the modeling of the Z + jet component; while among the experimental uncertainties, the largest are the uncertainties on the b-tag veto and the identification and energy calibration of merged jets.

CMS uncertainties are defined by variation of single components and their impact on the results is not provided. In general, larger theory uncertainties than in ATLAS appear to contribute for both the EW, QCD, and BSM components. Other significant contributions come from limited simulated statistics and merged-jet description in agreement with the ATLAS study.

Results. ATLAS reports a measured fiducial cross-section of $\sigma_{\mathrm{EW}} = 45 \pm 18\,\mathrm{fb}$, where the systematic uncertainty is about twice the statistical one. It corresponds to a background-only hypothesis rejection with a significance of 2.7σ, while 2.5σ is expected. The merged analysis has a much better systematic/statistical ratio with respect to the resolved one, and gives the largest contribution to the significance.

In the CMS analysis, limits on aQGC are set by fitting the mass distributions mentioned before. The list of constrained Wilson coefficients is the same as in the combined leptonic $W^{\pm}W^{\pm}$jj and $W^{\pm}$Zjj CMS analysis. While obtained with about one fourth of the data, constraints using the semileptonic analysis are comparable or better. In some case the limits supersede those obtained in the leptonic analysis by a factor of 3–5, in particular for what concerns the $f_{S,1}$ and the mixed operators.

3.6. *The $W^{\pm}\gamma jj$ and $Z\gamma jj$ final states*

While not immediately connected to the EWSB mechanism, VBS production of $W^{\pm}\gamma$jj and $Z\gamma$jj is still interesting for both verifying SM calculations and BSM searches. In particular, it shares many theoretical and experimental features with the scattering of heavy gauge bosons. The direct detection of the high-energy photon without decays to secondary particles makes the fiducial cross-sections particularly large. In both cases, only leptonic W and Z decays are considered. With this choice, $V\gamma$jj production from diagrams involving QCD vertices is the dominant background, even though in the $W^{\pm}\gamma$jj case some contamination from SM processes with top-quarks and photons remains.

3.6.1. *Theoretical calculations*

At the moment, the theory predictions for the production of a heavy gauge boson in association with a photon via VBS are rather limited. For $W^{\pm}\gamma$jj, they consist in the NLO QCD corrections to the EW signal[203] and to the QCD background.[204] The same holds true for $Z\gamma$jj, with NLO QCD corrections available in the VBS approximation[205] and fully for the background.[206]

We note that the $\gamma\gamma$ case, which has two jets and two photons in the final state, has also been studied theoretically at NLO QCD for the signal[207] and the background.[208–210] Unfortunately, as opposed to $W^{\pm}\gamma$jj and $Z\gamma$jj this EW production has not been measured yet at the LHC, due to the overwhelming multijet background.

3.6.2. *Experimental approaches*

ATLAS and CMS have reported evidence of EW $Z\gamma$jj production using a partial Run-2 dataset.[211,212] The CMS result is used in combination with 8 TeV data to obtain the observed evidence. Only CMS performed the search for the $W^{\pm}\gamma$jj final state[213] in the same dataset, leading to the observation of this process.

Photon reconstruction and identification proceed in similar ways in ATLAS and CMS[214,215] and have many points is common with the corresponding procedures for electrons. The electromagnetic shower reconstruction in the calorimeter is analogous and the identification criteria include shower shape (in the ATLAS case information is used in each single LAr layer) and small energy leakage in the hadronic calorimeter. Isolation requirements in trackers and calorimeters are also similar to those used to select electrons, even if in tracker isolation no charged particle is excluded from the cone. In ATLAS, identification is performed separately for photons converted in e^+e^- pairs in the detector material, while in CMS this contribution is not considered. Selection requirements are in general tighter than for electrons and different for the barrel and endcap regions of the detectors, with barrel photons showing higher purity because of smaller jet backgrounds.[m]

Monte Carlo simulation. The $W^\pm\gamma jj$ and $Z\gamma jj$ analyses adopt similar simulation strategies as other VBS analyses for signal and background. VBS signals are simulated at LO with MG5_aMC or Sherpa, with no additional partons besides the two tagging jets. The EW-QCD interferences are estimated to be 1%–3% (3%–8%) of the EW $W^\pm\gamma jj$ ($Z\gamma jj$) signal in the fiducial regions. The corresponding QCD-induced processes are simulated either at LO with a number of extra partons exceeding two or at NLO with a number of extra partons of at least two using the MG5_aMC and Sherpa generators. In general, the Monte Carlo generator results are used to normalize the cross-sections of simulated samples, since higher-order QCD calculations are not matching the analysis phase-spaces.[181,206] A unique background to these searches is the $t\bar{t}\gamma$ SM process, with at least one top quark decaying leptonically, which is simulated using MG5_aMC at LO (NLO) in ATLAS (CMS).

Fiducial region definitions and reconstruction-level selections. Fiducial regions considered in the ATLAS and CMS analyses are compared in Table 9. The same assumptions as in $W^\pm W^\pm jj$ are used for τ decays and lepton "dressing".

Reconstruction-level selections follow the fiducial regions requirements. All analyses use single- or double-lepton triggers to select events online.

Table 9. Comparison of $W^\pm\gamma jj$ and $Z\gamma jj$ fiducial region definitions and related EW (VBS) cross-section values in the ATLAS and CMS measurements.[211–213] JRS stands for generic Jet-Rapidity Separation selections. The large differences in the $Z\gamma jj$ fiducial-region choice for the ATLAS and CMS searches is noticeable.

Variable	ATLAS $Z\gamma jj$	CMS $Z\gamma jj$	CMS $W^\pm\gamma jj$
$p_T(\ell)$	> 20 GeV	$> 25/20$ GeV	> 30 GeV
$\|\eta(\ell)\|$	< 2.5	$< 2.5/2.4$	< 2.4
$\Delta R(\ell\gamma)$	> 0.4	> 0.7	—
$m_{\ell\ell}/m_T(W)$	> 40 GeV	$[70, 110]$ GeV	> 30 GeV
$p_T(\gamma)$	> 15 GeV	> 20 GeV	> 25 GeV
$\|\eta(\gamma)\|$	< 2.37	< 2.5	< 2.5
$m(\ell\ell\gamma) + m(\ell\ell)$	> 182 GeV	—	—
$p_{T,\text{miss}}$	—	—	> 30 GeV
$p_T(j)$	> 50 GeV	> 30 GeV	$> 50/40$ GeV
$\|\eta(j)\|$	< 4.5	< 4.7	< 4.7
m_{jj}	> 150 GeV	> 500 GeV	> 500 GeV
JRS	$\Delta y_{jj} > 1$	$\Delta\eta_{jj} > 2.5$	$\Delta\eta_{jj} > 2.5$
centrality	< 5	—	—
σ LO	7.8 ± 0.5 fb	5.0 ± 0.3 fb	17.03 fb

---

[m] Both ATLAS and CMS exclude from photon acceptance a small $|\eta|$ region corresponding to the transition between barrel and endcap calorimetry.

In the ATLAS Zγjj analysis, where particle-flow categorization is not employed, a complex procedure is used to remove potential overlaps between detector signals identified as lepton QED radiation, photons and jets.

In CMS, a selection on $m(V\gamma) > 100$ GeV reduces the contribution from final-state radiation in Z-boson decays. For the W case, the invariant mass is computed by imposing a W-mass constraint to determine the longitudinal momentum of the missing neutrino. Further VBS enrichment is obtained using the Zeppenfeld variable of the $V\gamma$ system and its azimuthal-angle difference with the dijet system.

Analysis strategy and background estimation. The ATLAS Zγjj analysis uses a BDT algorithm to isolate the EW signal over the backgrounds, where the 13 input variables are related to the kinematic properties of the two tagging jets, the photon, and the reconstructed Z boson.

CMS uses a two-dimensional fits using the most discriminating variables, which are (m_{jj}, $\Delta\eta_{\text{jj}}$) in the Zγjj case and (m_{jj}, $m(\ell\gamma)$) in the W$^{\pm}\gamma$jj case. In both analyses, events are first separated by lepton flavor and central or forward rapidity regions, and control regions with small VBS yields are fit together with the signal regions to constrain background normalizations from data.

In all cases the largest background component is the QCD W$^{\pm}\gamma$jj or Zγjj production and the next-to-largest comes from V+jets events where the photon is misidentified or not coming from the hard-scattering event. The former is estimated from simulation while the second is obtained using control regions in data with relaxed photon selections. The ATLAS and CMS data with superimposed signal and background components are shown in Fig. 24.

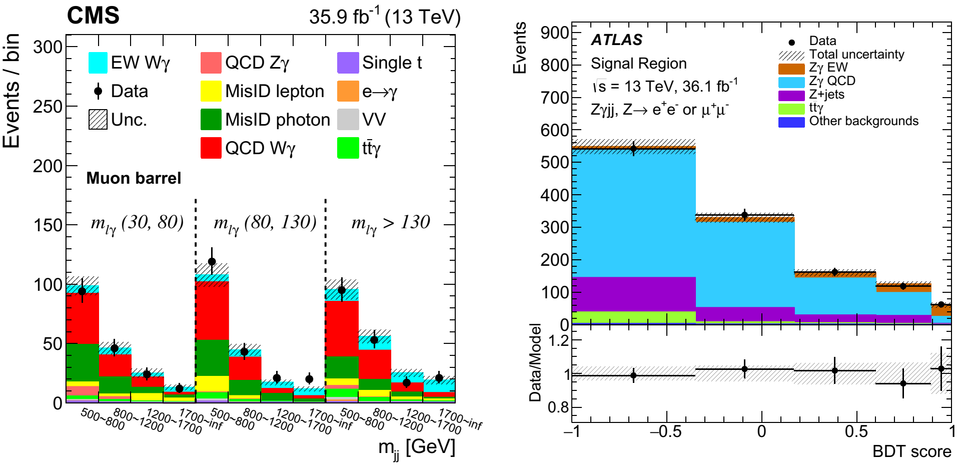

Fig. 24. Post-fit m_{jj} distributions in $m(\ell\gamma)$ intervals in the CMS W$^{\pm}\gamma$jj analysis (central-rapidity $\mu\gamma$ channel, left) and ATLAS output BDT score in the Zγjj analysis (right). The "MisID photon" event category in CMS is dominated by W +jets events.

Systematic uncertainties. In ATLAS the largest systematic impacts are from the limited size of simulated samples, theory errors on the $\mathrm{Z}\gamma\mathrm{jj}$ EW production, and nonprompt-photon background modeling from data. In CMS, the uncertainties are given as variations on a specific process and not as total impacts on the measurements. From their absolute size, it can be inferred that a larger uncertainty than in ATLAS is considered for the theory modeling of the QCD production, at least for $\mathrm{W}^{\pm}\gamma\mathrm{jj}$. Among the experimental uncertainties, jet energy scale and resolution uncertainties have a larger impact with respect to lepton and photon identification, in both experiments.

Results. ATLAS reports a measured fiducial cross-section of $\sigma_{\mathrm{EW}} = 7.8 \pm 2.0\,\mathrm{fb}$, where the total uncertainty is almost equally shared between statistical and systematic + modeling uncertainties. It corresponds to a background-only hypothesis rejection with a significance of 4.1σ, in perfect agreement with expectations according to the MG5_aMC simulation, while Sherpa predicts a somehow larger cross-section.

For $\mathrm{Z}\gamma\mathrm{jj}$ CMS similarly reports $\sigma_{\mathrm{EW}} = 3.2 \pm 1.2\,\mathrm{fb}$, where the ratio to the expectation is 0.65. It corresponds to a background-only hypothesis rejection with a significance of 3.9σ, while 5.2σ was expected, and the compatibility with the SM is approximately at the 1.5σ level. In the CMS case, the fiducial region is more restrictive, hence the statistical uncertainty is dominant. For $\mathrm{W}^{\pm}\gamma\mathrm{jj}$ the corresponding CMS results are $\sigma_{\mathrm{EW}} = 20 \pm 5\,\mathrm{fb}$, where the ratio to the expectation is 1.2 and in agreement with the SM. It corresponds to a background-only hypothesis rejection with a significance of 5.3σ, while 4.8σ was expected.

The total cross-sections including EW and strong components are measured to be $\sigma_{\mathrm{Z}\gamma\mathrm{jj,tot}} = 71^{+23}_{-19}\,\mathrm{fb}$ in ATLAS, $\sigma_{\mathrm{Z}\gamma\mathrm{jj,tot}} = 14 \pm 3\,\mathrm{fb}$ and $\sigma_{\mathrm{W}^{\pm}\gamma\mathrm{jj,tot}} = 108 \pm 16\,\mathrm{fb}$ in CMS, all in good agreement with the SM.

In the CMS analyses, limits on aQGC are set by fitting the diboson-mass distributions in the signal region with additional requirements on the minimum transverse momentum of the photon, and/or m_{jj}. The range of explored aQGC includes both mixed and transverse operators. The $\mathrm{W}^{\pm}\gamma\mathrm{jj}$ analysis is the most sensitive to the operators which do not affect anomalous production of heavy vector bosons (where the semileptonic or exclusive analyses give the most stringent limits), namely $f_{M,2}$, $f_{M,3}$, $f_{M,4}$, $f_{M,5}$, $f_{T,5}$, $f_{T,6}$, and $f_{T,7}$.

3.7. *The exclusive $\gamma\gamma \to W^+W^-$ final state*

Central exclusive production processes in proton–proton collisions are those in which the scattering is mediated through photon–photon fusion. The studies of these processes can be carried out in particularly clean experimental conditions thanks to the absence of proton remnants. However, since the direction of the scattered protons is almost parallel to the beam line, these particles escape detection in ATLAS and CMS. Considering this fact, there are two ways to perform exclusive studies: the first is to just use information from the main apparati, where protons are undetected, and require very low track and neutral activity in the selected events, in addition to the hard-scattering products; the second is to *tag* the protons using dedicated detectors placed along the LHC beams at distance from the main detectors. The Precision Proton Spectrometer (PPS) is a recent example.[216]

The exclusive $\gamma\gamma \to \mathrm{W}^+\mathrm{W}^-$ is a production process of the VBS type and, as such, is sensitive to BSM physics and in particular aQGC. It can be performed in the leptonic final state, using events with only two reconstructed leptons and large missing momentum in the main detectors, or in hadronic final states, where the use of proton tagging constrains the event kinematics and hence is a very powerful background-rejection technique.

3.7.1. *Theoretical calculations*

Compared to standard LHC measurement, the corresponding theoretical predictions are not very much advanced. In particular, for the elastic part i.e. $\gamma\gamma \to \mathrm{W}^+\mathrm{W}^-$, these are usually LO predictions matched to parton shower. They can be obtained from standard Monte Carlo generators and have to be combined with the corresponding photon flux (see for example Ref. 217).

The main background for such a measurement is $q\bar{q} \to \mathrm{W}^+\mathrm{W}^-$ which is very well known from a theoretical point of view with NLO QCD,[218–220] NLO QCD + PS,[90, 221, 222] NNLO QCD,[223, 224] gluon–gluon loop-induced,[225, 226] resummed,[227] and NLO EW[228–233] predictions. Further predictions even feature combinations of the above-mentioned calculations.[234–238]

3.7.2. *Experimental approaches*

ATLAS and CMS studies so far employ the technique which does not require proton tagging. ATLAS recently reported observation of $\gamma\gamma \to \mathrm{W}^+\mathrm{W}^-$ in Run-2 data[239] while CMS has issued only results on less recent datasets at 7 and 8 TeV, finding evidence for this process and stringent aQGC limits on the operators $f_{M,0}$ and $f_{M,1}$.[240]

Since this work deals with LHC Run-2 results, we will just briefly review the ATLAS analysis in the following. The analysis proceeds by requiring an electron and a muon of opposite signs with large dilepton transverse momentum and exactly zero additional charged particles in the event.[n]

Simulation of the signal events and of the $\gamma\gamma \to \ell^+\ell^-$ background without intermediate W bosons proceeds through the HERWIG generator,[86] interfaced to a suitable photon-flux provider and QED-dedicated PDFs. The main background, which is $\mathrm{W}^+\mathrm{W}^-$ production through quark–antiquark annihilation, is simulated using POWHEG.[222]

The fiducial region is defined by event with an electron and a muon with $p_{\mathrm{T},\ell} > 27/20\,\mathrm{GeV}$ (after QED FSR recovery), $|\eta_\ell| < 2.5$, $m_{e\mu} > 20\,\mathrm{GeV}$, $p_{\mathrm{T},e\mu} > 30\,\mathrm{GeV}$

---

[n] The same-flavor case is not considered because of the dominant $\gamma\gamma \to \ell^+\ell^-$ background.

and $n_{trk} = 0$ where trk is any charged particle with $p_{\mathrm{T}} > 0.5\,\mathrm{GeV}$ and $|\eta| < 2.5$. Further offline requirements are applied for the leptons to be compatible with a common vertex.

Background estimation is quite complex because of the multiple sources that can feed additional charged particles in the event and therefore fail the $n_{trk} = 0$ requirement. To improve pile-up descriptions, data-driven methods are used to derive corrections to the simulated events, targeting the density of proton–proton interactions and the number of tracks per interaction separately. Underlying-event modeling of nonexclusive $\mathrm{W}^+\mathrm{W}^-$ production is also corrected from a Drell–Yan control sample in data, while a correction factor for the proton-rescattering effect is derived from a $\gamma\gamma \to \ell^+\ell^-$ control sample.

Signal systematic uncertainties are dominated by the mass-dependent transfer factors between $\gamma\gamma \to \mathrm{W}^+\mathrm{W}^-$ and the $\gamma\gamma \to \ell^+\ell^-$ control sample, while the main systematic background uncertainties arise from variations from different theory predictions of nonexclusive $\mathrm{W}^+\mathrm{W}^-$ production. Overall, the largest impact comes from simulated statistics in background samples.

The fiducial cross-section is determined by fitting the signal region ($p_{\mathrm{T,e}\mu} >$ 30 GeV and $n_{\mathrm{trk}} = 0$) after checking data/prediction agreement in control regions where either $p_{\mathrm{T,e}\mu} <$ 30 GeV or $1 \leq n_{trk} \leq 4$. The significance of the observation is 8.4σ and the corresponding result is $\sigma_{\mathrm{fid}} = 3.1 \pm 0.4\,\mathrm{fb}$, where the statistical and systematic uncertainties are of the same order. Comparing with the corresponding CMS analysis, it can be inferred that constraints on relevant dim-8 operators could be competitive or better than those obtained from deep-inelastic pp collisions.

4. Prospects for High-Luminosity and High-Energy LHC Scenarios

In this section, we discuss prospects for VBS at the upcoming phases of the LHC and at future hadron colliders. At the time when this review is written, not many studies on these topics are available. However, we expect the situation to improve in the next few years when concrete realizations of plans are coming closer. More specifically, we will focus on the High-Luminosity (HL) and High-Energy (HE) phases of the LHC, for which the main physics results are compiled in Ref. 114. The HL run of the LHC is planned to start in 2027 at a center-of-mass energy $\sqrt{s} = 14\,\mathrm{TeV}$, and should provide an integrated luminosity of at least $3000\,\mathrm{fb}^{-1}$ per experiment. On the other hand, a viable option for the HE phase is to occur at $\sqrt{s} = 27\,\mathrm{TeV}$, with expected integrated luminosities of about $15000\,\mathrm{fb}^{-1}$.

From a theoretical point of view, predictions at $\sqrt{s} = 14\,\mathrm{TeV}$ for the HL are very similar to the ones at $\sqrt{s} = 13\,\mathrm{TeV}$ that we have reviewed above. In particular, as for the total cross-sections, the QCD or EW relative corrections only differ by few percent. At $\sqrt{s} = 100\,\mathrm{TeV}$, some results are available in Ref. 241 at LO which are further discussed in Ref. 242. In Table 10, we have compiled LO [$\mathcal{O}(\alpha^6)$] and NLO EW [$\mathcal{O}(\alpha^7)$] predictions for $\mathrm{W}^+\mathrm{W}^+$ at several center-of-mass energies: 14 TeV, 27 TeV and 100 TeV. These results are based on Refs. 100 and 114. It is interesting to

Table 10. Cross-sections at LO and NLO EW for VBS W^+W^+ at a center-of-mass energy of 14 TeV, 27 TeV, and 100 TeV. These numbers are based on Refs. 100 and 114.

$\sqrt{s}$	$\sigma^{\mathrm{LO}}\,[\mathrm{fb}]$	$\sigma^{\mathrm{NLO}}_{\mathrm{EW}}\,[\mathrm{fb}]$	$\delta_{\mathrm{EW}}\,[\%]$
14 TeV	1.4282(2)	1.213(5)	−15.1
27 TeV	4.7848(5)	3.881(7)	−18.9
100 TeV	25.485(9)	19.07(6)	−25.2

see that the cross-sections increase significantly with the center-of-mass energy while the EW corrections become negatively very large. This can simply be understood by the fact that the average typical scale that enters the Sudakov logarithms is increasing. While we focus here on the W^+W^+ channel, these corrections should be rather representative of other channels. Indeed, the Leading-Log approximation obtained following Ref. 102 is identical for all scattering processes of EW bosons as they result from the same $SU(2)_w$ coupling.[67, 68, 100] At 100 TeV, the corrections reach −25% making the use of resummation techniques as well as the inclusion of heavy gauge-bosons radiations necessary.

Experimental perspectives for VBS at the HL-LHC are reviewed in Ref. 114 using simulations of upgraded ATLAS and CMS detectors, a $\sqrt{s} = 14\,\mathrm{TeV}$ hypothesis and a range of integrated luminosities from $300\,\mathrm{fb}^{-1}$ through $8000\,\mathrm{fb}^{-1}$, where the first value corresponds to one year of data taking, and the latter to 10 years of combined datasets collected by the ATLAS and CMS experiments in the most optimistic scenario. All perspective analysis mimic or simplify event selections described in the previous chapters.

For the $W^\pm W^\pm jj$ final state CMS expects an overall uncertainty on the total fiducial VBS cross-section of 4.5% with a luminosity of $3000\,\mathrm{fb}^{-1}$, while for ATLAS this estimation is about $5\% - 6\%$. Concerning the purely longitudinal component of VBS, $W^\pm_L W^\pm_L$, a combination of ATLAS and CMS results, using fully simulated ATLAS events and improved electron efficiency, is expected to reach an expected significance of 3σ with $4000\,\mathrm{fb}^{-1}$ of total integrated luminosity.

For the $W^\pm Zjj$ final state, the predicted uncertainty at $3000\,\mathrm{fb}^{-1}$ in CMS is about 5.5%. In ATLAS, this estimation is provided as a function of the predicted background uncertainty, reflecting the difficulty to anticipate progress in theory calculations, and approaches 5% with the current knowledge. For the polarized components, ATLAS estimate considers inclusive estimations for each boson separately, i.e. sensitivities for $W^+_L Z_X$, $W^-_L Z_X$, and $W^\pm_X Z_L$. The significance is estimated to be between 1.5 and 2.5σ for Z_L and W^+_L and between 0.7 and 1.5σ for W^-_L depending on the final selection and systematic assumptions on the total background normalization. In CMS the doubly longitudinally polarized component is considered and the expected significance is about 1.3-1.4σ at $3000\,\mathrm{fb}^{-1}$.

For the ZZjj final state, estimates in ATLAS and CMS strongly depend on the assumption on the evolution of the theory uncertainty of the QCD component, especially the loop-induced, gluon-initiated one, which is the most challenging from the computational point of view. Estimates on the achievement of the evidence/observation of the process are already superseded by recent Run-2 results. ATLAS also shows perspectives of differential cross-section measurements, that however have uncertainties of 60% or larger after $3000\,\mathrm{fb}^{-1}$. CMS estimates to have a significance for the detection of the purely longitudinal component, $\mathrm{Z_L Z_L}$, varying between 1.2 and 1.4σ, depending on the detector extended muon coverage.

5. Conclusion

In the present work, we have reviewed the state-of-the-art of VBS at the LHC. In particular, for the theoretical part, we have almost exclusively focused our discussion on results in the SM of particle physics. This study therefore summarizes our present understanding of the SM and in particular the EW theory, through the magnifying glass of VBS.

The first part is a general introduction to the most important concepts in the study of VBS at the LHC. First, we have provided a precise definition of VBS at the LHC which should hopefully help for a better use of theoretical progress in experimental analysis. Then, the formalism of polarized VBS is discussed in detail. After this, general theoretical aspects are examined, where emphasis is put on higher-order corrections of QCD and EW origins. A presentation of the most relevant experimental aspects of VBS measurements follows. These include a brief description of the ATLAS and CMS detectors, the details of VBS tagging-jet and vector-boson reconstruction and the simulations used in data analysis. Finally, a short review of constraints on new-physics theories obtained from VBS measurements is provided, with special emphasis on Effective Field Theory interpretations.

In the second part of this report, all possible signatures of VBS at the LHC are examined. For each of the signatures, both the theoretical and experimental aspects are discussed and specificities of each channels are highlighted and explained. Great attention is also given to aspects related to the interface between experiment and theory and, in that respect, some directions are also given in order to improve current methodologies.

The last section is devoted to prospects for the measurements of VBS at future collider experiments. It is rather short, but should be interesting for future VBS studies.

With this work, we have gathered in one unique place, all relevant references for in-depth analysis of VBS at the LHC, which should show useful for both the experimental and theoretical communities. In particular, during the whole review we have tried to keep the discussion at a level which should be understandable by LHC physicists irrespectively of their background. The reason for this is that we are convinced that advance in fundamental physics can only proceed through a deep understanding of both experimental and theoretical aspects, which are two sides of the same coin and can therefore not be isolated. In particular, we believe that this is the way to get the most accurate physics results out of VBS, at present and future high-energy experiments.

Finally, it should be clear from the reading that a lot has already been achieved in the past few years, and that the detailed study of VBS at collider experiments possesses a huge potential for new innovative investigations. In this context, we hope that the present work will contribute to the great progresses that will be achieved in the next years regarding our understand of the EW theory of the SM.

Acknowledgments

We are grateful to the "VBSCan" COST action network CA16108 for offering a stimulating and dynamic atmosphere over the past few years. Without this action, this review would probably not have seen birth. Also, we are deeply indebted to our colleagues and collaborators for the numerous discussions on the topic of VBS. In particular, we would like to thank Pietro Govoni for his commitment in the VBSCan action as well as for feedback on the present manuscript. RC acknowledges support from the Italian and Serbian Ministries for Foreign Affairs through the Researcher Mobility Program RS19MO06. MP acknowledges support from the German Research Foundation (DFG) through the Research Training Group RTG2044. MZ is supported by the "Programma per Giovani Ricercatori Rita Levi Montalcini" granted by the Italian Ministero dell'Università e della Ricerca (MUR).

References

1. S. L. Glashow, *Nucl. Phys.* **22**, 579 (1961), doi:10.1016/0029-5582(61)90469-2.
2. S. Weinberg, *Phys. Rev. Lett.* **19**, 1264 (1967), doi:10.1103/PhysRevLett.19.1264.
3. A. Salam, *Conf. Proc. C* **680519**, 367 (1968), doi:10.1142/9789812795915_0034.
4. P. W. Higgs, *Phys. Lett.* **12**, 132 (1964), doi:10.1016/0031-9163(64)91136-9.
5. P. W. Higgs, *Phys. Rev. Lett.* **13**, 508 (1964), doi:10.1103/PhysRevLett.13.508.
6. F. Englert and R. Brout, *Phys. Rev. Lett.* **13**, 321 (1964), doi:10.1103/PhysRevLett.13.321.
7. G. S. Guralnik, C. R. Hagen and T. W. B. Kibble, *Phys. Rev. Lett.* **13**, 585 (1964), doi:10.1103/PhysRevLett.13.585.
8. P. W. Higgs, *Phys. Rev.* **145**, 1156 (1966), doi:10.1103/PhysRev.145.1156.
9. T. W. B. Kibble, *Phys. Rev.* **155**, 1554 (1967), doi:10.1103/PhysRev.155.1554.
10. ATLAS Collab. (G. Aad *et al.*), *Phys. Lett. B* **716**, 1 (2012), doi:10.1016/j.physletb.2012.08.020, arXiv:1207.7214 [hep-ex].
11. CMS Collab. (S. Chatrchyan *et al.*), *Phys. Lett. B* **716**, 30 (2012), arXiv:1207.7235 [hep-ex], doi:10.1016/j.physletb.2012.08.021.
12. M. Gallinaro *et al.*, Beyond the standard model in vector boson scattering signatures, arXiv:2005.09889 [hep-ph].
13. M. Szleper, arXiv:1412.8367 [hep-ph].
14. D. R. Green, P. Meade and M.-A. Pleier, *Rev. Mod. Phys.* **89**, 035008 (2017), arXiv:1610.07572 [hep-ex], doi:10.1103/RevModPhys.89.035008.
15. M. Rauch, arXiv:1610.08420 [hep-ph].
16. A. Tricoli, M. Schönherr and P. Azzurri, arXiv:2012.13967 [hep-ex].
17. S. Dawson, *Nucl. Phys. B* **249**, 42 (1985), doi:10.1016/0550-3213(85)90038-0.

18. M. J. Duncan, G. L. Kane and W. Repko, *Nucl. Phys. B* **272**, 517 (1986), doi:10.1016/0550-3213(86)90234-8.
19. R. Cahn and S. Dawson, *Phys. Lett. B* **136**, 196 (1984), doi:10.1016/0370-2693(84)91180-8, [Erratum **138**, 464 (1984)].
20. I. Kuss and H. Spiesberger, *Phys. Rev. D* **53**, 6078 (1996), arXiv:hep-ph/9507204, doi:10.1103/PhysRevD.53.6078.
21. E. Accomando, A. Denner and S. Pozzorini, *J. High Energy Phys.* **03**, 078 (2007), arXiv:hep-ph/0611289, doi:10.1088/1126-6708/2007/03/078.
22. T. Figy, C. Oleari and D. Zeppenfeld, *Phys. Rev. D* **68**, 073005 (2003), arXiv:hep-ph/0306109, doi:10.1103/PhysRevD.68.073005.
23. A. Ballestrero *et al.*, *Eur. Phys. J. C* **78**, 671 (2018), arXiv:1803.07943 [hep-ph], doi:10.1140/epjc/s10052-018-6136-y.
24. B. Biedermann, A. Denner and M. Pellen, *J. High Energy Phys.* **10**, 124 (2017), arXiv:1708.00268 [hep-ph], doi:10.1007/JHEP10(2017)124.
25. CMS Collab. (A. M. Sirunyan *et al.*), *Phys. Lett. B* **809**, 135710 (2020), arXiv:2005.01173 [hep-ex], doi:10.1016/j.physletb.2020.135710.
26. CMS Collab. (A. M. Sirunyan *et al.*), *Phys. Lett. B* **812**, 135992 (2021), arXiv:2008.07013 [hep-ex], doi:10.1016/j.physletb.2020.135992.
27. B. W. Lee, C. Quigg and H. Thacker, *Phys. Rev. Lett.* **38**, 883 (1977), doi:10.1103/PhysRevLett.38.883.
28. B. W. Lee, C. Quigg and H. Thacker, *Phys. Rev. D* **16**, 1519 (1977), doi:10.1103/PhysRevD.16.1519.
29. M. S. Chanowitz and M. K. Gaillard, *Phys. Lett. B* **142**, 85 (1984), doi:10.1016/0370-2693(84)91141-9.
30. M. S. Chanowitz and M. K. Gaillard, *Nucl. Phys. B* **261**, 379 (1985), doi:10.1016/0550-3213(85)90580-2.
31. W. Stirling and E. Vryonidou, *J. High Energy Phys.* **07**, 124 (2012), arXiv:1204.6427 [hep-ph], doi:10.1007/JHEP07(2012)124.
32. Z. Bern *et al.*, *Phys. Rev. D* **84**, 034008 (2011), arXiv:1103.5445 [hep-ph], doi:10.1103/PhysRevD.84.034008.
33. J. Aguilar-Saavedra, J. Carvalho, N. F. Castro, F. Veloso and A. Onofre, *Eur. Phys. J. C* **50**, 519 (2007), arXiv:hep-ph/0605190, doi:10.1140/epjc/s10052-007-0289-4.
34. A. Ballestrero, E. Maina and G. Pelliccioli, *J. High Energy Phys.* **03**, 170 (2018), arXiv:1710.09339 [hep-ph], doi:10.1007/JHEP03(2018)170.
35. A. Ballestrero, A. Belhouari, G. Bevilacqua, V. Kashkan and E. Maina, *Comput. Phys. Commun.* **180**, 401 (2009), arXiv:0801.3359 [hep-ph], doi:10.1016/j.cpc.2008.10.005.
36. A. Ballestrero, E. Maina and G. Pelliccioli, *J. High Energy Phys.* **09**, 087 (2019), arXiv:1907.04722 [hep-ph], doi:10.1007/JHEP09(2019)087.
37. A. Aeppli, F. Cuypers and G. J. van Oldenborgh, *Phys. Lett. B* **314**, 413 (1993), arXiv:hep-ph/9303236, doi:10.1016/0370-2693(93)91259-P.
38. A. Aeppli, G. J. van Oldenborgh and D. Wyler, *Nucl. Phys. B* **428**, 126 (1994), arXiv:hep-ph/9312212, doi:10.1016/0550-3213(94)90195-3.
39. W. Beenakker, F. A. Berends and A. Chapovsky, *Nucl. Phys. B* **548**, 3 (1999), arXiv:hep-ph/9811481, doi:10.1016/S0550-3213(99)00110-8.
40. M. Billoni, S. Dittmaier, B. Jäger and C. Speckner, *J. High Energy Phys.* **12**, 043 (2013), arXiv:1310.1564 [hep-ph], doi:10.1007/JHEP12(2013)043.
41. A. Denner, S. Dittmaier, M. Roth and D. Wackeroth, *Nucl. Phys. B* **587**, 67 (2000), arXiv:hep-ph/0006307 [hep-ph], doi:10.1016/S0550-3213(00)00511-3.

42. A. Denner and M. Pellen, *J. High Energy Phys.* **08**, 155 (2016), arXiv:1607.05571 [hep-ph], doi:10.1007/JHEP08(2016)155.
43. A. Denner and G. Pelliccioli, *J. High Energy Phys.* **09**, 164 (2020), arXiv:2006.14867 [hep-ph], doi:10.1007/JHEP09(2020)164.
44. ATLAS Collab. (M. Aaboud *et al.*), *Eur. Phys. J. C* **79**, 535 (2019), arXiv:1902.05759 [hep-ex], doi:10.1140/epjc/s10052-019-7027-6.
45. A. Ballestrero, E. Maina and G. Pelliccioli, *Phys. Lett.* **B811**, 135856 (2020), arXiv:2007.07133 [hep-ph], doi:10.1016/j.physletb.2020.135856.
46. J. Baglio and L. D. Ninh, *Commun. Phys.* **30**, 35 (2020), arXiv:1910.13746 [hep-ph], doi:10.15625/0868-3166/30/1/14461.
47. A. Denner and G. Pelliccioli, arXiv:2010.07149 [hep-ph].
48. D. Buarque Franzosi, O. Mattelaer, R. Ruiz and S. Shil, *J. High Energy Phys.* **04**, 082 (2020), arXiv:1912.01725 [hep-ph], doi:10.1007/JHEP04(2020)082.
49. J. Alwall, R. Frederix, S. Frixione, V. Hirschi, F. Maltoni, O. Mattelaer, H. S. Shao, T. Stelzer, P. Torrielli and M. Zaro, *J. High Energy Phys.* **07**, 079 (2014), arXiv:1405.0301 [hep-ph], doi:10.1007/JHEP07(2014)079.
50. P. Artoisenet, R. Frederix, O. Mattelaer and R. Rietkerk, *J. High Energy Phys.* **03**, 015 (2013), arXiv:1212.3460 [hep-ph], doi:10.1007/JHEP03(2013)015.
51. M. Grossi, J. Novak, B. Kersevan and D. Rebuzzi, *Eur. Phys. J. C* **80**(12), 1144 (2020).
52. D. B. Kaplan and H. Georgi, *Phys. Lett. B* **136**, 183 (1984), doi:10.1016/0370-2693(84)91177-8.
53. D. B. Kaplan, H. Georgi and S. Dimopoulos, *Phys. Lett. B* **136**, 187 (1984), doi:10.1016/0370-2693(84)91178-X.
54. H. Georgi and D. B. Kaplan, *Phys. Lett. B* **145**, 216 (1984), doi:10.1016/0370-2693(84)90341-1.
55. M. J. Dugan, H. Georgi and D. B. Kaplan, *Nucl. Phys. B* **254**, 299 (1985), doi:10.1016/0550-3213(85)90221-4.
56. R. Contino, Y. Nomura and A. Pomarol, *Nucl. Phys. B* **671**, 148 (2003), arXiv:hep-ph/0306259, doi:10.1016/j.nuclphysb.2003.08.027.
57. K. Agashe, R. Contino and A. Pomarol, *Nucl. Phys. B* **719**, 165 (2005), arXiv:hep-ph/0412089, doi:10.1016/j.nuclphysb.2005.04.035.
58. R. Contino, L. Da Rold and A. Pomarol, *Phys. Rev. D* **75**, 055014 (2007), arXiv:hep-ph/0612048, doi:10.1103/PhysRevD.75.055014.
59. K. Agashe, R. Contino, L. Da Rold and A. Pomarol, *Phys. Lett. B* **641**, 62 (2006), arXiv:hep-ph/0605341, doi:10.1016/j.physletb.2006.08.005.
60. B. Bellazzini, C. Csáki and J. Serra, *Eur. Phys. J. C* **74**, 2766 (2014), arXiv:1401.2457 [hep-ph], doi:10.1140/epjc/s10052-014-2766-x.
61. G. Panico and A. Wulzer, *The Composite Nambu-Goldstone Higgs* (Springer, 2016).
62. T. Han, G. Valencia and S. Willenbrock, *Phys. Rev. Lett.* **69**, 3274 (1992), arXiv:hep-ph/9206246, doi:10.1103/PhysRevLett.69.3274.
63. B. Jäger, C. Oleari and D. Zeppenfeld, *J. High Energy Phys.* **07**, 015 (2006), arXiv:hep-ph/0603177, doi:10.1088/1126-6708/2006/07/015.
64. B. Jäger, C. Oleari and D. Zeppenfeld, *Phys. Rev. D* **73**, 113006 (2006), arXiv:hep-ph/0604200, doi:10.1103/PhysRevD.73.113006.
65. G. Bozzi, B. Jäger, C. Oleari and D. Zeppenfeld, *Phys. Rev. D* **75**, 073004 (2007), arXiv:hep-ph/0701105, doi:10.1103/PhysRevD.75.073004.
66. B. Jäger, C. Oleari and D. Zeppenfeld, *Phys. Rev. D* **80**, 034022 (2009), arXiv:0907.0580 [hep-ph], doi:10.1103/PhysRevD.80.034022.

67. A. Denner, S. Dittmaier, P. Maierhöfer, M. Pellen and C. Schwan, *J. High Energy Phys.* **06**, 067 (2019), arXiv:1904.00882 [hep-ph], doi:10.1007/JHEP06(2019)067.
68. A. Denner, R. Franken, M. Pellen and T. Schmidt, *J. High Energy Phys.* **11**, 110 (2020), arXiv:2009.00411 [hep-ph], doi:10.1007/JHEP11(2020)110.
69. P. Bolzoni, F. Maltoni, S.-O. Moch and M. Zaro, *Phys. Rev. Lett.* **105**, 011801 (2010), arXiv:1003.4451 [hep-ph], doi:10.1103/PhysRevLett.105.011801.
70. P. Bolzoni, F. Maltoni, S.-O. Moch and M. Zaro, *Phys. Rev. D* **85**, 035002 (2012), arXiv:1109.3717 [hep-ph], doi:10.1103/PhysRevD.85.035002.
71. M. Cacciari, F. A. Dreyer, A. Karlberg, G. P. Salam and G. Zanderighi, *Phys. Rev. Lett.* **115**, 082002 (2015), arXiv:1506.02660 [hep-ph], doi:10.1103/PhysRevLett.115.082002, [Erratum **120**, 139901 (2018)].
72. F. A. Dreyer and A. Karlberg, *Phys. Rev. Lett.* **117**, 072001 (2016), arXiv:1606.00840 [hep-ph], doi:10.1103/PhysRevLett.117.072001.
73. F. A. Dreyer and A. Karlberg, *Phys. Rev. D* **98**, 114016 (2018), arXiv:1811.07906 [hep-ph], doi:10.1103/PhysRevD.98.114016.
74. F. A. Dreyer and A. Karlberg, *Phys. Rev. D* **99**, 074028 (2019), arXiv:1811.07918 [hep-ph], doi:10.1103/PhysRevD.99.074028.
75. F. A. Dreyer, A. Karlberg, J.-N. Lang and M. Pellen, arXiv:2005.13341 [hep-ph].
76. T. Liu, K. Melnikov and A. A. Penin, *Phys. Rev. Lett.* **123**, 122002 (2019), arXiv:1906.10899 [hep-ph], doi:10.1103/PhysRevLett.123.122002.
77. F. A. Dreyer, A. Karlberg and L. Tancredi, arXiv:2005.11334 [hep-ph].
78. B. Jäger, A. Karlberg, S. Plätzer, J. Scheller and M. Zaro, *Eur. Phys. J. C* **80**, 756 (2020), arXiv:2003.12435 [hep-ph], doi:10.1140/epjc/s10052-020-8326-7.
79. B. Jäger and G. Zanderighi, *J. High Energy Phys.* **11**, 055 (2011), arXiv:1108.0864 [hep-ph], doi:10.1007/JHEP11(2011)055.
80. B. Jäger and G. Zanderighi, *J. High Energy Phys.* **04**, 024 (2013), arXiv:1301.1695 [hep-ph], doi:10.1007/JHEP04(2013)024.
81. B. Jäger, A. Karlberg and G. Zanderighi, *J. High Energy Phys.* **03**, 141 (2014), arXiv:1312.3252 [hep-ph], doi:10.1007/JHEP03(2014)141.
82. B. Jäger, A. Karlberg and J. Scheller, *Eur. Phys. J. C* **79**, 226 (2019), arXiv:1812.05118 [hep-ph], doi:10.1140/epjc/s10052-019-6736-1.
83. T. Sjöstrand, S. Mrenna and P. Z. Skands, *Comput. Phys. Commun.* **178**, 852 (2008), arXiv:0710.3820 [hep-ph], doi:10.1016/j.cpc.2008.01.036.
84. T. Sjöstrand, S. Ask, J. R. Christiansen, R. Corke, N. Desai, P. Ilten, S. Mrenna, S. Prestel, C. O. Rasmussen and P. Z. Skands, *Comput. Phys. Commun.* **191**, 159 (2015), arXiv:1410.3012 [hep-ph], doi:10.1016/j.cpc.2015.01.024.
85. M. Bahr *et al.*, *Eur. Phys. J. C* **58**, 639 (2008), arXiv:0803.0883 [hep-ph], doi:10.1140/epjc/s10052-008-0798-9.
86. J. Bellm *et al.*, *Eur. Phys. J. C* **76**, 196 (2016), arXiv:1512.01178 [hep-ph], doi:10.1140/epjc/s10052-016-4018-8.
87. J. Bellm *et al.*, *Eur. Phys. J. C* **80**, 452 (2020), arXiv:1912.06509 [hep-ph], doi:10.1140/epjc/s10052-020-8011-x.
88. P. Nason, *J. High Energy Phys.* **11**, 040 (2004), arXiv:hep-ph/0409146, doi:10.1088/1126-6708/2004/11/040.
89. S. Frixione, P. Nason and C. Oleari, *J. High Energy Phys.* **11**, 070 (2007), arXiv:0709.2092 [hep-ph], doi:10.1088/1126-6708/2007/11/070.
90. S. Frixione and B. R. Webber, *J. High Energy Phys.* **06**, 029 (2002), arXiv:hep-ph/0204244, doi:10.1088/1126-6708/2002/06/029.
91. CMS Collab. (A. M. Sirunyan *et al.*), *Eur. Phys. J. C* **78**, 589 (2018), arXiv:1712.09814 [hep-ex], doi:10.1140/epjc/s10052-018-6049-9.

92. B. Cabouat and T. Sjöstrand, *Eur. Phys. J. C* **78**, 226 (2018), arXiv:1710.00391 [hep-ph], doi:10.1140/epjc/s10052-018-5645-z.
93. R. Frederix, S. Frixione, S. Prestel and P. Torrielli, *J. High Energy Phys.* **07**, 238 (2020), arXiv:2002.12716 [hep-ph], doi:10.1007/JHEP07(2020)238.
94. J. Butterworth *et al.*, *J. Phys. G* **43**, 023001 (2016), arXiv:1510.03865 [hep-ph], doi:10.1088/0954-3899/43/2/023001.
95. R. Bellan *et al.*, VBSCan Thessaloniki 2018 Workshop Summary, in *2nd Vector Boson Scattering Coordination and Action Network Annual Meeting*, (2019), arXiv:1906.11332 [hep-ph].
96. M. Zaro, P. Bolzoni, F. Maltoni and S.-O. Moch, *PoS* **CHARGED2010**, 028 (2010), arXiv:1012.1806 [hep-ph], doi:10.22323/1.114.0028.
97. M. Zaro and H. Logan, Recommendations for the interpretation of LHC searches for H_5^0, $H_5^{\pm}$, and $H_5^{\pm\pm}$ in vector boson fusion with decays to vector boson pairs, LHCHXSWG-2015-001, technical report (2015).
98. LHC Higgs Cross Section Working Group Collab. (D. de Florian *et al.*), **2/2017** (10 2016), arXiv:1610.07922 [hep-ph], doi:10.23731/CYRM-2017-002.
99. A. Denner and S. Dittmaier, *Phys. Rept.* **864**, 1 (2020), arXiv:1912.06823 [hep-ph], doi:10.1016/j.physrep.2020.04.001.
100. B. Biedermann, A. Denner and M. Pellen, *Phys. Rev. Lett.* **118**, 261801 (2017), arXiv:1611.02951 [hep-ph], doi:10.1103/PhysRevLett.118.261801.
101. A. Denner and T. Hahn, *Nucl. Phys. B* **525**, 27 (1998), arXiv:hep-ph/9711302, doi:10.1016/S0550-3213(98)00287-9.
102. A. Denner and S. Pozzorini, *Eur. Phys. J. C* **18**, 461 (2001), arXiv:hep-ph/0010201, doi:10.1007/s100520100551.
103. M. Chiesa, A. Denner, J.-N. Lang and M. Pellen, *Eur. Phys. J. C* **79**, 788 (2019), arXiv:1906.01863 [hep-ph], doi:10.1140/epjc/s10052-019-7290-6.
104. A. Manohar, P. Nason, G. P. Salam and G. Zanderighi, *Phys. Rev. Lett.* **117**, 242002 (2016), arXiv:1607.04266 [hep-ph], doi:10.1103/PhysRevLett.117.242002.
105. A. V. Manohar, P. Nason, G. P. Salam and G. Zanderighi, *J. High Energy Phys.* **12**, 046 (2017), arXiv:1708.01256 [hep-ph], doi:10.1007/JHEP12(2017)046.
106. A. Martin, R. Roberts, W. Stirling and R. Thorne, *Eur. Phys. J. C* **39**, 155 (2005), arXiv:hep-ph/0411040, doi:10.1140/epjc/s2004-02088-7.
107. C. Schmidt, J. Pumplin, D. Stump and C. Yuan, *Phys. Rev. D* **93**, 114015 (2016), arXiv:1509.02905 [hep-ph], doi:10.1103/PhysRevD.93.114015.
108. NNPDF Collab. (R. D. Ball, V. Bertone, S. Carrazza, L. Del Debbio, S. Forte, A. Guffanti, N. P. Hartland and J. Rojo), *Nucl. Phys. B* **877**, 290 (2013), arXiv:1308.0598 [hep-ph], doi:10.1016/j.nuclphysb.2013.10.010.
109. NNPDF Collab. (V. Bertone, S. Carrazza, N. P. Hartland and J. Rojo), *SciPost Phys.* **5**, 008 (2018), arXiv:1712.07053 [hep-ph], doi:10.21468/SciPostPhys.5.1.008.
110. L. Harland-Lang, A. Martin, R. Nathvani and R. Thorne, *Eur. Phys. J. C* **79**, 811 (2019), arXiv:1907.02750 [hep-ph], doi:10.1140/epjc/s10052-019-7296-0.
111. S. Frixione, V. Hirschi, D. Pagani, H. Shao and M. Zaro, *J. High Energy Phys.* **09**, 065 (2014), arXiv:1407.0823 [hep-ph], doi:10.1007/JHEP09(2014)065.
112. S. Frixione, V. Hirschi, D. Pagani, H. S. Shao and M. Zaro, *J. High Energy Phys.* **06**, 184 (2015), arXiv:1504.03446 [hep-ph], doi:10.1007/JHEP06(2015)184.
113. M. Czakon, D. Heymes, A. Mitov, D. Pagani, I. Tsinikos and M. Zaro, *J. High Energy Phys.* **10**, 186 (2017), arXiv:1705.04105 [hep-ph], doi:10.1007/JHEP10(2017)186.
114. P. Azzi *et al.*, *CERN Yellow Rep. Monogr.* **7**, 1 (2019), arXiv:1902.04070 [hep-ph], doi:10.23731/CYRM-2019-007.1.

115. A. Denner, S. Dittmaier, M. Pellen and C. Schwan, *Phys. Lett. B* **798**, 134951 (2019), arXiv:1907.02366 [hep-ph], doi:10.1016/j.physletb.2019.134951.
116. ATLAS Collab. (G. Aad *et al.*), *JINST* **3**, S08003 (2008), doi:10.1088/1748-0221/3/08/S08003.
117. CMS Collab. (S. Chatrchyan *et al.*), *JINST* **3**, S08004 (2008), doi:10.1088/1748-0221/3/08/S08004.
118. M. Pellen, *Phys. Rev. D* **101**, 013002 (2020), arXiv:1908.06805 [hep-ph], doi:10.1103/PhysRevD.101.013002.
119. ATLAS Collab. (G. Aad *et al.*), *JINST* **15**, P10004 (2020), arXiv:2007.12539 [physics.ins-det], doi:10.1088/1748-0221/15/10/P10004.
120. CMS Collab. (V. Khachatryan *et al.*), *JINST* **12**, P01020 (2017), arXiv:1609.02366 [physics.ins-det], doi:10.1088/1748-0221/12/01/P01020.
121. ATLAS Collab. (G. Aad *et al.*), *Eur. Phys. J. C* **77**, 490 (2017), arXiv:1603.02934 [hep-ex], doi:10.1140/epjc/s10052-017-5004-5.
122. CMS Collab. (A. Sirunyan *et al.*), *JINST* **12**, P10003 (2017), arXiv:1706.04965 [physics.ins-det], doi:10.1088/1748-0221/12/10/P10003.
123. M. Cacciari, G. P. Salam and G. Soyez, *J. High Energy Phys.* **04**, 063 (2008), arXiv:0802.1189 [hep-ex], doi:10.1088/1126-6708/2008/04/063.
124. M. Cacciari, G. P. Salam and G. Soyez, *Eur. Phys. J. C* **72**, 1896 (2012), arXiv:1111.6097 [hep-ph], doi:10.1140/epjc/s10052-012-1896-2.
125. ATLAS Collab. (M. Aaboud *et al.*), *Phys. Rev. D* **96**, 072002 (2017), arXiv:1703.09665 [hep-ex], doi:10.1103/PhysRevD.96.072002.
126. CMS Collab. (V. Khachatryan *et al.*), *JINST* **12**, P02014 (2017), arXiv:1607.03663 [hep-ex], doi:10.1088/1748-0221/12/02/P02014.
127. M. Cacciari and G. P. Salam, *Phys. Lett. B* **659**, 119 (2008), arXiv:0707.1378 [hep-ph], doi:10.1016/j.physletb.2007.09.077.
128. ATLAS Collab. (G. Aad *et al.*), *Eur. Phys. J. C* **76**, 581 (2016), arXiv:1510.03823 [hep-ex], doi:10.1140/epjc/s10052-016-4395-z.
129. ATLAS Collab. (M. Aaboud *et al.*), *Eur. Phys. J. C* **77**, 580 (2017), arXiv:1705.02211 [hep-ex], doi:10.1140/epjc/s10052-017-5081-5, [Erratum **77**, 712 (2017)].
130. CMS Collab. (A. M. Sirunyan *et al.*), *JINST* **15**, P09018 (2020), arXiv:2003.00503 [hep-ex], doi:10.1088/1748-0221/15/09/P09018.
131. ATLAS Collab., Discrimination of Light Quark and Gluon Jets in pp collisions at $\sqrt{s} = 8$ TeV with the ATLAS Detector, ATLAS-CONF-2016-034, technical report (2016).
132. CMS Collab., Performance of quark/gluon discrimination in 8 TeV pp data, CMS-PAS-JME-13-002, technical report (2013).
133. R. Kogler *et al.*, *Rev. Mod. Phys.* **91**, 045003 (2019), arXiv:1803.06991 [hep-ex], doi:10.1103/RevModPhys.91.045003.
134. ATLAS Collab. (G. Aad *et al.*), *Eur. Phys. J. C* **76**, 292 (2016), arXiv:1603.05598 [hep-ex], doi:10.1140/epjc/s10052-016-4120-y.
135. CMS Collab. (A. Sirunyan *et al.*), *JINST* **13**, P06015 (2018), arXiv:1804.04528 [physics.ins-det], doi:10.1088/1748-0221/13/06/P06015.
136. ATLAS Collab. (M. Aaboud *et al.*), *Eur. Phys. J. C* **79**, 639 (2019), arXiv:1902.04655 [physics.ins-det], doi:10.1140/epjc/s10052-019-7140-6.
137. ATLAS Collab. (G. Aad *et al.*), *JINST* **14**, P12006 (2019), arXiv:1908.00005 [hep-ex], doi:10.1088/1748-0221/14/12/P12006.
138. CMS Collab. (V. Khachatryan *et al.*), *JINST* **10**, P06005 (2015), arXiv:1502.02701 [physics.ins-det], doi:10.1088/1748-0221/10/06/P06005.

139. P. Speckmayer, A. Höcker, J. Stelzer and H. Voss, *J. Phys. Conf. Ser.* **219**, 032057 (2010), doi:10.1088/1742-6596/219/3/032057.
140. ATLAS Collab. (M. Aaboud *et al.*), *Eur. Phys. J. C* **78**, 903 (2018), arXiv:1802.08168 [hep-ex], doi:10.1140/epjc/s10052-018-6288-9.
141. CMS Collab. (A. M. Sirunyan *et al.*), *JINST* **14**, P07004 (2019), arXiv:1903.06078 [hep-ex], doi:10.1088/1748-0221/14/07/P07004.
142. S. Alioli, P. Nason, C. Oleari and E. Re, *J. High Energy Phys.* **06**, 043 (2010), arXiv:1002.2581 [hep-ph], doi:10.1007/JHEP06(2010)043.
143. Sherpa Collab. (E. Bothmann *et al.*), *SciPost Phys.* **7**, 034 (2019), arXiv:1905.09127 [hep-ph], doi:10.21468/SciPostPhys.7.3.034.
144. NNPDF Collab. (R. D. Ball *et al.*), *J. High Energy Phys.* **04**, 040 (2015), arXiv:1410.8849 [hep-ph], doi:10.1007/JHEP04(2015)040.
145. CMS Collab. (V. Khachatryan *et al.*), *Eur. Phys. J. C* **76**, 155 (2016), arXiv:1512.00815 [hep-ex], doi:10.1140/epjc/s10052-016-3988-x.
146. CMS Collab. (A. M. Sirunyan *et al.*), *Eur. Phys. J. C* **80**, 4 (2020), arXiv:1903.12179 [hep-ex], doi:10.1140/epjc/s10052-019-7499-4.
147. GEANT4 Collab. (S. Agostinelli *et al.*), *Nucl. Instrum. Methods A* **506**, 250 (2003), doi:10.1016/S0168-9002(03)01368-8.
148. J. Allison *et al.*, *IEEE Trans. Nucl. Sci.* **53**, 270 (2006), doi:10.1109/TNS.2006.869826.
149. C. Degrande, N. Greiner, W. Kilian, O. Mattelaer, H. Mebane, T. Stelzer, S. Willenbrock and C. Zhang, *Ann. Phys.* **335**, 21 (2013), arXiv:1205.4231 [hep-ph], doi:10.1016/j.aop.2013.04.016.
150. O. J. P. Éboli, M. Gonzalez–Garcia and J. Mizukoshi, *Phys. Rev. D* **74**, 073005 (2006), arXiv:hep-ph/0606118, doi:10.1103/PhysRevD.74.073005.
151. E. d. S. Almeida, O. J. P. Éboli and M. Gonzalez–Garcia, *Phys. Rev. D* **101**, 113003 (2020), arXiv:2004.05174 [hep-ph], doi:10.1103/PhysRevD.101.113003.
152. K. Arnold *et al.*, *Comput. Phys. Commun.* **180**, 1661 (2009), arXiv:0811.4559 [hep-ph], doi:10.1016/j.cpc.2009.03.006.
153. CMS Collab., Limits on anomalous triple and quartic gauge couplings, https://twiki.cern.ch/twiki/bin/view/CMSPublic/PhysicsResultsSMPaTGC, (2020), [Online].
154. G. Perez, M. Sekulla and D. Zeppenfeld, *Eur. Phys. J. C* **78**, 759 (2018), arXiv:1807.02707 [hep-ph], doi:10.1140/epjc/s10052-018-6230-1.
155. R. Gomez-Ambrosio, *Eur. Phys. J. C* **79**, 389 (2019), arXiv:1809.04189 [hep-ph], doi:10.1140/epjc/s10052-019-6893-2.
156. A. Dedes, P. Kozów and M. Szleper, arXiv:2011.07367 [hep-ph].
157. J. J. Ethier, R. Gomez-Ambrosio, G. Magni and J. Rojo, arXiv:2101.03180 [hep-ph].
158. A. Denner, L. Hošeková and S. Kallweit, *Phys. Rev. D* **86**, 114014 (2012), arXiv:1209.2389 [hep-ph], doi:10.1103/PhysRevD.86.114014.
159. J. Baglio *et al.*, arXiv:1107.4038 [hep-ph].
160. J. Baglio *et al.*, arXiv:1404.3940 [hep-ph].
161. T. Melia, K. Melnikov, R. Röntsch and G. Zanderighi, *J. High Energy Phys.* **12**, 053 (2010), arXiv:1007.5313 [hep-ph], doi:10.1007/JHEP12(2010)053.
162. F. Campanario, M. Kerner, L. D. Ninh and D. Zeppenfeld, *Phys. Rev. D* **89**, 054009 (2014), arXiv:1311.6738 [hep-ph], doi:10.1103/PhysRevD.89.054009.
163. T. Melia, P. Nason, R. Röntsch and G. Zanderighi, *Eur. Phys. J. C* **71**, 1670 (2011), arXiv:1102.4846 [hep-ph], doi:10.1140/epjc/s10052-011-1670-x.
164. W. Kilian, T. Ohl and J. Reuter, *Eur. Phys. J. C* **71**, 1742 (2011), arXiv:0708.4233 [hep-ph], doi:10.1140/epjc/s10052-011-1742-y.
165. M. Moretti, T. Ohl and J. Reuter, arXiv:hep-ph/0102195.

166. C. Schwan, *PoS* **RADCOR2017**, 081 (2018), doi:10.22323/1.290.0081.
167. ATLAS Collab., Modelling of the vector boson scattering process $pp \to W^{\pm}W^{\pm}jj$ in Monte Carlo generators in ATLAS, ATL-PHYS-PUB-2019-004, technical report (2019).
168. ATLAS, CMS, LHC EWWG MB Working Group Collab., Comparison of ATLAS and CMS VBS Monte Carlo simulation, ATL-PHYS-PUB-2020-026, technical report (2020).
169. ATLAS Collab. (M. Aaboud *et al.*), *Phys. Rev. Lett.* **123**, 161801 (2019), arXiv:1906.03203 [hep-ex], doi:10.1103/PhysRevLett.123.161801.
170. CMS Collab. (A. M. Sirunyan *et al.*), *Phys. Rev. Lett.* **120**, 081801 (2018), arXiv:1709.05822 [hep-ex], doi:10.1103/PhysRevLett.120.081801.
171. S. Höche, Status of Sherpa event generator, in *Proc. Multi-Boson Interactions Workshop (MBI), University of Michigan* (2018).
172. D. L. Rainwater, R. Szalapski and D. Zeppenfeld, *Phys. Rev. D* **54**, 6680 (1996), arXiv:hep-ph/9605444, doi:10.1103/PhysRevD.54.6680.
173. CMS Collab. (A. M. Sirunyan *et al.*), *Phys. Lett. B* **812**, 136018 (2021), arXiv:2009.09429 [hep-ex], doi:10.1016/j.physletb.2020.136018.
174. F. Campanario, M. Kerner, L. D. Ninh and D. Zeppenfeld, *Phys. Rev. Lett.* **111**, 052003 (2013), arXiv:1305.1623 [hep-ph], doi:10.1103/PhysRevLett.111.052003.
175. Les Houches 2017: Physics at TeV Colliders Standard Model Working Group Report (2018).
176. ATLAS Collab., Modelling of the vector boson scattering process $pp \to W^{\pm}W^{\pm}jj$ in Monte Carlo generators in ATLAS, technical report (2019).
177. ATLAS Collab. (M. Aaboud *et al.*), *Phys. Lett. B* **793**, 469 (2019), arXiv:1812.09740 [hep-ex], doi:10.1016/j.physletb.2019.05.012.
178. J. Alwall *et al.*, *Eur. Phys. J. C* **53**, 473 (2008), arXiv:0706.2569 [hep-ph], doi:10.1140/epjc/s10052-007-0490-5.
179. M. Grazzini, S. Kallweit, D. Rathlev and M. Wiesemann, *J. High Energy Phys.* **05**, 139 (2017), arXiv:1703.09065 [hep-ph], doi:10.1007/JHEP05(2017)139.
180. T. Melia, P. Nason, R. Röntsch and G. Zanderighi, *J. High Energy Phys.* **11**, 078 (2011), arXiv:1107.5051 [hep-ph], doi:10.1007/JHEP11(2011)078.
181. F. Campanario, M. Kerner, L. D. Ninh and D. Zeppenfeld, *J. High Energy Phys.* **07**, 148 (2014), arXiv:1405.3972 [hep-ph], doi:10.1007/JHEP07(2014)148.
182. C. Li, Y. An, C. Charlot, R. Covarelli, Z. Guan and Q. Li, *Phys. Rev. D* **102**, 116003 (2020), arXiv:2006.12860 [hep-ph], doi:10.1103/PhysRevD.102.116003.
183. S. Alioli, S. Ferrario Ravasio, J. M. Lindert and R. Röntsch, arXiv:2102.07783 [hep-ph].
184. M. Grazzini, S. Kallweit, M. Wiesemann and J. Y. Yook, arXiv:2102.08344 [hep-ph].
185. ATLAS Collab. (G. Aad *et al.*), arXiv:2004.10612 [hep-ex], submitted to *Nature Phys.*
186. CMS Collab. (A. M. Sirunyan *et al.*), *Phys. Lett. B* **774**, 682 (2017), arXiv:1708.02812 [hep-ex], doi:10.1016/j.physletb.2017.10.020.
187. M. Grazzini, S. Kallweit, M. Wiesemann and J. Y. Yook, *J. High Energy Phys.* **03**, 070 (2019), arXiv:1811.09593 [hep-ph], doi:10.1007/JHEP03(2019)070.
188. N. Kauer, *J. High Energy Phys.* **12**, 082 (2013), arXiv:1310.7011 [hep-ph], doi:10.1007/JHEP12(2013)082.
189. Y. Gao, A. V. Gritsan, Z. Guo, K. Melnikov, M. Schulze and N. V. Tran, *Phys. Rev. D* **81**, 075022 (2010), arXiv:1001.3396 [hep-ph], doi:10.1103/PhysRevD.81.075022, [Erratum: 10.1103/PhysRevD.81.079905].

190. S. Bolognesi, Y. Gao, A. V. Gritsan, K. Melnikov, M. Schulze, N. V. Tran and A. Whitbeck, *Phys. Rev. D* **86**, 095031 (2012), arXiv:1208.4018 [hep-ph], doi:10.1103/PhysRevD.86.095031.
191. A. V. Gritsan, J. Roskes, U. Sarica, M. Schulze, M. Xiao and Y. Zhou, *Phys. Rev. D* **102**, 056022 (2020), arXiv:2002.09888 [hep-ph], doi:10.1103/PhysRevD.102.056022.
192. T. Melia, K. Melnikov, R. Röntsch and G. Zanderighi, *Phys. Rev. D* **83**, 114043 (2011), arXiv:1104.2327 [hep-ph], doi:10.1103/PhysRevD.83.114043.
193. N. Greiner, G. Heinrich, P. Mastrolia, G. Ossola, T. Reiter and F. Tramontano, *Phys. Lett. B* **713**, 277 (2012), arXiv:1202.6004 [hep-ph], doi:10.1016/j.physletb.2012.06.027.
194. M. Rauch and S. Plätzer, *Eur. Phys. J. C* **77**, 293 (2017), arXiv:1605.07851 [hep-ph], doi:10.1140/epjc/s10052-017-4860-3.
195. A. Cardini, Study of W^+W^- pair production via vector boson scattering in proton-proton collisions at 13 TeV with the CMS experiment, Master thesis, University of Florence (2017).
196. A. Denner and M. Pellen, *J. High Energy Phys.* **02**, 013 (2018), arXiv:1711.10359 [hep-ph], doi:10.1007/JHEP02(2018)013.
197. F. Anger, F. Febres Cordero, H. Ita and V. Sotnikov, *Phys. Rev. D* **97**, 036018 (2018), arXiv:1712.05721 [hep-ph], doi:10.1103/PhysRevD.97.036018.
198. ATLAS Collab. (G. Aad *et al.*), *Phys. Rev. D* **100**, 032007 (2019), arXiv:1905.07714 [hep-ex], doi:10.1103/PhysRevD.100.032007.
199. D. Krohn, J. Thaler and L.-T. Wang, *J. High Energy Phys.* **02**, 084 (2010), arXiv:0912.1342 [hep-ph], doi:10.1007/JHEP02(2010)084.
200. CMS Collab. (A. M. Sirunyan *et al.*), *Phys. Lett. B* **798**, 134985 (2019), arXiv:1905.07445 [hep-ex], doi:10.1016/j.physletb.2019.134985.
201. H. Georgi and M. Machacek, *Nucl. Phys. B* **262**, 463 (1985), doi:10.1016/0550-3213(85)90325-6.
202. A. J. Larkoski, S. Marzani, G. Soyez and J. Thaler, *J. High Energy Phys.* **05**, 146 (2014), arXiv:1402.2657 [hep-ph], doi:10.1007/JHEP05(2014)146.
203. F. Campanario, N. Kaiser and D. Zeppenfeld, *Phys. Rev. D* **89**, 014009 (2014), arXiv:1309.7259 [hep-ph], doi:10.1103/PhysRevD.89.014009.
204. F. Campanario, M. Kerner, L. D. Ninh and D. Zeppenfeld, *Eur. Phys. J. C* **74**, 2882 (2014), arXiv:1402.0505 [hep-ph], doi:10.1140/epjc/s10052-014-2882-7.
205. F. Campanario, M. Kerner and D. Zeppenfeld, *J. High Energy Phys.* **01**, 160 (2018), arXiv:1704.01921 [hep-ph], doi:10.1007/JHEP01(2018)160.
206. F. Campanario, M. Kerner, L. D. Ninh and D. Zeppenfeld, *Eur. Phys. J. C* **74**, 3085 (2014), arXiv:1407.7857 [hep-ph], doi:10.1140/epjc/s10052-014-3085-y.
207. F. Campanario, M. Kerner, D. Ninh and I. Rosario, *J. High Energy Phys.* **06**, 072 (2020), arXiv:2002.12109 [hep-ph], doi:10.1007/JHEP06(2020)072.
208. T. Gehrmann, N. Greiner and G. Heinrich, *Phys. Rev. Lett.* **111**, 222002 (2013), arXiv:1308.3660 [hep-ph], doi:10.1103/PhysRevLett.111.222002.
209. S. Badger, A. Guffanti and V. Yundin, *J. High Energy Phys.* **03**, 122 (2014), arXiv:1312.5927 [hep-ph], doi:10.1007/JHEP03(2014)122.
210. Z. Bern, L. Dixon, F. Febres Cordero, S. Höche, H. Ita, D. Kosower, N. A. Lo Presti and D. Maitre, *Phys. Rev. D* **90**, 054004 (2014), arXiv:1402.4127 [hep-ph], doi:10.1103/PhysRevD.90.054004.
211. ATLAS Collab. (G. Aad *et al.*), *Phys. Lett. B* **803**, 135341 (2020), arXiv:1910.09503 [hep-ex], doi:10.1016/j.physletb.2020.135341.
212. CMS Collab. (A. M. Sirunyan *et al.*), *J. High Energy Phys.* **06**, 076 (2020), arXiv:2002.09902 [hep-ex], doi:10.1007/JHEP06(2020)076.

213. CMS Collab. (A. M. Sirunyan *et al.*), *Phys. Lett. B* **811**, 135988 (2020), arXiv:2008.10521 [hep-ex], doi:10.1016/j.physletb.2020.135988.
214. CMS Collab. (V. Khachatryan *et al.*), *JINST* **10**, P08010 (2015), arXiv:1502.02702 [physics.ins-det], doi:10.1088/1748-0221/10/08/P08010.
215. ATLAS Collab. (M. Aaboud *et al.*), *Eur. Phys. J. C* **79**, 205 (2019), arXiv:1810.05087 [hep-ex], doi:10.1140/epjc/s10052-019-6650-6.
216. CMS, TOTEM Collab., CMS-TOTEM Precision Proton Spectrometer, CERN-LHCC-2014-021, technical report (2014).
217. V. Budnev, I. Ginzburg, G. Meledin and V. Serbo, *Phys. Rept.* **15**, 181 (1975), doi:10.1016/0370-1573(75)90009-5.
218. J. Ohnemus, *Phys. Rev. D* **44**, 1403 (1991), doi:10.1103/PhysRevD.44.1403.
219. U. Baur, T. Han and J. Ohnemus, *Phys. Rev. D* **53**, 1098 (1996), arXiv:hep-ph/9507336, doi:10.1103/PhysRevD.53.1098.
220. J. M. Campbell and R. Ellis, *Phys. Rev. D* **60**, 113006 (1999), arXiv:hep-ph/9905386, doi:10.1103/PhysRevD.60.113006.
221. K. Hamilton, *J. High Energy Phys.* **01**, 009 (2011), arXiv:1009.5391 [hep-ph], doi:10.1007/JHEP01(2011)009.
222. P. Nason and G. Zanderighi, *Eur. Phys. J. C* **74**, 2702 (2014), arXiv:1311.1365 [hep-ph], doi:10.1140/epjc/s10052-013-2702-5.
223. T. Gehrmann, M. Grazzini, S. Kallweit, P. Maierhöfer, A. von Manteuffel, S. Pozzorini, D. Rathlev and L. Tancredi, *Phys. Rev. Lett.* **113**, 212001 (2014), arXiv:1408.5243 [hep-ph], doi:10.1103/PhysRevLett.113.212001.
224. M. Grazzini, S. Kallweit, S. Pozzorini, D. Rathlev and M. Wiesemann, *J. High Energy Phys.* **08**, 140 (2016), arXiv:1605.02716 [hep-ph], doi:10.1007/JHEP08(2016)140.
225. F. Caola, K. Melnikov, R. Röntsch and L. Tancredi, *Phys. Lett. B* **754**, 275 (2016), arXiv:1511.08617 [hep-ph], doi:10.1016/j.physletb.2016.01.046.
226. M. Grazzini, S. Kallweit, M. Wiesemann and J. Y. Yook, *Phys. Lett. B* **804**, 135399 (2020), arXiv:2002.01877 [hep-ph], doi:10.1016/j.physletb.2020.135399.
227. M. Grazzini, S. Kallweit, D. Rathlev and M. Wiesemann, *J. High Energy Phys.* **08**, 154 (2015), arXiv:1507.02565 [hep-ph], doi:10.1007/JHEP08(2015)154.
228. J. Kühn, F. Metzler, A. Penin and S. Uccirati, *J. High Energy Phys.* **06**, 143 (2011), arXiv:1101.2563 [hep-ph], doi:10.1007/JHEP06(2011)143.
229. A. Bierweiler, T. Kasprzik, J. H. Kühn and S. Uccirati, *J. High Energy Phys.* **11**, 093 (2012), arXiv:1208.3147 [hep-ph], doi:10.1007/JHEP11(2012)093.
230. J. Baglio, L. D. Ninh and M. M. Weber, *Phys. Rev. D* **88**, 113005 (2013), arXiv:1307.4331 [hep-ph], doi:10.1103/PhysRevD.94.099902, [Erratum **94**, 099902 (2016)].
231. S. Gieseke, T. Kasprzik and J. H. Kühn, *Eur. Phys. J. C* **74**, 2988 (2014), arXiv:1401.3964 [hep-ph], doi:10.1140/epjc/s10052-014-2988-y.
232. B. Biedermann, M. Billoni, A. Denner, S. Dittmaier, L. Hofer, B. Jäger and L. Salfelder, *J. High Energy Phys.* **06**, 065 (2016), arXiv:1605.03419 [hep-ph], doi:10.1007/JHEP06(2016)065.
233. S. Kallweit, J. Lindert, S. Pozzorini and M. Schönherr, *J. High Energy Phys.* **11**, 120 (2017), arXiv:1705.00598 [hep-ph], doi:10.1007/JHEP11(2017)120.
234. E. Re, M. Wiesemann and G. Zanderighi, *J. High Energy Phys.* **12**, 121 (2018), arXiv:1805.09857 [hep-ph], doi:10.1007/JHEP12(2018)121.

235. M. Grazzini, S. Kallweit, J. M. Lindert, S. Pozzorini and M. Wiesemann, *J. High Energy Phys.* **02**, 087 (2020), arXiv:1912.00068 [hep-ph], doi:10.1007/JHEP02(2020)087.
236. S. Kallweit, E. Re, L. Rottoli and M. Wiesemann, *J. High Energy Phys.* **12**, 147 (2020), arXiv:2004.07720 [hep-ph], doi:10.1007/JHEP12(2020)147.
237. S. Bräuer, A. Denner, M. Pellen, M. Schönherr and S. Schumann, *J. High Energy Phys.* **10**, 159 (2020), arXiv:2005.12128 [hep-ph], doi:10.1007/JHEP10(2020)159.
238. M. Chiesa, C. Oleari and E. Re, *Eur. Phys. J. C* **80**, 849 (2020), arXiv:2005.12146 [hep-ph], doi:10.1140/epjc/s10052-020-8419-3.
239. ATLAS Collab. (G. Aad *et al.*) (2020), arXiv:2010.04019 [hep-ex].
240. CMS Collab. (V. Khachatryan *et al.*), *J. High Energy Phys.* **08**, 119 (2016), arXiv:1604.04464 [hep-ex], doi:10.1007/JHEP08(2016)119.
241. M. L. Mangano *et al.*, *CERN Yellow Rep.*, 1 (2017), arXiv:1607.01831 [hep-ph], doi:10.23731/CYRM-2017-003.1.
242. B. Jäger, L. Salfelder, M. Worek and D. Zeppenfeld, *Phys. Rev. D* **96**, 073008 (2017), arXiv:1704.04911 [hep-ph], doi:10.1103/PhysRevD.96.073008.